Assen Zlatarov University
Burgas, Bulgaria

ANNUAL

1

VOLUME XLVI, BOOK 1, 2017

TECHNICAL AND NATURAL SCIENCES

ASSEN ZLATAROV UNIVERSITY
BURGAS, BULGARIA

ANNUAL

Vol. XLVI, BOOK 1, 2017

TECHNICAL AND NATURAL SCIENCES

Assen Zlatarov University

Assen Zlatarov University
Annual, Vol. XLVI, Book 1, 2017
Burgas 8010, Bulgaria
ISSN 1312-1359

ASSEN ZLATAROV UNIVERSITY
BURGAS, BULGARIA

ANNUAL

Vol. XLVI, BOOK 1, 2017

TECHNICAL AND NATURAL SCIENCES

BURGAS ● 2017

VOLUME XLVI (1). CONTENTS

ANNUAL OF ASSEN ZLATAROV UNIVERSITY, BURGAS
BULGARIA, 2017, v. XLVI (1)

SIMULTANEOUS DETERMINATION OF COPPER AND LEAD IN DRINKING AND LAKE WATERS BY ANODIC STRIPPING VOLTAMMETRY

Nikolay Zaitsev, Dencho Stanev, Krasimira Stancheva, Viktoria Trifonova, Veska Shivacheva, Hristivelina Jecheva
E-mail: krasimiraangelova@abv.bg

ABSTRACT

Anodic stripping voltammetry has been developed for the simultaneous determination of copper (II) and lead (II) in drinking and lake waters. The stripping peaks were obtained at -50 to -200 mV for copper and at -400 to -500 mV for lead ions, supporting electrolyte 0.01 M HNO_3. The concentrate was stripped by changing the potential from -1300 to +400 mV, at a potential sweep rate 25 mV/s. The content of analytes determined by the standard addition method were: 66.0 ± 5.6 μg/l Cu^{2+} in drinking water; 105.4 ± 6.4 μg/l Cu^{2+} in lake water and 5.7 ± 0.4 μg/l Pb^{2+} in drinking water; 9.5 ± 0.7 μg/l Pb^{2+} in lake water, respectively. The concentrations of metals determined are below the international permissible limits and do not pose a health concern for the consumption of water in Burgas Region.

Key words: *voltammetry, copper and lead determination, drinking and lake waters*

INTRODUCTION

Toxic and heavy metals are everywhere in the environment and they are a major cause of disease, aging, and even genetic defects. They are the most toxic inorganic pollutants and can be of both natural and anthropogenic origin associated with various sources of harmful emissions. The effects of toxic and heavy metals are particularly pronounced in areas with developed chemical or metallurgical industries [1].

The major sources of intoxication include air, soil and water [2]. In international practice, the term "environmental disease" has been officially recognized, associated with acute toxic changes in the blood, nervous diseases, and interference with the genetic structure of the cell [3]. As a result, mutagenic and carcinogenic damage to the immune system occurs.

The survey of heavy metal contents has been carried out for over 35 years in Bulgaria, mainly in areas with intensive industries, where 5 "hot spot" were established [1]. Burgas Region is also an ecologically endangered area whose problems are due to industrial production, the high growth of production and domestic waste, the growth and physical aging of the fleet.

Heavy metals include all metals with a relative atomic mass greater than 40 or more than 5 g/cm^3. Some of them, such as Cu, Zn, Mo, Co, Mn, and Fe, play an important role in the life of living organisms, others, such as mercury, lead, etc., are not biologically necessary.

Depending on the degree of danger to human health, heavy metals are divided into three groups (see Table 1). The metals of the first group are the most dangerous for human health [4]. The poisonous action of heavy metals on humans and animals is the greater the more soluble their compounds are in water and in fats. Diluted, they are easier to digest and show their toxicity. The water that reaches our home usually comes either from surface water (water from small rivers, streams or lakes) or underground water. About 80% of the tap water in Bulgaria comes from lakes, rivers or other sources on the surface. Underground water sources and municipal wells provide about 20% and the rest is from private wells.

Table 1. Groups of elements according to their harmfulness [4].

Group	Elements
I group	Hg, Cd, Pb, As, Zn, Ti
II group	Co, Ni, Mo, Cu, Cr
III group	Ba, V, Mn, Sr, Al

The most common chemical pollutants in drinking water are nitrates, pesticides, petroleum products and heavy metals due to different sources [5, 6]:

- Depending on the original source of drinking water;
- When it is due to human activity, agriculture, industry or water supply network;
- Drinking water may also be contaminated by contact with water supply.

Water quality can be assessed by various parameters such as Biochemical oxygen demand (BOD, also called biological oxygen demand), temperature, electrical conductivity, nitrate, phosphorus, potassium, dissolved oxygen, etc. Heavy metals such as Pb, Cu, etc. are of special concern because they produce water or chronic poisoning in aquatic animals.

The World Health Organization recommends that the maximum level of copper in drinking water should not exceed 2 mg/l (2 ppm) and the maximum level of lead in drinking water should not exceed 0.01 mg/l (10 ppb) [7].

According to the Bulgarian State Standard [8], the basic methods for determining the metals studied are:

- photometric and polarographic for copper (ISO 17.1.4.1980);
- photometric and polarographic for lead (ISO 17.1.4.2080).

For the determination of heavy metals in water such as Cu and Pb, the photometric and polarographic methods are recommended [8]. The photometric methods are inapplicable or less applicable in the presence of turbid or coloured solutions. In some cases, multiple filtration or searching for a clarification solution is necessary, which prolongs the analysis.

Voltammetry allows simultaneous determination of several metals with sufficient accuracy and sensitivity, which are characteristic of atomic absorption [9], and it is comparable to the sensitivity of neutron activation analysis [10]. Another advantage of the voltampermetric method is that it is safe and the cost of the analysis is comparatively lower. Its resolution is greater than the standard polarographic method for heavy metal analysis in water. Examples of determinations of Cu and Pb by Anodic Stripping Voltammetry (ASV) are given in the literature [11-15].

The goal of this work is to study the determination of copper and lead content in drinking and lake waters and to characterize the method of ASV in terms of accuracy, reproducibility and sensitivity in Cu and Pb analysis in these specified natural objects.

EXPERIMENTAL

Instrumentation. Voltammograms are recorded using an Ekotest –VA (Ekoniks-Ekspert, RF) computer-controlled voltammetric analyzer connected to a three-electrode cell. The electrode system is a three-in-one transducer designed as a single body electrochemical cell with a polycarbon indicator electrode, an auxiliary electrode and a reference electrode located in the same plane [16-18]. The combination of «3 in 1» electrode is a whole voltammetric 3-electrode cell in a single body. All component electrodes (work, auxiliary and reference electrodes) are placed coplanarly on top of the sensor. The indicator electrode surface is regenerated by polishing it with an ashless paper filter wetted with ethanol. Voltammograms are recorded in an alternating-current mode with alternating voltage amplitude. The pH is measured using an Ekspert 001, model 3 (0.1) pH meter/potentiometer (Ekoniks-Ekspert, RF) with a glass electrode.

Fig. 1. The set measurement of heavy metals in laboratory and field conditions.

Thermo Scientific Evolution 300 UV-Vis and Specol 11 spectrophotometers were used.

Reagents and solutions. All chemicals (Merck, Germany, high purity >99 %) are of analytical-reagent grade and employed without further purification. Double-distilled water was used in the preparation of the various solutions. The following reagents are used: HNO_3; $Hg_2(NO_3)_2 \times 2H_2O$; $CuSO_4 \times 2H_2O$; $Pb(NO_3)_2$; KCl. A stock solution of $Hg_2(NO_3)_2$ at a concentration of 5 g/l; a working solution of Hg^{2+} - 100 mg/l; a stock solution of Pb^{2+} - 25 mg/l; a Cu^{2+} stock solution - 25 mg/l. The working solutions of standard lead and copper additives have a

concentration of 1.25 mg/l. The concentrated supporting electrolyte solution is prepared as 50 ml of 0.01 M HNO_3 and 50 ml of 0.01 M $Hg_2(NO_3)_2$ are placed in a 250 ml flask and then diluted to the mark with double-distilled water. The concentrated HNO_3 supporting electrolyte solution is prepared as 50 ml of 0.01 M HNO_3 is transferred to a 250 ml flask and then diluted to the mark with double-distilled water. The diluted solution is prepared as 200 ml of concentrated supporting electrolyte solution is poured into a 1 ml flask and brought to the mark with double-distilled water.

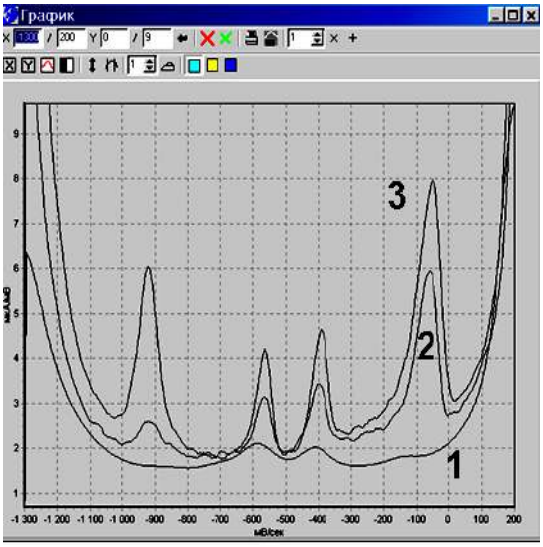

Fig. 2. Examples of measurement of zinc, cadmium, lead, copper with the complexes «Ecotest-VA- heavy metals». Samples: 1 - blank, 2 - tested sample, 3 - tested sample with standard additions [16].

Table 1. Optimal conditions for voltammetric measurements with the replacement of solutions using a three-in-one transducer.

Stage of analysis	Solution composition	Potential of the working electrode, E_w, mV	The time of exposing the electrode, t_{exp}, s
1.Electrochemical cleaning of the electrode	0.1M HNO_3	+100	100
2.Formation of the mercury film	$Hg(NO_3)_2.H_2O$ 100 mg/l, 0.1M HNO_3	-600	200
3.Electrochemical preconcentration of copper and lead	0.1M HNO_3 0.01M HNO_3	-600	200
4.Electrostripping of the concentrate	0.01M HNO_3 + sample	-1300…+400; potential sweep rate, 25 mV/s	300

Analytical procedure. 1 liter water sample was filtered and evaporated to 150 ml. 80 ml water sample was pipetted and transferred into 100 ml volumetric flask. Then 20 ml concentrated supporting electrolyte was added and the solution was homogenized. 25 ml from this solution was transferred in the glass vessel and 8 drops of 100 mg/l $Hg(NO_3)_2.H_2O$ were put in the vessel. The electrode was immersed into the solution and the analytes were pre-concentrated. The voltammograms were recorded. Consecutively, 1, 2 and 3 ml of standard additives of copper and lead (1.25 mg/l) solutions were added and voltammograms were recorded. The program calculated the areas of the peaks and gave the concentrations. All measurements were carried out at room temperature.

RESULTS AND DISCUSSION

Anodic stripping voltammetry is used to determine the concentration of Pb and Cu in the water samples. The method consists of a deposition potential that is more negative than the half-wave potential $E_{1/2}$ of the metals to be determined and an anodic scan to oxidize the reduced metal back into solution:

Deposition: $M^{n+} + ne^- = M(Hg)$

Stripping: $M(Hg) = M^{n+} + ne^-$

During deposition an amalgam is formed by the elemental metal and the mercury on the e electrode. The scan in the positive direction peak current is proportional to the concentration of the metal M. The sensitivity of the method arises due to the pre-concentration of the analyte species.

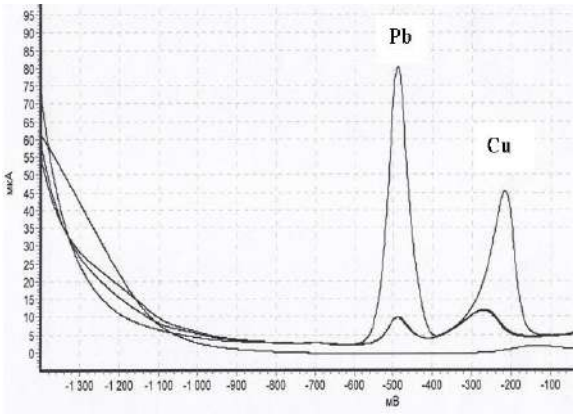

Fig. 3. Voltammograms of Pb and Cu with additives of standard solutions of lead and cooper

The maximum analytical signal of copper was found to be from -50 to -200 mV and the one for lead from – 400 to -500 mV at a rate of 25 mV/s in an alternating-current mode. The optimum current range was 2-200 μA. The optimal conditions for voltammetric measurements are given in Table 1.

Linear calibration graphs were obtained in a concentration range 10-500 μg/l for Cu^{2+}, and 30-500 μg/l for Pb^{2+}. The detection limit for copper ions is 0.5 μg/l (RSD=12%) and for lead ions is 0.1 μg/l (RSD=10%).

Table 2. Determination of copper (II) in environmental waters

Samples	Cu(II) found $\bar{x} \pm tS/\sqrt{n}$ (μg/l)	RSD $S_r = (S/\bar{x}) \times 100$ (%)
Drinking water	66.0 ± 5.6	7.34
Lake water	105.4 ± 6.4	1.37

The accuracy and precision of the voltammetric procedure were verified by the standard spectrophotometric method for determination of copper and lead ions in waters. The results obtained are given in Tables 2 and 3.

Table 3. Determination of lead (II) in environmental waters

Samples	Pb(II) found $\bar{x} \pm tS/\sqrt{n}$ (μg/l)	RSD $S_r = (S/\bar{x}) \times 100$ (%)
Drinking water	5.7 ± 0.4	6.35
Lake water	9.5 ± 0.7	6.36

Number of determination $n= 5$; t - Students t-value at 95% probability; S - standard deviation; $\bar{x}$, an average.

The concentrations of copper and lead in various water samples were found to be lower than the drinking water contamination standards issued by the World Health Organization.

CONCLUSIONS

Anodic stripping voltammetry has been developed for the simultaneous determination of copper (II) and lead (II) in drinking and lake waters. Under the optimal conditions alternating-current voltammograms were recorded and the concentration of copper and lead ions were determined by standard addition method. The results obtained are in agreement with those of the standard spectrophotometry method.

REFERENCES

1. Staykova, P. and V. Naydenova. Proceedinds of the anniversary scientific conference of ecology, Plovdiv, 2008, p. 551.
2. Enciclopedia www.greenstudentu.com/ encyclopedia/pollution. Accessed 2/17/2010.
3. Lawrence Wilson M.D. *Toxic metals in human health and disease" (© Revised, July 2008, The Center for Development)*- http://www.drlwilson.com/Articles/TOXIC%20METALS.htm
4. Stoyanov, S. *Heavy metals in the environment and food products. - Toxic damage to the person, clinical picture, treatment and prophylaxis. Pensoft Publishing House, Sofia, (1999).*
5. European Council Directive 98/83/EC of 3 November 1998 on the quality of water intended for human consumption, Values of Annex 1, Part B, (1998).

6. Unicef, Common water and sanitation-related diseases. (2003). Available http://www.unicef.org/wash/index_wes_related.html
7. WHO/FAO/IAEA. *Trace Elements in Human Nutrition and Health, "World Health Organization", Geneva, 1996.*
8. Manual. *Bulgarian State Standards, Ed., Standardization, Sofia, 1989.*
9. Bond, A. M. *Electroanalytical methods, ed. Scholtz, Moscow, Binom, 2006.*
10. Drugov Y.S. and A.A. Rodin. *Ecological Analytical Chemistry, St. Petersburg, Anatolia, 2002.*
11. Ensafi, A.A., T. Khayamian, A. Benvildi and E. Mirmontaz. *Anal. Chim. Acta*, **561**, (2006), p. 225.
12. Merkoçi, A., M. Vasjari, E. Fàbregas and S. Alegret. *Microchim. Acta*, **135**, (2000), p.29.
13. Martiniano, L.C., V. R. Abrantes, S. Y. Neto, E. P. Marques, T.C.O. Fonseca, L.P. Paim, A. G. Souza, N. R. Stradiotto and R. Q. Aucélio. *Fuel*, **103**, (2013), p. 1164.
14. Mahesar, S.A., S.T.H. Sherazi, A. Niaz, M.I. Bhanger, S. Uddin and A. Rauf. *Food Chem. Toxicol.* **48**, (2010), p.2357.
15. Jakmunee, J. and J. Junsomboon. *Talanta*, **77**, (2008), p. 172.
16. Zaitsev, N.K., E. B. Sviderskii and V.V. Yuritsyn RF Patent 2 239 825, (2004).
17. Zaitsev, N.K., E.A. Osipova and E. B. Sviderskii, *J. Anal. Chem.* **59**, (2004), p. 649.
18. Shvedene N.V., V.V. Sviridov, N.K Zaitsev, M.V. Roslova and I.V. Pletnev. *Moscow University Chem. Bulletin*. **67**, (2012), p. 192.

ANNUAL OF ASSEN ZLATAROV UNIVERSITY, BURGAS
BULGARIA, 2017, v. XLVI (1)

POROUS TEXTURE ASSESSMENT OF ACTIVATED CARBONS DERIVED FROM WALNUT SHELLS THROUGH CHEMICAL ACTIVATION

Lenia Gonsalvesh, Stancho Pavlov, Mariana Tavlieva, Velyana Georgieva
E-mail: lenia_gonsalvesh@abv.bg

ABSTRACT

On the basis of N_2 adsorption-desorption isotherms measured at –196°C by an automatic apparatus Surfer (Thermo Scientific), the porous texture characteristic of activated carbons (ACs) derived from agro-waste, i.e. walnut shells, through chemical activation are elucidated. For the purpose different calculation procedures are applied. From the tested reagents for chemical activation, $ZnCl_2$ promotes additional development of micro- and mesopores and respectively higher S_{BET} for AC prepared by it. The latter is characterized as predominantly microporous AC with S_{BET} and S_{micro} of 553 and 468 $m^2 g^{-1}$, respectively, and $V_{0,95}$ and V_{micro} of 0.2652 and 0.1982 (6.6 %RSD) $cm^3 g^{-1}$, respectively. By the application of different approaches more reliable results for V_{micro} with their uncertainties can be reported. Pore size distribution assessed by applying NLDFT theory reveal monomodal micropore volume distribution (pore width of 1.68 nm) for ACs prepared through chemical activation by $ZnCl_2$.

Key words: *activated carbon, chemical activation, N_2 adsorption isotherms, porous structure*

INTRODUCTION

The production of nano-porous materials, i.e. activated carbons (ACs), with various and specific physicochemical properties can be tailored with a suitable carbon rich precursor and appropriate process parameters selection. In general, any carbon rich organic materials can be converted into AC. In the 1990s wood, peat, coal and coconut shells were among the most widely used precursors, the best one being the expensive anthracite [1, 2]. In the last decade, since scientific interest has been focused towards valorization and recycling of different waste, the production of low-cost ACs from carbon containing waste materials, i.e. "End-of-Life" tyres [3-6], polymeric wastes [2, 7], biomass wastes [8-11], etc, gained importance. A variety of experimental strategies for production of ACs have been explored, which, however, can be classified into two clearly defined groups [1]: i) thermal (physical) activation consisting of two consecutive steps, i.e. carbonization (produces char rich in carbon) and activation (partially gasification of char with an oxidizing agent, i.e. steam or CO_2); and ii) chemical activation mostly carried out in a single stage as prior carbonization the raw material is impregnated with a chemical agent. In the literature there are a number of publications related to impregnation of lignocellulosic materials with different activating reagents such as $ZnCl_2$, H_3PO_4, H_2SO_4, $CaCl_2$, $KMnO_4$, NaOH, K_2CO_3, etc. before their thermochemical conversion into ACs [12]. Among the activation agents used, $ZnCl_2$ is one of the most effective for production of micro- or meso-porous carbons due to its high activation ability and relatively low cost. This type of chemical activation destabilizes the lignocellulosic structure due to hydrolysis reactions, which increase the elasticity of the precursor particles, and in a subsequent heating process AC with a well developed porosity and a high specific surface is produced [1]. In fact, the activation agent promotes and/or assists the formation of micro- and mesopores, and carbons with increased adsorption capacity compared to physically activated carbons are produced.

Nowadays, agro-wastes are considered as sustainable, ecologically friendly and economically feasible renewable resources for production of ACs with well developed porous structure (dominantly microporous in most cases). Such ACs have been successfully applied in different fields, as adsorption of pollutants [8, 9], catalyst supports in heterogeneous catalysis [10, 11], gas

storage and separation [13]. However, the efficient and specific application of ACs as adsorbent or catalyst support is strongly determined by their physicochemical properties. In this regard, porous texture characteristics such as specific surface area, pore volumes and pore sizes distribution are important factors to be considered. Among the various characterization techniques, gas adsorption has been shown to be sufficient for evaluation of porous texture parameters of micro- and mesoporous materials [1, 14-16]. However, elucidating the porous texture of different materials is not always straightforward. The developed methods, computational procedures and models for porous structure assessment through gas adsorption are based on different assumptions, which could result in underestimation or overestimation of the final results. Therefore in order to obtain the most reliable results for the parameters characterizing the porous structure, different mathematical approaches and computational procedures should be applied and compared.

The aim of the current research is the production of ACs from agro-waste (walnut shells), through chemical activation by NaCl or $ZnCl_2$ solutions and assessment of the influence of the nature of activation reagent on the porous structure of prepared materials.

EXPERIMENT

In the current study walnut shells (WS) were valorized and used as carbon precursor feedstocks for production of ACs. Prior to use, the air-dried biomass sample was ground in a high-speed rotary cutting mill, sieved (< 2 mm) and oven dried at 110ºC. The impregnation of the biomass waste is carried out with two different activating reagents, i.e. 2 wt.% $ZnCl_2$ or 2 wt.% NaCl solutions, at room temperature and continuous stirring for 6 hours. After this treatment the samples were filtered and washed with deionized water up to lack of chloride ions in the filtrates and then dried for 6 hours at 105 °C. The raw WS sample and impregnated with 2 wt.% $ZnCl_2$ and 2 wt.% NaCl samples were subjected to carbonization or the so-called slow pyrolysis in inert atmosphere in a lab-scale muffle furnace at slow heating rate of 10°C min^{-1} up to pyrolysis temperature of 500°C kept further isothermal for 1 h. The obtained products after carbonization of the raw WS sample and impregnated with 2 wt.% $ZnCl_2$ and 2 wt.% NaCl samples are respectively denoted as Wchar, W-AC_{ZnCl2} and W-AC_{NaCl}.

The porous structure characterization was carried out by measuring N_2 adsorption isotherms at –196°C on an automatic apparatus Surfer (Thermo Scientific). The specific surface area S_{BET} of bio-chars is determined by using N_2 adsorption data in the range of P_i/P_0 up to 7.3×10^{-2} (isotherms of Type I) and the linear form of *BET* equation [17-19]. The total pore volume, known as volume of *Gurvich*, is determined based on the volume of adsorbate $V_{0,95}$, recorded on the desorption branch of the adsorption isotherm at a relative pressure P_i/P_0 = 0.95. The micropore volume ($V_{DR,micro}$) is calculated by using the Dubinin-Radushkevich equation up to $P_i/P_0 \leq 0.16$ and *V–t* plots [14-16, 20, 21]. The pore size distribution and pore diameters L_0 are obtained by applying the Non Local Density Functional Theory (NLDFT) on data of adsorption branch of N_2 isotherms [21].

RESULTS AND DISCUSSION

According to IUPAC classification, the recorded N_2 adsorption isotherms of W_{char}, W-AC_{ZnCl2} and W-AC_{NaCl} samples (Fig. 1) represent Type I isotherm and reflect the significant role of microporous structure on the adsorption process. At high P_i/P_0, a hysteresis loop of H4 type appears in the isotherms, which is attributed to the presence of some mesopores as well. Clearly, the type of activating agent affects the porosity of prepared ACs – W-AC_{ZnCl2} sample demonstrates much higher N_2 adsorption capacity compared to W_{char} and W-AC_{NaCl}, while N_2 adsorption capacity of W_{char} and W-AC_{NaCl} samples is rather comparable. Consequently higher S_{BET} and $V_{0.95}$ are calculated for activated with $ZnCl_2$ AC sample (Table 1).

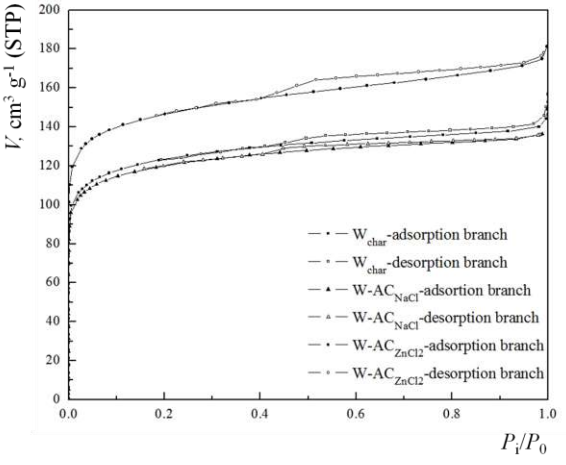

Fig. 1. N_2 adsorption isotherms of investigated samples

Table 1. Textural properties of prepared porous materials

Parameters	Calculation method		Sample		
			W_{char}	W-AC_{NaCl}	W-AC_{ZnCl2}
$V_{0.95}$ (cm^3 g^{-1})	*Gurvich*		0.2148	0.2076	0.2652
S_{BET} (m^2 g^{-1})	*BET*		463	450	553
C			6357	7013	8367
$V_{DR, micro}$ (cm^3 g^{-1})	*DR*		0.1799	0.1774	0.2133
$V_{DR, meso}$ [a] (cm^3 g^{-1})			0.0349	0.0302	0.0519
$V_{t, micro}$ (cm^3 g^{-1})	*V–t* plot	*Halsey*	0.1578	0.1523	0.1716
		npFCB	0.1694	0.1641	0.1914
		npCB	0.1693	0.1639	0.1899
$V_{t, meso}$ [b] (cm^3 g^{-1})		*Halsey*	0.057	0.0553	0.0936
		npFCB	0.0454	0.0435	0.0738
		npCB	0.0455	0.0437	0.0753
$S_{t, ext}$ (m^2 g^{-1})		*Halsey*	68	68	108
		npFCB	54	53	84
		npCB$_2$	54	53	86
$S_{t, micro}$ [c] (m^2 g^{-1})		*Halsey*	395	382	445
		npFCB	409	397	469
		npCB	409	397	467
L_0 [d] (nm)	*NLDFT (n2c77K_cyl)*		1.49 (10)	1.68 (90)	1.68 (92)
			1.78 (48)	2.82 (4)	2.82 (2)
			1.99 (34)	3.55 (6)	3.55 (6)
			3.76 (3)		
			4.73 (5)		

[a] –$V_{meso} = V_{0.95} - V_{DR,micro}$; [b] –$V_{t, meso} = V_{0.95} - V_{t, micro}$; [c] –$S_{t, micro} = S_{BET} - S_{t, ext}$;
[d] –in brakets is the approximated content in rel. %.

Porosity and especially microporosity assessment is a challenging task. Very often the applied approaches for micropore volume calculation from N_2 adsorption isotherms give significantly different results, which are especially pronounced for highly activated carbons with a wide micropore size distribution [22]. To overcome this problem different calculation approaches and application of various adsorptives and measurements over a wide range of temperature and pressure with more attention towards the kinetics of adsorption and desorption and to fluid transport within pores are suggested [23]. In order to obtain more reliable assessment of porosity, in the current research the application of *DR* equation and *V–t* plots to N_2 adsorption isotherms of the investigated ACs is performed.

Dubinin, in collaboration with Raduskevich, presents an equation for calculation of micropores volume based on the range of low and average relative pressures of the N_2 adsorption isotherm, $10^{-4} < P_i/P_0 < 0.1$ [14, 17]. Their model is an adaptation of the previously developed by Polany potential theory for adsorption on a homogeneous, equipotential adsorbent`s surface and persorption theory. According to Dubinin, the adsorption process in microporous structures is expressed in volumetric filling of micropores, without the realization of mono- and multilayers. The linear equation of Dubinin-Radushkevich

(*DR*), describing the adsorption in microporous adsorbents and catalysts, has the following form:

$$\lg V_i = \lg V_{DR,micro} - D\left(\lg P_0/P_i\right)^2, \quad (1)$$

where V_i is the adsorbed amount at given P_i/P_0, expressed as volume of the liquid adsorbate, $V_{DR,micro}$ is the volume of the micropores and D is represented by the following equation:

$$D = B\left(\frac{T}{\beta}\right)^2, \quad (2)$$

where B and β are physicochemical constants reflecting the specific nature of the adsorbent and the adsorbate. According to Eq. (1), ordinate intercept is equal to $\lg V_{DR,micro}$, from which the value of the micropores volume $V_{DR,micro}$ can be calculated, while the slope of the regression line gives the parameter D.

V–t plot method as described by Lippens and de Boer [24] is a technique which compares an isotherm of a porous material with a standard type II isotherm (of non-porous material). In this approach, initially *t*-standard curve is prepared based on data of non-porous material with *BET C* constant similar to that of investigated porous sample and then the isotherm of the later is re-drawn as a plot of the gas adsorbed vs. statistical layer thickness, *t*, of the non-porous material at the corresponding P_i/P_0 [15]. The application *V–t* plot approach makes it possible to determine micropore volume and external (mesopore) surface area. In the case of N_2 adsorption, the statistical layer thickness, *t*, of the adsorbed film on a non-porous material can be calculated as follow:

$$t = 0.354\frac{W_a}{W_m} \text{ [nm]}, \quad (3)$$

where W_a is the adsorbed weight, W_m is the adsorbed weight corresponding to formation of a monolayer and 0.354 nm is N_2 monolayer depth [15]. However, based on *t*-standard curves obtained from N_2 adsorption isotherms of non-porous materials, empirical thickness equations describing the relation between t and P_i/P_0 have been computed. In the current study two thickness equations, i.e. *Halsey* equation and equation developed on the base of non-porous furnace carbon black (*npFCB*), described bellow respectively as Eq. (4) and Eq. (5), are employed. Additionally, based on the N_2 adsorption data for *t* of non-porous carbon blacks (*npCB*) presented by Kaneko et. al. [25], an empirical equation, i.e. Eq. (6), was also derived and employed in the current research.

$$t = 0.354\left[\frac{-5}{\ln\left(\frac{P_i}{P_0}\right)}\right]^{\frac{1}{3}} \text{ [nm]} \quad (4)$$

$$t = 0.088\left(\frac{P_i}{P_0}\right)^2 + 0.645\left(\frac{P_i}{P_0}\right) + 0.298 \text{ [nm]} \quad (5)$$

$$t = 0.27091 + 1.37941\left(\frac{P_i}{P_0}\right) - 4.78724\left(\frac{P_i}{P_0}\right)^2 + 13.46039\left(\frac{P_i}{P_0}\right)^3 - 16.57504\left(\frac{P_i}{P_0}\right)^4 + 7.56665\left(\frac{P_i}{P_0}\right)^5 \text{ [nm]} \quad (6)$$

The *DR* plots as well as *V–t* (based on *npFCB*) plots of investigated samples with their respective fits are presented on Fig. 2 and 3. The calculated porosity parameters by applying *DR* and *V–t* plots approaches are included in Table 1.

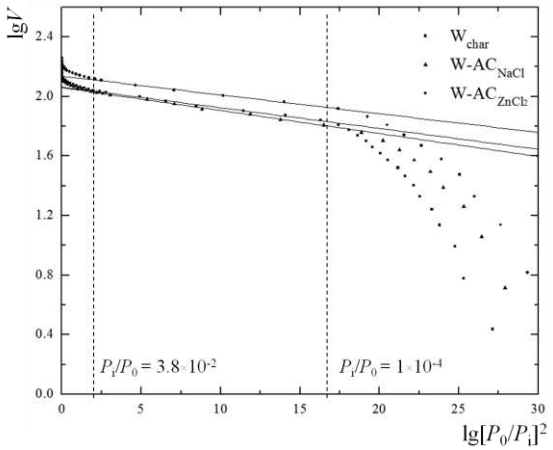

Fig. 2. *DR* plots of investigated samples with their respective fits

The porous texture parameters, gathered in Table 1, reflect the predominant microporous nature of the investigated samples. The calculated $V_{DR,micro}$ significantly prevails $V_{DR,mezo}$ for all samples and varies in the range of 0.1774 – 0.2133 $cm^3\ g^{-1}$. The highest value for $V_{DR,micro}$ is calculated for AC prepared after impregnation with $ZnCl_2$, which is in accordance with the magnitude of S_{BET} and $V_{0.95}$ of that sample. Obvious-ly, the chemical activation may lead to additional enlargement of porous texture of WS based ACs as the nature of the used activation reagent has a significant impact: $ZnCl_2$ acts as a better chemical reagent for production of WS

based AC since it promotes additional development of micro- and mesopores and respectively higher S_{BET}; the influence of NaCl is rather insigni-ficant.

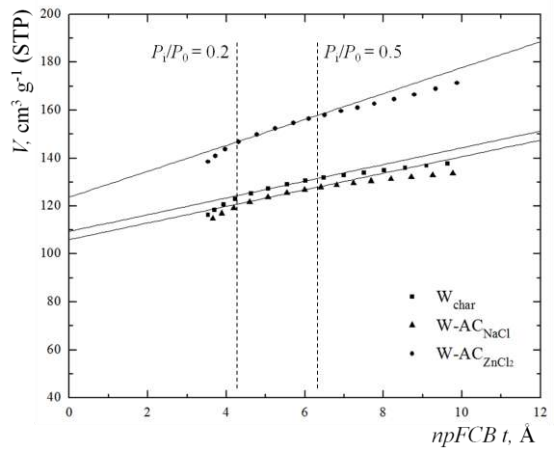

Fig. 3. *V–t* (*npFCB*) plots of investigated samples with their respective fits

By using any of *V–t* plots, i.e. *t* calculated based on Eq. (4), (5) or (6), the same peculiarities in the magnitude of V_{micro} of investigated samples are observed. Nevertheless, the results for V_{micro} obtained by *V–t* plots differ to those obtained by *DR* plots/equation. The largest differences are revealed when *Halsey* equation (Eq. (4)), developed for silica, alumina and other oxides, is used for calculation of statistical layer thickness *t* and construction of *V–t* plots. On the contrary, by using the *V–t* plots in which *t* is calculated on the basis of the equations developed for *npFCB* and *npCB*, the calculated $V_{t,micro}$ values for investigated samples are identical between each other and substantially similar to those obtained by *DR* equation. This demonstrates the importance of the non-porous reference material selected for the construction of the *V–t* plot and calculation of pore texture parameters – a non-porous reference material with similar chemical composition and *BET C* constant to that of investigated porous samples should be employed [15, 16, 26]. Thus, based on *V–t* plots constructed by using non-porous carbon reference materials and *DR* equation, V_{micro} of 0.1729 (3.5 %RSD), 0.1703 (3.9% RSD) and 0.1982 (6.6 %RSD) cm^3 g^{-1} can be reported for W_{char}, W-AC_{NaCl} and W-AC_{ZnCl_2} samples, respectively.

Pore size distribution (PSD) assessed applying NLDFT theory on N_2 adsorption isotherms of investigated samples is presented on Fig. 4. For NLDFT computation the n2c77_cyl kernel, developed for carbon micro- and mezoporous materials based on a cylindrical pore model, is used since the theoretical adsorption isotherms described by using this kernel are in best agreement with the registered experimental adsorption isotherms of the samples. The maximums in the PSD curve correspond to the prevailing pore sizes of the investigated samples. The registered pore widths are in the range of 1.49 to 4.73 nm. The PSD confirms once again the predominance of micropore structure for investigated samples as over 90% of registered pore sizes are in the range of micropores (< 2 nm), with trimodal micropore volume distribution for W_{char} sample (maximums at 1.49, 1.78, 1.99 nm) and monomodal micropore volume distribution for W-AC_{NaCl} and W-AC_{ZnCl_2} ACs (maximum at 1.68 nm).

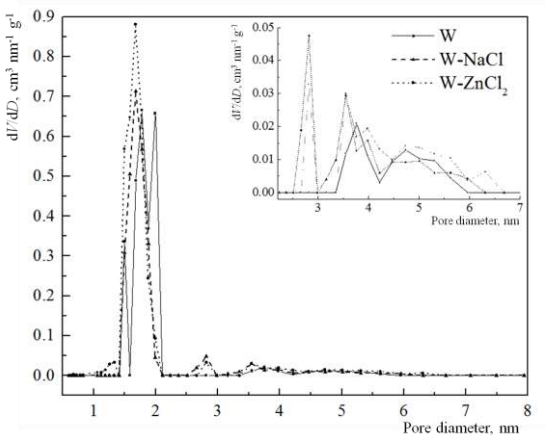

Fig. 4. Pore size distribution of investigated samples

CONCLUSIONS

In the current research the influence of the activation reagents on the porous structure of ACs derived from agro-waste WS is revealed. From the tested activation reagents, $ZnCl_2$ acts as a better chemical reagent for production of WS based AC, since it promotes additional development of micro- and mesopores and, respectively, higher $S_{BET.}$ By the application of different approaches more reliable results for V_{micro} with their uncertainties can be reported.

REFERENCES

1. Bandosz, T.J., Activated Carbon Surfaces in Environmental Remediation, Elsevier, 2006.
2. Stoycheva, I.G., et al., *Water, Air, & Soil Pollution*, 227 (2016) p. 452.
3. Gonsalvesh, L., et al., *Bulgarian Chemical Communications*, 49 (2017) p. 75.
4. Acevedo, B., C. Barriocanal, *Fuel Processing Technology*, 134 (2015) p. 275.

5. Acevedo, B., et al., *Fuel*, 151 (2015) p. 83.
6. Saleh, T.A., V.K. Gupta, *Advances in Colloid and Interface Science*, 211 (2014) p. 93.
7. Gonsalvesh, L., et al., *Fuel Processing Technology*, 149 (2016) p. 75.
8. Gonsalvesh, L., et al., *Journal of Chemical Technology & Biotechnology*, 91 (2016) p. 1585.
9. Gonsalvesh, L., et al., *Advances in Environmental Research*, 6 (2017) p. 95.
10. Tsoncheva, T., et al., *Journal of Porous Materials*, 22 (2015) p. 1127.
11. Tsoncheva, T., et al., *Microporous and Meso-porous Materials*, 217 (2015) p. 87.
12. Yahya, M.A., et al., *Renewable and Sustainable Energy Reviews*, 46 (2015) p. 218.
13. Bader, N., A. Ouederni, *Journal of Energy Storage*, 5 (2016) p. 77.
14. Gregg, S.J., K.S.W. Sing, Adsorption, Surface Area and Porosity, Academic Press, London, 1982.
15. Lowell, S., et al., Characterization of Porous Solids and Powders: Surface Area, Pore Size and Density, Kluwer Academic Publishers, 2004.
16. Thommes, M., et al., Physisorption of gases, with special reference to the evaluation of surface area and pore size distribution (IUPAC Technical Report), in: Pure and Applied Chemistry, 2015, p. 1051.
17. ISO 9277:2010, Determination of the specific surface area of solids by gas adsorption-BET method, 2010.
18. Brunauer, S., et al., *Journal of the American Chemical Society*, 60 (1938) p. 309.
19. Vlaev, L., Adsorption and Catalysis, Baltika-2002, Burgas, 2014.
20. Stoeckli, F., et al., *Carbon*, 39 (2001) p. 1115.
21. IBS ISO 15901-3:2007, Pore size distribution and porosity of solid materials by mercury porosimetry and gas adsorption-Part 3: Analysis of micropores by gas adsorption 2007.
22. Selles-Perez, M.J., J.M. Martin-Martinez, *Fuel*, 77 (1991) p. 877.
23. Sing, K.S.W., *Carbon*, 27 (1989) p. 5.
24. Lippens, B.C., J.H. de Boer, *Journal of Catalysis*, 4 (1965) p. 319.
25. Kaneko, K., *Journal of Membrane Science*, 96 (1994) p. 59.
26. Sing, K.S.W., et al., Assessment of Microporosity, in: Adsorption by Powders and Porous Solids (Second Edition), Academic Press, Oxford, 2014, p. 303.

ANNUAL OF ASSEN ZLATAROV UNIVERSITY, BURGAS
BULGARIA, 2017, v. XLVI (1)

SOFTWARE FOR PROCESSING DATA FROM N_2 ADSORPTION MEASUREMENTS

Stancho Pavlov, Lenia Gonsalvesh
E-mail: stancho_pavlov@yahoo.com

ABSTRACT

In this paper, a program especially designed for processing N_2 adsorption data obtained at 77K by Surfer apparatus (Thermo Scientific) is presented. The program is written in Delphi. It allows the determination of porous texture characteristics: i) specific surface area S_{BET} by using the linear form of BET equation; ii) the total pore volume ($V_{0.95}$), known as volume of Gurvich; iii) the micropore volume ($V_{DR,micro}$) by using the Dubinin-Radushkevich equation; and iv) pore size distribution by using Pierce method. In the paper the program functions, structure and the way of working are described.

Key words: *Delphi programming, N_2 adsorption data, porous texture characteristics*

INTRODUCTION

The characterization of the porous structure of adsorbents and heterogeneous catalysts generally employs adsorption methods. For the purpose, adsorption of N_2 at 77 K at different relative pressures is most often applied. Based on the obtained N_2 adsorption-desorption data and using a particular mathematical apparatus and computational procedures, the values of the basic parameters characterizing the porosity, i.e. specific surface are $S_{BET,}$ the total pore volume ($V_{0.95}$), micropores volumes ($V_{DR,micro}$), the average radius of pores and pore volume distribution by size, can be determined. In the current paper, a program especially designed for processing N_2 adsorption data obtained at 77 K and calculation of the main parameters characterizing the porous texture is presented.

EXPOSITION

The theory, mathematical apparatus and computational procedures used for calculation of porosity parameters with the developed program are described in: i) [1-3] for specific surface are $S_{BET,}$ the total pore volume ($V_{0.95}$), micropores volumes ($V_{DR,micro}$), the average radius of pores; and ii) [4] for pore size distribution by using Pierce method.

The initial/raw data for N_2 adsorption at 77 K obtained by Surfer apparatus (Thermo Scientific) represented as Excel like "cvs" file in nineteen columns is loaded in the prepared program. The opening and reading of the data in this “csv” file are accomplished successively by the following procedures:

- ReadTxt(FileNameFV:string;var StrArr:TStrArr;var n,m:integer);
- TFrmAddsrb.MIOpenClick(Sender: TObject).

The first procedure gets the file name and returns an array of strings, their number of rows and columns, while the second one puts the data in a string grid with a name "StrngGrdRdnTxt". The adsorption data are separated from desorption data by the sign "Des" in the first column of the string area. An overview of the Tab Sheet “Data” which represents a table with the loaded raw N_2 adsorption-desorption data obtained by Surfer apparatus is shown in Fig. 1. On this Tab Sheet construction of N_2 adsorption-desorption isotherm is also possible. For the purpose the data for relative pressure P_i/P_0 included in column (12) and adsorbed volume of N_2 in $cm^3\ g^{-1}$ included in column (16) should be used by applying the main menu options “Graphic>View Isotherm” (an overview of main menu options is given in Fig. 2). These data are used and introduced in the other Tab Sheets constructed for determination of specific surface are S_{BET} (Tab Sheet “S bet”), micropores volumes ($V_{DR,micro}$) (Tab Sheet “DR”), and pore volume distribution by size (Tab Sheets “Adsorption” and “Desorption”).

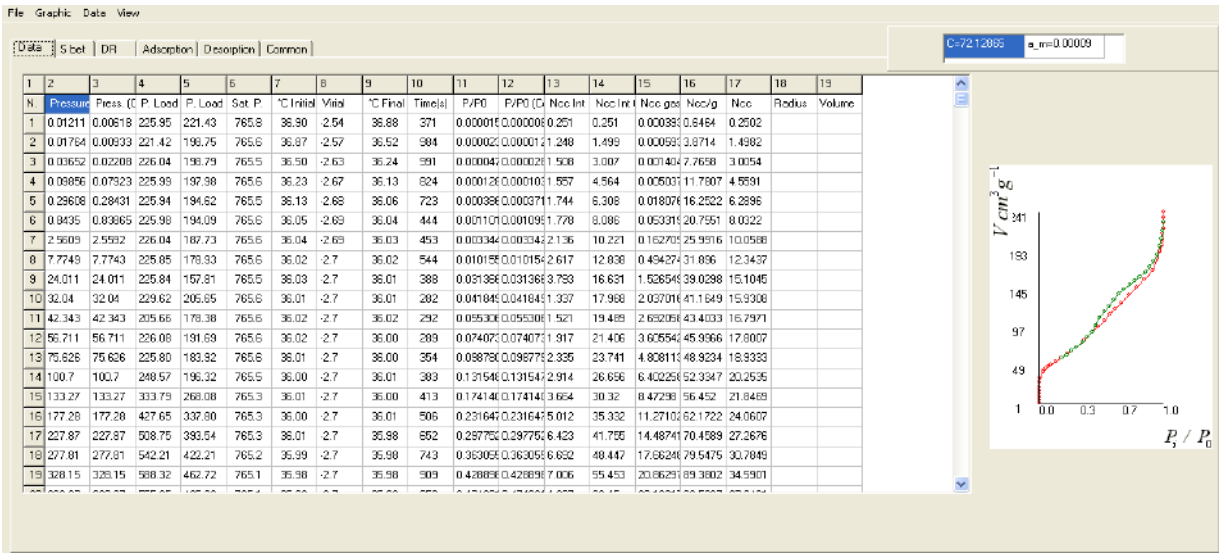

Fig. 1. An overview of Tab Sheet "Data"

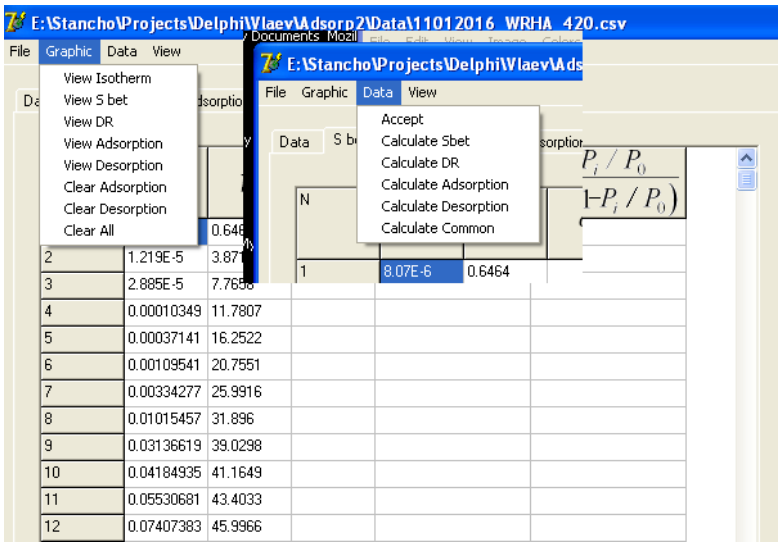

Fig. 2. An overview of main menu options

The second Tab Sheet (Fig. 3), i.e. "S bet", is designed for calculation of S_{BET} by using N_2 adsorption data and the linear form of *BET* equation (Eq. 1). Inasmuch as linear *BET* range for micro- and mesoporous materials appears in a different range of relative pressures, a window in which to set the relative pressure range for *BET* fitting is provided. In general, the linear *BET* range for microporous material is determined based on criteria of *Rouquerol* [2]. Therefore, the graphical representation of the latter is included in this Tab Sheet as well. When the mouse cursor moves through the curve of this graph the local coordinates are displayed. Thus, the P_i/P_0 at which $\alpha(1-P_i/P_0)$ is maximal can be clearly seen. After setting the linear range for *BET* fitting the graphical presentation of linear form of the *BET* equation can be drawn. Trough linear regression y=ax+b, the determination of monolayer capacity α_m and physicochemical constant C can be accomplished (see Eq. 1). The monolayer capacity α_m and physicochemical constant C based on which the S_{BET} is calculated, together with calculated S_{BET} appear in a window next to the graphs.

$$\frac{P_i/P_o}{\alpha_i\left(1-P_i/P_o\right)}=\frac{(C-1)}{\alpha_m C}\frac{P_i}{P_o}+\frac{1}{\alpha_m C}, \qquad (1)$$

where, α_i is the amount of adsorbed N_2 at a certain P_i/P_0, α_m is the monolayer capacity, C is a physicochemical constant standing in relation to the heat of adsorption of the adsorbate. According to Eq. (1), ordinate intercept is equal to $1/\alpha_m C$, while the slope of the regression line gives $(C-1)/\alpha_m C$. Including the slope and ordinate intercept in a system of two equations of the

first degree with two unknown parameters, the values of the constants C and α_m can be calculated. Determination of α_m gives the opportunity to calculate the specific surface of a porous sample using the equation:

$$S_{BET} = \alpha_m N_A \omega, \qquad (2)$$

where: N_A is Avogadro's number, 6.023×10^{23} 1/mol, and ω is the effective cross section area of the adsorbent molecule, which for the nitrogen molecule is about 16.27Å^2.

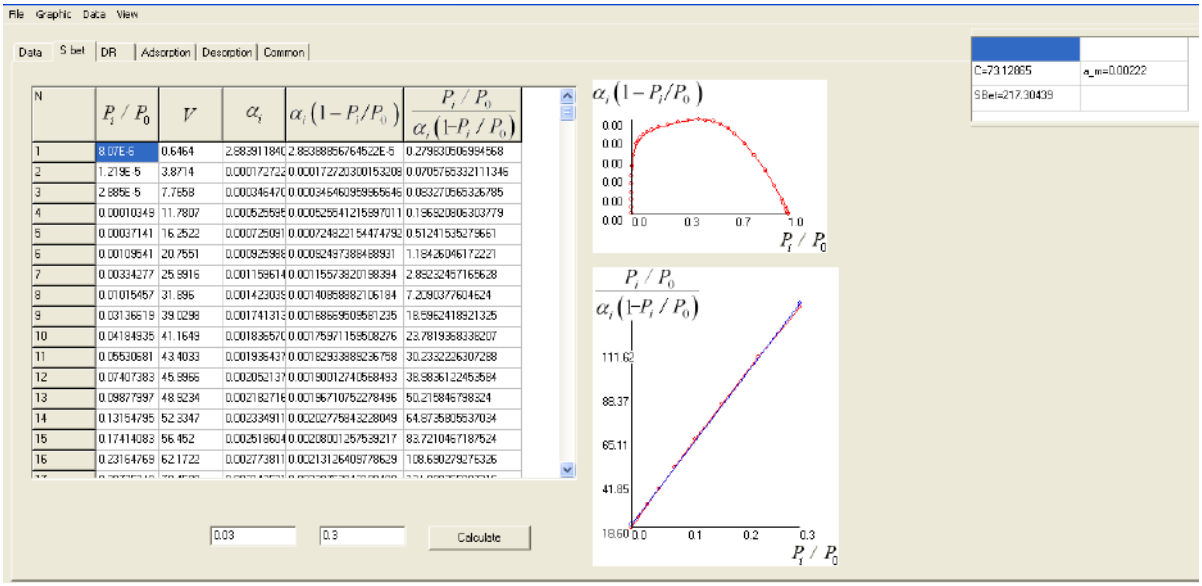

Fig. 3. An overview of Tab Sheet "S bet"

The management of Tab Sheet "DR" is quite similar to "S bet" one. However in it, the linear equation of Dubinin-Radushkevich (*DR*) (Eq. 3), describing the adsorption in microporous adsorbents and catalysts, is processed:

$$\lg V_i = \lg V_{DR,micro} - D\left(\lg P_0/P_i\right)^2, \qquad (3)$$

where V_i is the adsorbed amount at given P_i/P_0, expressed as volume of the liquid adsorbate, $V_{DR,micro}$ is the volume of the micropores and D is represented by the following equation:

$$D = B\left(\frac{T}{\beta}\right)^2, \qquad (4)$$

where B and β are physicochemical constants reflecting the specific nature of the adsorbent and the adsorbate. According to Eq. (3), ordinate inter-cept is equal to $\lg V_{DR,micro}$, from which the value of the micropores volume $V_{DR,micro}$ can be calculated, while the slope of the regression line gives the parameter D.

Tab Sheets "Adsorption" and "Desorption" (Fig. 4) compute pore volume distribution by size (PSD) by using respectively adsorption and desorption isotherm branches and Pierce method described in details in Gonsalvesh et al. [4]. Inasmuch as this method employs calculation of statistical layer thickness, t, the two most common equations for t calculation are introduced within the options, i.e. de Boer equation (Eq. 5) and Halsey equation (Eq. 6).

$$t = 0.1\sqrt{\frac{13.99}{(0.034 - 0.4343\ln\left(\frac{P_i}{P_0}\right)}} \text{ [nm]} \qquad (5)$$

$$t = 0.354\left[\frac{-5}{\ln\left(\frac{P_i}{P_0}\right)}\right]^{\frac{1}{3}} \text{ [nm]} \qquad (6)$$

Trough restriction Edits, i.e. "EdtAdsFrom" and "EdtAdsTo" in case of PSD calculation based on adsorption isotherm branch, and "EdtDesFrom" and "EdtDesTo" in case of PSD calculation based on desorption isotherm branch, the P_i/P_0 interval of interest for calculation is settled. The calculations are carried out within this interval only. The determination of the demanded values takes place by the main menu options, i.e. "Data>Calculate Adsorption" for PSD calculation based on adsorption isotherm branch (Tab Sheet "Adsorption") and "Da-

ta>Calculate Desorption" for PSD calcu-lation based on desorption isotherm branch (Tab Sheet "Desorption"), by using the procedure CalcAds_Des(var Ads_DesF:TAds_Des). After performing the calculation according to Pierce method the graphical representation of PSD by plotting $\Delta V_{p,i}/\Delta r_{p,i}$ *vs.* $r^*_{p,i}$ is possible by using the main menu options "Graphic>View Adsorption" or "Graphic>View Desorption". The procedure TFrmAddsrb.Graphics(KindF.string) is responsible for graphic representation of PSD data. The last mentioned procedure works differently according to the argument string.

Two main types of data are declared in the units "Adsorption.pas", PsAdsorp.pas", "Files.pas", "Matrix.pas" and "PsSplScr.pas" based on which the program is developed. The main unit responsible for calculations within the program is "Adsortion.pas", part of which is given bellow:

```
type TStGraphic=class(TObject)
  m_N:integer;
  XMax_Min,YMax_Min: array[1..2] of real;
  m_Arr:array [1..cMaxDim] of TRPoint;
  m_Kind:string;
  constructor Create;
  destructor Destroy();override;
  procedure Drow(var
XMaxF,XMinF:real;bUseXMaxMin:boolean;
    var
YMaxF,YMinF:real;bUseYMaxMin:boolean;ColorF:TColor;Fram
eF:integer;
     var ImgF:TImage);
end;
type TAds_Des=record
  mGrXMaxMin,mGrYMaxMin: array[1..2] of real;
  m_N,iFrom,iTo,m_Frame:integer;
  m_Arr:array [1..cMaxDim] of TRPoint;
  m_Res:array [1..cMaxDim,1..18] of real;
  m_Kind:string;
end;
```

and several variables:

```
StGraphicG:TStGraphic;
 AdsorpG,DesorpG,SbetG,DRG:TAds_Des;
 VariantG:integer;
 bHaveData:boolean;
 FrmtG:string;
```

The program dependences are given in Table 1.

Table 1. Program dependences

Main procedure	Subprocedures	
FormActivate	MIOpenClick	
MIOpenClick	ReadTxt	InvString
MIViewCommonClick	Graphics	
MIViewSbetClick	ClearImg	Graphics
MIClearAllClick	ClearStrGr	ClearImg
CalculateAdsorption1Click	CalcAds_Des	
CalculateSbetClick	CalcSbet	
Graphics(KindF:string)	StGraphicG.Drow	

In the final Tab Sheets "Common" all calculated by the program porous texture characteristics are presented, i.e S_{BET}, $V_{0.95}$, $V_{DR,micro}$, V_{mezo} ($V_{0.95}$–$V_{DR,micro}$), $\Delta\Sigma V_p$, $\Delta\Sigma A_p$, $r^*_{p,i}$.

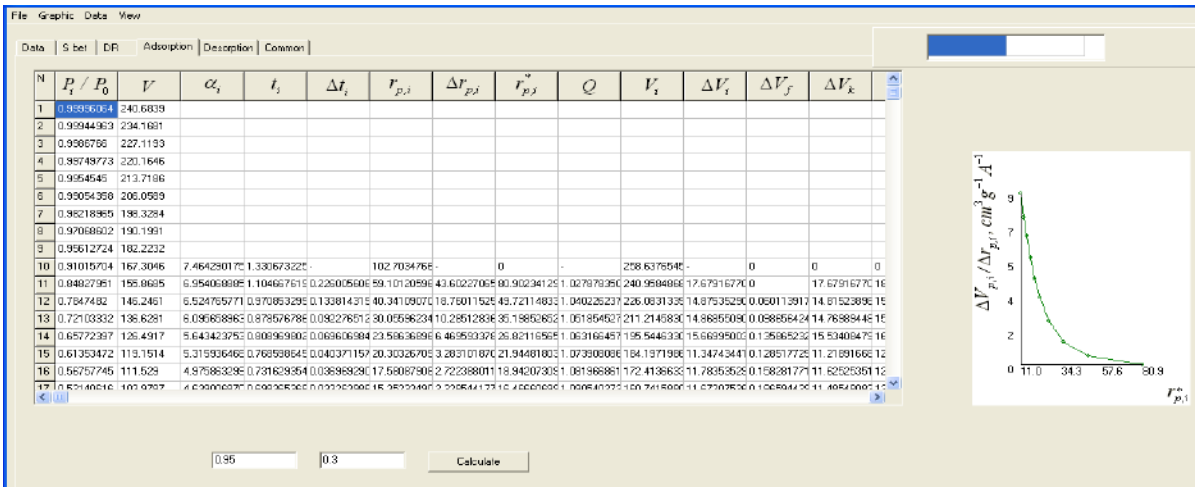

Fig. 4. An overview of the Tab Sheets for PSD calculations

REFERENCES

1. Gonsalvesh, L., et al., *Annual Assen Zlatarov University, Burgas*, XLIV (2015) p. 31.
2. Gonsalvesh, L., et al., *Indistrial Technologies* III (2016) p. 162.
3. Vlaev, L., Adsorption and Catalysis, Baltika-2002, Burgas, 2014.
4. Gonsalvesh, L., et al., *Annual Assen Zlatarov University, Burgas*, XLIV (2015) p. 26
.

ANNUAL OF ASSEN ZLATAROV UNIVERSITY, BURGAS
BULGARIA, 2017, v. XLVI (1)

OBTAINING WEAR-RESISTANT MATERIALS ON THE BASE OF METAL MATRIX COMPOSITES REINFORCED WITH TiC PARTICLES

Svetlana Boshnakova, Irena Markovska, Dimitar Rusev
E-mail: imarkovska@btu.bg

ABSTRACT

This study reviews the deposition of powder mixture of titanium carbide over stainless steel substrates for reinforcement in order to produce surface metal matrix composites (MMCs). They have been investigated intensively because of the composites great resistance to abrasive wear. Plasma melt injection (PMI) process was employed for layers of thickness 5-6 mm formed by two representative powders consisting volumetric fraction of TiC. The micromechanical characteristics are investigated as well as: Vickers hardness, Young modulus and SAR number, and the structures with the interface zones observed. The samples were machined and grinded and their resistance to abrasion tested according to ASTM G75-01. As a result, it is shown that the MMCs exceed the wear resistance of the reference base stainless steel.

Key words: *MMCs, TiC, wear resistance, Vickers hardness, structure*

INTRODUCTION

The aim of the present work is to synthesize a new material or such with improved properties based on a metal matrix reinforced with TiC particles. Metal matrix composites (MMCs) are characterized with the presence of hardening and clearly defined interface zones. The main objective of the present study is to obtain a metal matrix composite material characterized by increased strength and high wear resistance. Another task is to investigate the mechanism of formation of stable multiphase systems as well as to offer technology for directed production of composites with predefined properties.

In order to achieve the above-mentioned tasks systematic investigations have been carried out connected with the processes of application of different types of carbides on the surface of the metal substrate. Various technologies are used for this purpose, such as:

1. Laser Melt Injection with dusting in the melting zone
2. Plasma welding by feeding additional powder material using Plasma-Pulver / Plasma Melt Injection.

Carbides are compounds between metal and carbon and most commonly they have the formula MeC [1].

These compounds have some of the highest melting temperatures, e.g. SiC - 2700^{o}C; TiC–3140^{o}C; ZrC – 3530^{o}C; TaC – 3880^{o}C; VC – 2830^{o}C; WC – 2600^{o}C.

In this study, TiC has been chosen for synthesizing the metal matrix composites. Titanium carbide is appropriate as a reinforcing component in composite materials due to its stability, hardness and wear resistance.

A potentially profitable application is local reinforcement on stainless steels with TiC particles which produce a steel surface with improved wear-resistance characteristics [2].

MATERIALS AND METHODS

Materials

In the present study the main types of stainless steels, namely ferrite X2CrTi12, according to BDS EN 10088-4: 2009 [3], austenitic X5CrNi18-10, as well as its ASTM analog 304 [4] X15CrNi25-20 and X6CrNiTi18-10, have been investigated as possible metal matrices. There microstructure is composed of δ-Fe phases and γ-Fe phases. Laser welding and industrial welding are suitable for stainless steel 304 and X1NiCrMoCuN20-18-7. The methods used to apply TiC as an enhancing component require the addition of various metallic powder blends as binder component. Specifically, we have chosen the TRIBALOY® T-800 alloy. The TRIBALOY® T-800 alloy is in powder form. It

was selected because of its high wear resistance, which is further enhanced by the use of carbide materials.

Methods

The raw materials and MMCs were studied mainly by X-ray analysis, infrared (IR) spectroscopy, differential thermal analysis (DTA), scanning electron microscopy (SEM) etc.

Thermal analyzes were carried out on a complex apparatus for thermal analysis (STA 449 F3 Jupiter), NETZSCH - Germany, under heating up to 1000 ^{o}C at a speed of raising the temperature 10 ^{0}C/min.

Infrared spectroscopy FT-IR - spectra were made with Tensor 27 Fourier infrared spectrophotometer FTIR (Bruker, Germany) in the range of 400-4000 cm^{-1}. Measurements were carried out at room temperature, samples (0,3 mg) was tabletted with KBr (100 mg) at a pressure of 2-4 atm.

Measurement of structure – micro and macro structure - the study of microstructure is viewed by microscope Axiovert 200MAT and Axiovision camera for recording. Metallographic samples were etched by a mixture of 10 ml HNO_3, 20 ml of HCl and 30 ml H_2O. The samples were held in the solution for 15 min and then polished.

Measurement of hardness - the study of the mechanical properties of materials in the range of a few micrometers were performed according to EN ISO 6507-1 with UMT-2M (Bruker-Cetr, USA), working with load of 2 N and allowing measurement with maximum sensitivity of samples with dimensions in the millimetre range area.

Resistance to abrasion measurement - SAR measured with Miller tester according to ASTM G75-01 for the abrasive response of the WC composite which gives the relevant values for the approved properties compared to the general stainless steel characteristics in abrasive conditions.

Roughness measurement - according surface quality requirements as per EN 25178-70:2014 performed by Hommel Etamic "T8000".

EXPERIMENT

In Plasma Injection, the raw material (the powder mixture) must flow into the plasma stream to mix with the plasma jet. The raw material should be mixed with the plasma to molecular level.

A turbulent flow of homogeneously mixed plasma and particles goes on the metal support [5-7]. The experiment was carried out in Plasmastar Source 250 apparatus. This apparatus provides a local melting of the substrate.

The second method used in this study, the Laser Powder Injection, has the following specific advantages: process flexibility (wide range of controllable parameters), excellent adhesion to the substrate, low porosity of the coating, the laser beam acting only locally on the desired area, the composite can be formed with an arbitrarily chosen direction of application, carried out in a protective gas environment (protection from environmental influences). There is a relatively little thermal deposition onto the application area. This method allows to locally deposit a surface coating so that the width of a linear zone is in the range of 1.5-3 mm.

These advantages make it possible to apply the protective coating precisely to the desired area which is subjected to severe wear [8, 9].

RESULTS AND DISCUSSION

Different kinds of tests were used to characterize the coatings prepared. In order to obtain a qualitatively composite coating, homogeneous mixing of Tribaloy® T-800 particles with TiC is required. The morphology of the resulting powder blends was characterized by FT-IR and DTA. Figure 1 shows the infrared spectrum of the initial powder (powder mixture of Tribaloy T-800 and TiC). The results of the thermal analysis are shown in Fig. 2.

The preparation of powder mixtures has a determining effect on the morphology of the layers applied onto stainless substrates.

Figure 1 shows the FT-IR spectra of powder mixture of Tribaloy T-800 and TiC. The bands of the major groups in them are shown as follows: at 3431.82 cm^{-1}, 2921.05 cm^{-1}, 2852.37 cm^{-1}, 1631.53 cm^{-1}, 1164.85 cm^{-1}, 1088.69 cm^{-1}, 797.98 cm^{-1}, 780.89 cm^{-1}, 695.25 cm^{-1}, 591.72 cm^{-1}, 516.38 cm^{-1} and 458.53 cm^{-1}. Figure 1 shows that at 3441.62 / 3432.02 cm^{-1} a broad band is observed which corresponds to the O-H

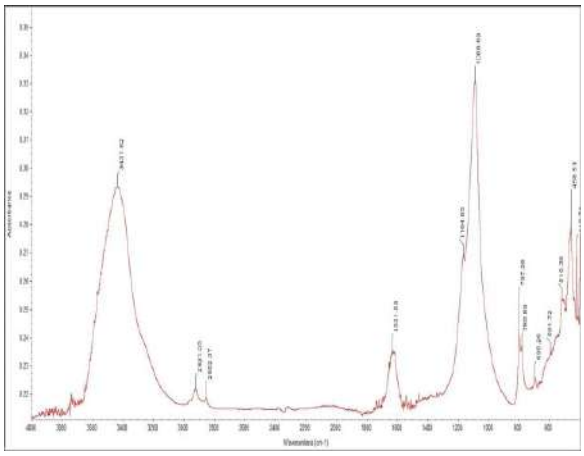

Fig. 1. FT-IR of Tribaloy T-800 and TiC

hydrogen bonding groups. The presence of water is confirmed by the strong deformation of the O-H bond at 1633.99 cm^{-1}, which is attributed to the deformation variations of O-H in H_2O. These asymmetric valent vibrations for the -OH groups and symmetric valent vibrations for the H-O-H groups are an indication of the humidity of the original powder mixtures. In Figure 1 the Ti-O-C bonds at 516.72 cm^{-1} and Ti-C at 797.98 cm^{-1} were visible, while an expected Ti-Co vibration spectrum of 360 cm^{-1} is not visible. It is also expected to show the spectrum of deposited TiC in the 230-250 cm^{-1} range. The multiple high peaks in the range of 1088 cm-1 are due to O-Si-O bonds.

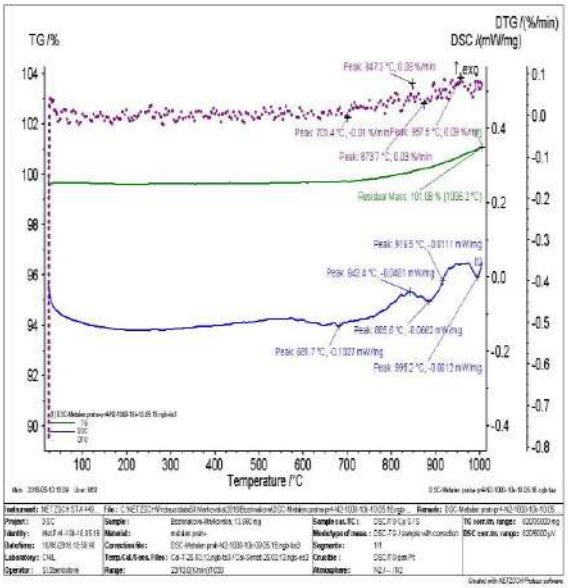

Fig. 2. DSC of initial mixture of Tribaloy T-800 and TiC

Figure 2 shows the thermal analysis results. The above-mentioned analyses of raw materials were carried out in order to investigate the processes that occur in them under heating. The thermal method shows the various steps in weight loss due to dehydration and oxidation reactions (due to burning of carbon compounds).

Experimental results show that the presence of a binding layer between the beads of the solid phase improves the mechanical strength of the materials. The metal which is the bonding layer is modified by the solidification and this process increases the strength of the metal matrix composite. Additionally, the resulting dense bonding phase prevents the appearance of microcracks in it as well as the passage of microcracks through the hardly melting TiC beads. In this way the mechanical strength of MMCs visibly increases.

Figure 3 shows a TiC layer deposited on a steel X5CrNi18-10 substrates.

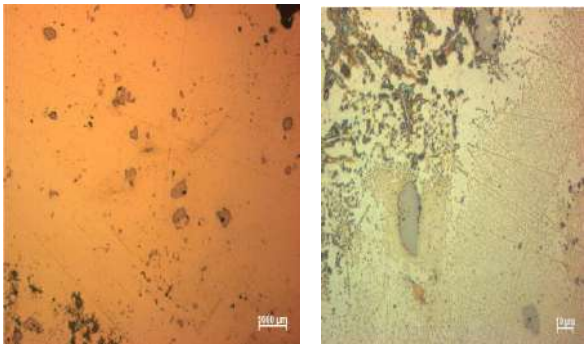

Fig. 3. TiC layer applied on X5CrNi18-10

Some of important physicomechanical properties of the synthesized materials, such as hardness, Young modulus, and wear resistance are measured. The hardness and elastic modulus values in both samples show a large scatter in some tests, due to the non-homogeneity of the surface and its high roughness. Nevertheless, there is a comparative repeatability of most of the values. This fact indicates that their corresponding micro-indents have fallen into an area of the same material. If the most repetitive values are subtracted and grouped, these three groups would have to correspond to the hardness and the modulus of elasticity of the parent metal and the interface zone (Figure 4).

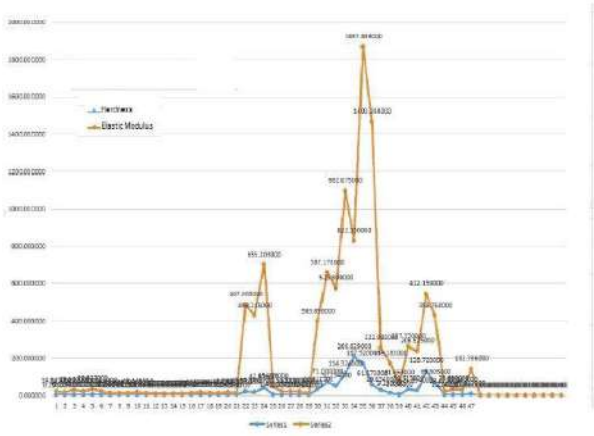

Fig. 4. Hardness and Young modulus distribution

The abrasion wear analysis was performed in accordance with ASTM G75-01, defining SAR numbers (abrasion resistance in slurry). All experiments were carried out in a medium of distilled water and solid particles of alumina powder with a size of 0.045-0.075 mm (99.7% Al_2O_3, 0.2% Na_2O, 0.02% Fe_2O_3, 0.02% SiO_2). The samples were subjected to controlled wear by simulating an oscillating motion. This determines the resistance of the test sample material. Two types of samples were compared. Two specimens of steel support X5CrNi18-10 coatings with TlC were compared to uncoated steel to determine cumulative mass loss and wear.

Pictures of the original patterns subjected to wear are shown in Fig. 5. (Samples No.22 and 23), while Fig. 6 shows pictures of the samples after the wear tests.

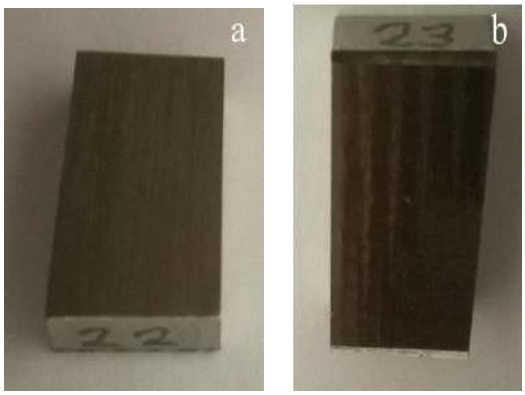

Fig. 5. Surface of the material before the test

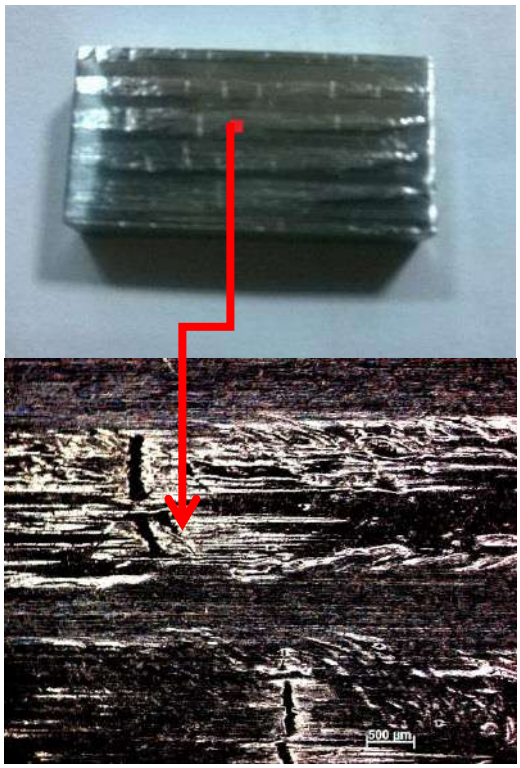

Fig. 6. Surface of the material after the test

In order to assess the impact of the abrasive material after the Miller test, the roughness of the surface was investigated. Initially, a hand-held measurement was performed by Mitotoyo apparatus, which is shown in Figure 7

Fig. 7. Investigation of material roughness with Mitotoyo's hand tool

Figure 8 shows a three-dimensional view of the worn out surfaces.

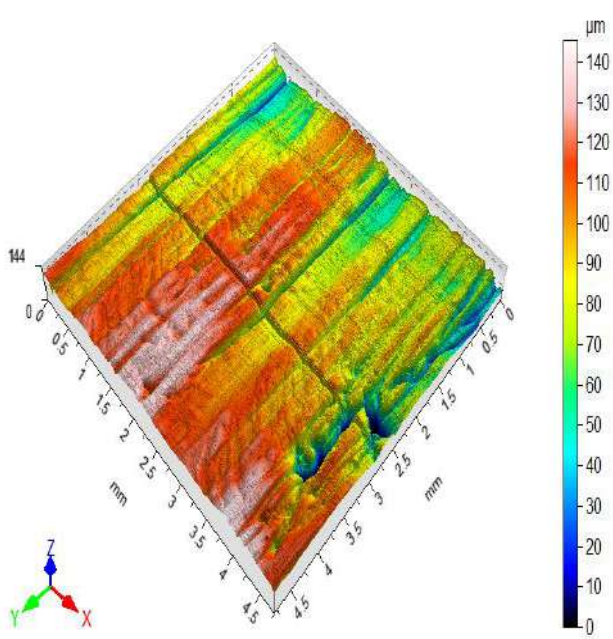

Fig. 8. Surface profile of MMCs

The figure shows strips of deformation due to the influence of the solid particles of Al2O3 on the surface of the samples. They also show hardening carbide zones, which are more resistant to wear. That's why the typical ulcers can be seen in the above figure.

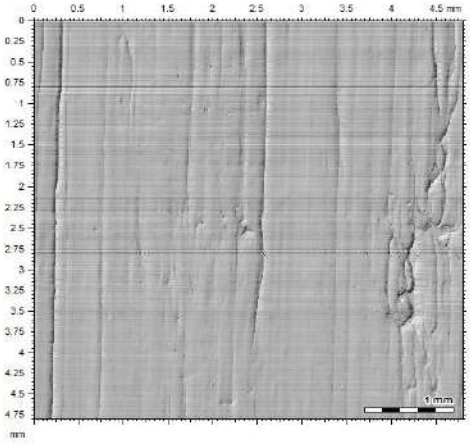

Fig. 9. Raster image of characteristic worn areas of Tribaloi T-800 + TiC

The statistical data have been summarized and then presented in Fig. 10.

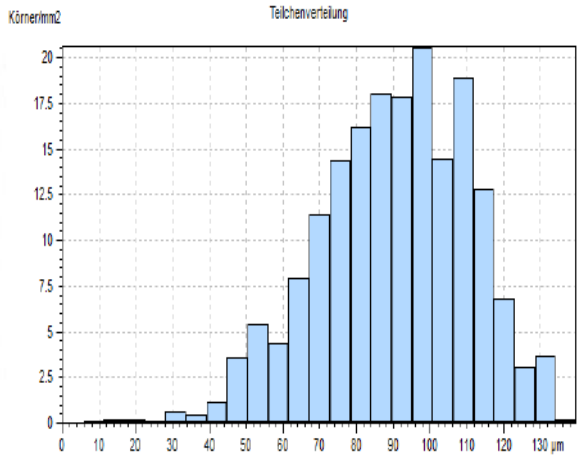

Fig. 10. Static distribution of the measured morphological characteristics

CONCLUSIONS

1. Suitable compositions of mixture of carbides and Tribaloy® T-800 powders for preparing of uniform deposition are established.
2. The technological parameters of coating regimes forming metal matrix composites (MMCs) were determined experimentally in accordance with the technological possibilities of the Plasma Reis installation and the Rofin laser installation in the department of Maschinenbau, TU Chemnitz, Germany.
3. The influence of the basic technological parameters in the plasma and laser deposition of the composite coatings on their structure, composition and mechanical properties was determined.
4. Around the TiC particles the uniform distribution of the solidified Tribaloy® T-800 alloy has been shown. This is a solid solution of fcc cobalt (α-Co) and dendritic formations, so-called intermetallic Laves phase consisting of Co_3Mo_2Si and Co_2MoCr.
5. It was found out that composite materials with ≈ 20% titanium carbides and Tribaloy® T-800 obtained at parameters 2.1 kW and a dust / gas flow rate of 4 l/min have wear resistance which is higher than the stainless steel base material.

REFERENCES

1. Gerasimov, E and S. Bachvarov, *Technology of Ceramic Materials, Sofia: Saraswati, 2003.*
2. Sacks, N., *The wear and corrosive-wear response of tungsten carbide-cobalt hardmetals under woodcutting and three body abrasion con-*

ditions, University of Erlangen-Nurnberg, Erlangen, 2002.
3. Boshnakova, S., D. Rusev and I. Markovska, *Proceedings of the University of Ruse "Angel Kanchev",* **52,** (2013), p. 246.
4. Yan, J., M. Gao and X. Zeng, *Optics and Lasers in Engineering,* **48,** (2010), p. 512.
5. Maslennikova, G., R. Mamaladze and S. Mizuta, *Ceramic materials, Moscow: Stroyizdat, 1984.*
6. G. Visokov, *Applied Plasma Chemistry, Sofia: Technika, 1987, vol. 1 and 2.*
7.Valkov, V., S. Bachvarov and H. Boyadjieva, *Construction*, **12,** (1990), p. 19.
8. Boshnakova S., D. Rusev and I. Markovska, *Journal of Chemical Technology and Metallurgy,* **50,** (2015), p. 557.
9. Boshnakova S., I. Markovska and D. Rusev, *Proceedings of the University of Ruse "Angel Kanchev",* **54,** (2015) p. 12.

ANNUAL OF ASSEN ZLATAROV UNIVERSITY, BURGAS
BULGARIA, 2017, v. XLVI (1)

STUDY ON THE POSSIBILITY TO UTILIZE ASHES FROM THERMAL POWER STATIONS FOR THE PRODUCTION OF CONSTRUCTION CERAMIC MATERIALS

Ganka Kolchakova, Nikolay Enev, Snejana Koruderlieva, Milena Ivanova
E-mail: gkolchakova@gmail.com

ABSTRACT

Many industrial production facilities form significant amounts of side products many of which remain practically unused after the main technological process and are dumped as industrial waste. Ashes from a thermal power station, clay and coal were used as raw materials for production of bricks. The samples of all prepared blends conform to the requirements of BDS EN ISO 10545 and can be used for production of construction ceramic articles. The development of particular engineering decisions for ecologically friendly management of the wastes from the mineral processing industry and their practical implementation is an important step towards resource effectiveness.

Key words: *waste, ash, ceramic materials, properties*

INTRODUCTION

The shortage of traditional raw materials on the one hand and the modern tendencies for implementation of non-waste technologies, on the other, have boosted the development and introduction of new materials obtained from local raw materials and industrial wastes for production of construction ceramic materials.

Certain experience in the field of production of bricks from ashes has been accumulated already in Spain, France, Germany, Poland, Russia, etc. [1-2]. Methods for manufacturing construction ceramic materials on the basis of combustion wastes [3], drilling slime, volatile sols, slag and sawdust [4-5], wastes from galvanic production lines, lime containing and abrasive wastes [6], contaminated mineral sediments [7] are applied without making changes in the production facilities and obtaining products of similar quality.

In this respect, the aim of the present work is to study the possibility to utilize ashes from thermal power stations for production of construction ceramic articles. Taking into account the severe ecological risks, the utilization of the ashes solves the problem of their storage on arable land.

EXPERIMENT

The raw materials used for the experiments were ashes from a thermal power station, clay and brown coal. Their chemical compositions are presented in Table 1.

The clay used was from the "Buchvata" deposit near Pleven. It has been categorized as medium plastic, easy melting and with medium cohesion.

Table 1. Chemical compositions of raw materials, mass%

Raw materials	Ash	Clay	Coal
SiO_2	48,32	63,44	22,00
Al_2O_3	17,90	15,25	10,48
Fe_2O_3	18,01	4,81	3,68
CaO	4,52	5,63	1,88
MgO	2,34	1,46	0,80
$K_2O + Na_2O$	2,40	1,76	-
TiO_2	0,87	-	-
MnO	0,04	-	-
SO_3	-	-	1,16
Loss of ignition	5,60	7,65	60,00

The coal used was clay-coal mixture of brown coal of class 0-40 mm. It has calorific value 2700 – 3700 Kcal/kg and content of ashes - 40%.

Figure 1 shows the diffractogram of the ash. The most intense reflexes observed for the ashes were for quartz, magnetite, albite and amorphous phase. The clay has the following phase composition: quartz – 30%, muscovite type mica and illite – 18%, halloysite – 14%, albite – 14%, montmorillonite – 12% and microcline – 10%.

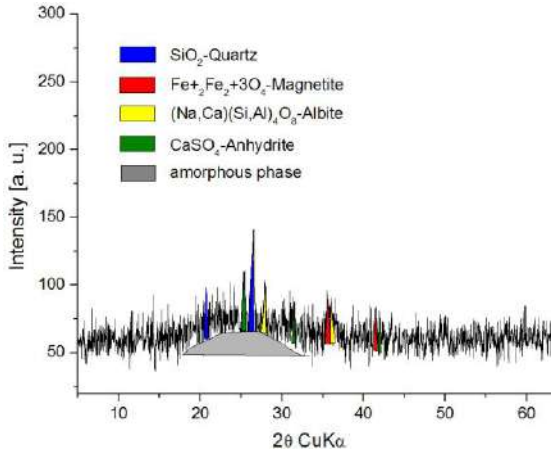

Fig. 1. Diffractogram of ash

Four sample blends with constant coal content were prepared for the experiments. The compositions of the blends are shown in Table 2.

Table 2. Compositions of the blends, mass%

Compositions	Ash	Clay	Coal
AC_LC_1	60	20	20
AC_LC_2	50	30	20
AC_LC_3	40	40	20
AC_LC_4	30	50	20

Based on the blend compositions, their chemical compositions were calculated and presented in Table 3.

Table 3. Chemical compositions of the blend, mass%

Compositions	AC_LC_1	AC_LC_2	AC_LC_3	AC_LC_4
SiO_2	46,08	47,59	49,10	50,62
Al_2O_3	15,89	15,62	15,35	15,09
Fe_2O_3	12,51	11,19	9,87	8,54
CaO	4,21	4,32	4,44	4,55
MgO	1,86	1,77	1,68	1,59
$Na_2O + K_2O$	1,79	1,73	1,66	1,60
TiO_2	0,52	0,44	0,35	0,26
MnO	0,02	0,02	0,02	0,01
SO_3	0,23	0,23	0,23	0,23
Loss of ignition	16,89	17,09	17,30	17,51

The sample blends were mixed and homogenized by combined milling in a ball mill for 3h, plasticized with 8% distilled water. After granulation through a 0.5mm sieve, samples were prepared from the blends by the method of semidry pressing under pressure of 50MPa.

The samples were sintered in superkanthal furnace NABER equipped with program regulator EUROTERM 822 to control the sintering process. The sintering was carried out at temperatures in the interval 900 -1050ºC at heating rate of 5ºC/min and isothermal period at the highest temperature 3h.

RESULTS AND DISCUSSION

Blends AC_LC_1 – AC_LC_4 had the same coal content of 20 mass%. The content of ashes was from 60 to 30 mass%, while clay content was from 20 to 50 mass%. The samples were characterized with respect to water uptake, apparent density and apparent porosity. The results obtained are shown in Table 4.

Table 4. Physicochemical properties of the samples

Compositions	T, °C	$\rho_{app.}\cdot10^{-3}$, g/m^3	W, %	$P_{app.}$, %
AC_LC_1	900	1,53	34,80	52,20
	950	1,52	33,10	50,31
	1000	1,54	31,70	48,82
	1050	1,56	30,11	46,97
AC_LC_2	900	1,48	36,30	53,72
	950	1,50	34,44	51,60
	1000	1,52	33,21	50,48
	1050	1,54	31,52	48,54
AC_LC_3	900	1,46	37,81	55,20
	950	1,48	36,10	53,43
	1000	1,50	34,60	51,90
	1050	1,52	34,10	50,31
AC_LC_4	900	1,44	39,21	56,46
	950	1,46	37,41	54,62
	1000	1,48	36,11	53,44
	1050	1,50	34,41	51,62

For all the samples studied, the apparent density increased with the increase of temperature. Besides, the apparent density decreased with the decrease of the content of ashes. A tendency of increase of the water uptake to 39% at temperature of 900°C and the apparent density to 54% was observed for blend AC_LC_4. These results can be explained by the fact that coal also takes part in the combustion process, so large amounts of gas phase is released which affects the porosity and density of the samples despite that the contents of alkali oxides increased almost twice.

The diffractograms of samples prepared from blends AC_LC_2 and AC_LC_4 are presented in Figures 2 and 3.

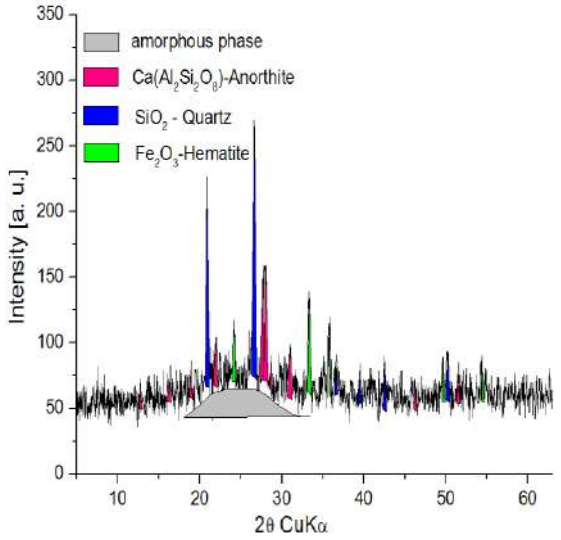

Fig. 2. Diffractogram of sample of blend AC_LC_2

For both blends, the characteristic reflexes from anorthite, quartz, hematite and amorphous phase were registered. For the AC_LC_4 blend, the content of amorphous phase sharply decreased with the decrease of the content of ashes.

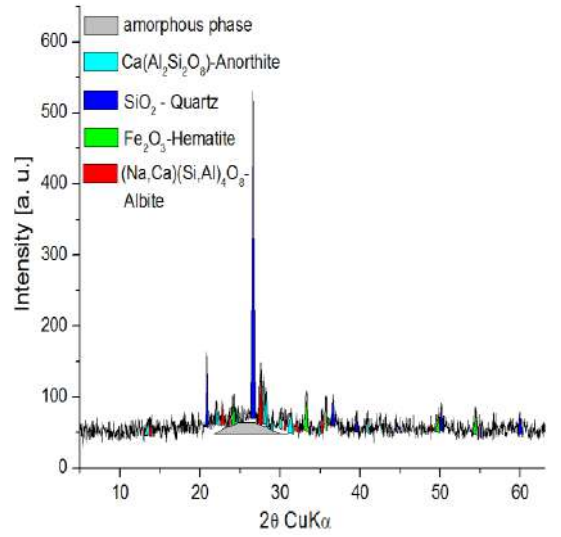

Fig. 3. Diffractogram of sample of blendAC_LC_4

A new crystalline phase was registered – albite, while the contents of anorthite and hematite decreased.

Table 5 shows the mechanical strength of the samples sintered in the temperature 1050ºC.

With the increase of amount of ashes, respectively, the increase of the apparent density, the mechanical strength of the sample increased.

Table 5. Mechanical strength of samples

Compositions	Compressive strength, MPa	Bending strength, MPa
AC_LC_1	23	3,0
AC_LC_2	21	2,7
AC_LC_3	18	2,4
AC_LC_4	17	2,3

The values of the mechanical strength of the samples obtained correlate with the values of the apparent density. For the composition having an ash content of 60 mass% (AC_LC_1), the compressive strength is 23MPa, while the bending strength is 3,0MPa.

The samples conformed to BDS EN ISO 10545 with respect to compression strength and bending strength.

CONCLUSIONS

According to BDS EN ISO 10545 "Ceramic tiles", the physicochemical properties of general purpose bricks should conform to the following requirements: water uptake not less than 10%; cold resistance – not less than 15 cycles; compression strength not less than 6MPa; bending strength not less than 1.4MPa. Comparing the results obtained for the samples studied to the requirements of national standard, it can be seen that the samples sintered from all the blends conform to the requirements of BDS EN ISO 10545 with respect to water uptake and mechanical strength.

REFERENCES

1. Ahmaruzzaman M., *Prog. Energy Combust. Sci.*, **36**, (2010), p. 327.
2. Sesé F. M., D. E. Quesada, F. A. Iglesias, *Ceram. Int.*, **37**, (2011), p. 3019.
3. Wang H., M. Zhu, Y. Sun, R. Ji, L. Liu, X. Wang, *Constr. Build. Mater.*, 155, (2017), p. 930.
4. Oreshkin D. V., A. N. Chebotaev, V. A. Perfilov, *Procedia Eng.*, **111**, (2015), p. 607.
7. Malhotra S.K., Tehri S.P., *Constr. Build. Mater.*, **10**, (1996), p. 191.
5. Kizinievic O., V. Kizinievic, *Constr. Build. Mater.*, **127**, (2016), p. 264.
6. Halil M.A, Turgut P., *Constr. Build. Mater.*, **22**, (2008), p. 1074.
7. Rauta S.P., R.V. Ralegaonkar, S.A. Mandavgane, *Constr. Build. Mater.*, **25**, (2011), p. 4037.

ANNUAL OF ASSEN ZLATAROV UNIVERSITY, BURGAS
BULGARIA, 2017, v. XLVI (1)

ENHANCEMENT OF IMMUNOASSAY FLUORESCENCE AND DETECTION SENSITIVITY TO NEUTROPHILS BY USING ANTIBODIES MULTIPLE LABELLED WITH DYE/DNA CONJUGATE

Zlatina Becheva, Katya Gabrovska, Yavor Ivanov
E-mail: zlatinabe4eva@abv.bg

ABSTRACT

A simple method of attaching multiple fluorescent labels on an antibody with a dye/DNA conjugate to increase the immunoassay sensitivity was suggested. In the work, bovine neutrophil fragments adsorbed on the surface of a 96-well plate were detected by its immunoreaction with a biotinylated anti-bovine neutrophil antibody. A 30 base pair double-stranded oligonucleotide terminated with biotin was attached to the antibody through the biotin/streptavidin/biotin interaction. Multiple labeling of the antibody was achieved after a fluorescent DNA probe was added into the solution and bound to the oligonucleotide. By comparison with fluorescein-labelled streptavidin, the assay with the dye/DNA label produced up to 2-fold increase in fluorescence intensity, and consequently about 7-fold lower detection limit. The multiple labelling method uses readily available reagents, and is simple to implement.

Key words: *fluorescence immunoassay, antibody labelling, multiple labels, Dye/DNA conjugate, neutrophils*

INTRODUCTION

Immunoassay methods have been widely used in many important areas, such as drug discovery, diagnosis of diseases, therapeutic drug monitoring and environmental monitoring due to their high specificity, simplicity, and versatility. The acquirement of detection signal usually entails labelling of antibodies or antigens with specific types of signal molecules or groups, such as radioisotopes, enzymes, metal complexes, and fluorescent dyes [1–3].

The fluorescent labels for the labelling of antibodies, which provide exquisite sensitivity [4] and guarantee the reliability of quantitative determination, should be bright and stable enough in single-molecule fluorescence detection. Usually, a fluorescent dye molecule is coupled to the target molecules to generate a detectable signal. However, the major difficulty limits the sensitivity: when these fluorophores are used, it results in relatively low fluorescence signal intensity. Because one antibody can only be labelled with one or a few fluorophores, the fluorescence signal is too weak to be detected when the target concentration is low. However, the sensitivity of the current fluorescence immunoassay technology needs to be improved substantially.

Immuno-PCR has been reported to improve the immunoassay sensitivity by 100- to 10 000-ffold [5], but requires a separate set of assay for DNA quantification. While chemiluminescence has been proven to be a very sensitive detection method, it is very difficult to implement the method on microarrays, since the light-emitting species are not confined to the surface [6].

An alternative approach for signal amplification in fluorescence immunoassay is to increase the number of labels conjugated to each antibody. This can be done by either attaching multiple labels at multiple sites of the antibody with only one label at each site or attaching multiple labels at one site with a macromolecular carrier.

Qin Zhang and Liang-Hong Guo [7] reported a simple method of attaching multiple fluorescent labels on an antibody with a dye/DNA conjugate to increase the immunoassay sensitivity. In this work, mouse IgG adsorbed on the surface of a 96-well plate was detected by its immunoreaction with biotinylated goat anti-mouse antibody. Multiple labeling of the antibody was achieved with SYBR Green I fluorescent DNA binder. In another work [8] these authors demon-

strated the utility of the dye/DNA conjugate label in both direct and competitive fluorescence immunoassays for the detection of 17β-estradiol. But this method is not applied to neutrophil cell detection in mastitic milk. It is known that subclinical mastitis, which shows no visible signs of disease, causes the greatest financial losses to dairy farmers. Therefore early detection of subclinical mastitis is an important issue. Until now, there has been no developed and implemented analytical method to detect early-stage of mastitis.

We have suggested a method of attaching multiple fluorescent labels at a single site on antibodies. In the work described below, we employed a 30 base paired biotinylated double-stranded oligonucleotide as a carrier for the conjugation of multiple fluorescent dyes. It was attached to a biotin-modified anti-bovine neutrophil antibody through the high specificity and high-affinity biotin-streptavidin interaction. A highly fluorescent DNA probe, Yodam1, binds in situ to the oligonucleotide at high ratios by the specific binding interaction with DNA.

A comparison was made with fluorescein labeled streptavidin in the immunological detection of antibody on Bovine neutrophil fragments (Scheme 1). The dye/DNA conjugated labelled immunocomplex produced about 2 fold increase in the fluorescence intensity. The improved sensitivity would be very attractive for neutrophil cell detection in mastitic milk.

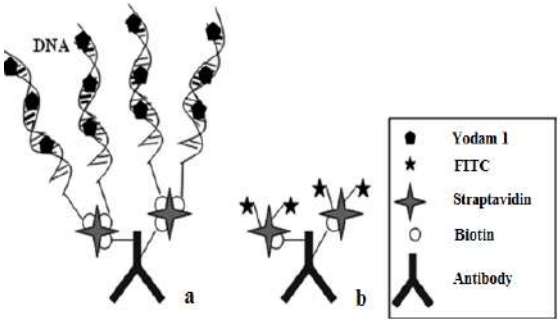

Scheme 1. (**a**) Schematic illustration of the antibody multiple labelling strategy using a biotinterminatedDNA to carry a large number of fluorescent DNA binders (Yodam 1), and streptavidin to link the DNA to a biotinylated antibody. (**b**) Schematic illustration of the conventional approach of using FITC-streptavidin to label an antibody.

MATERIALS AND METHODS

Reagents

Fluorescein 5(6) - isothiocyanate, Isomer I, and Yodam1 were provided from Fluka; Biotinyl-N-hydroxysuccinimide (BT-NHS), Streptavidin ST, Bovine serum albumin (BSA), Tween 20, and dimethylformamide (DMF) were purchased from Sigma-Aldrich, Germany; Sepadex G25 Medium was delivered by Pharmacia Fine Chemicals, Sweden. All other chemical reagents were pushed from Sigma-Aldrich.

Neutrophil fragment and anti-bovine neutrophil antibody obtaining

Bovine neutrophil fragments and anti-bovine neutrophil antibody were obtained as described in our previous paper [9].

Obtaining of anti-bovine neutrophil antibody-biotin conjugate

The antibody-biotin conjugate was prepared by the method of Zhang and Guo [7] with some modifications. Anti-bovine neutrophil antibody (Ab) was diluted in 100 mM carbonate buffer, pH 9.5. Biotin-NHS (BT) was diluted with dimethylformamide, just before use. The solutions were mixed dropwise. The final concentration ratio in the reaction mixture was 100 μg BT/1 mg Ab. The conjugating sample was incubated at room temperature for 3 hours in a shaker. The conjugate was purified by Sephadex G-25 Medium gel filtration column (300/10 mm). Flow rate was 0.5 mL/min. The elution buffer was 50 mM Tris, containing 50 mM NaCl, pH 8. Each fraction was measured for absorbance at 224 nm (for BT-NHS) and 280 nm (for protein) and UV-Vis spectrophotometric scan of the conjugate fraction was made on UV-Vis Spectrophotometer Jenway 6900.

Streptavidin-FITC conjugating procedure

Streptavidin-fluorescein isothiocyanate (ST-FITC) conjugation was performed by the method described in our previous paper (Becheva et al. 2017). Briefly, the reaction mixture contained 167 μg FITC/1 mg ST. The conjugate was purified by gel filtration with Sephadex G-25 Medium column (70/10 mm). Flow rate was 0.5 mL/min. The elution buffer was 50 mM Phosphate Buffer Saline (PBS), pH 7.4. Absorbance of each fraction was measured at 280 nm (for protein) and 495 nm (for FITC). The conjugate

fraction was analyzed by UV-Vis and fluorescence spectrophotometric assays (UV-Vis Spectrophotometer Jenway 6900 and Fluorescent Spectrophotometer F96Pro).

Protein concentration and moles fluorescent dye per mole protein (F/P) of the obtained conjugate were calculated with the following equations:

Protein concentration (M) = $(A_{280} - (A_{495} \times 0.3)) / \varepsilon_{protein}$

$F/P = A_{495} / (\varepsilon_{fluorescent\ dye} \times$ Protein concentration)

$\varepsilon_{protein}$ for streptavidin is 168 960 $M^{-1}cm^{-1}$

$\varepsilon_{fluorescent\ dye}$ for FITC is 68 000 $M^{-1}cm^{-1}$.

The optimal ratio of F/P is 2 – 5.

BT-DNA

A 30 base pair biotinylated double-stranded oligonucleotide (BT-DNA) was obtained by hybridizing two complementary single-stranded oligonucleotides purchased from Sigma-Aldrich (Germany): strand A, biotin-5'-TTT TTT TTT GCG GGT AAC GTC AAT ATT AAC TTT ACT CCC-3'; strand B, 5'-GGG AGT AAA GTT AAT ATT GAC GTT ACC CGC- 3'. The nine thymine nucleotides on strand A are designed to minimize possible spatial hindrance to binding with streptavidin.

The two oligonucleotides were mixed in 2 ×SSC buffer (0.3 M NaCl, 30 mM sodium citrate, pH 7.0), denatured at 95^0C for 5 min on a Gene Amp^R PCR System 9700, and then naturally cooled down to room temperature.

The concentration of the oligonucleotide was determined by absorbance at 260 nm.

ELISA with Ag-Ab-BT-ST-BT-DNA-Yodam1

ELISA procedures were performed by using a modified version of the methods of Zhang and Guo (2007).

Variety concentrations of neutrophil fragments (Ag) from 20 to 1000 μg/mL in 50 mM carbonate buffer, pH 9.6 (50 μL each) were added to microtiter plate wells. Incubation at 4°C, overnight was performed. The plate was washed three times with 200 μL washing buffer (50 mM Tris, 50 mM NaCl, 0.1% Tween 20, pH 7.4). Then, wells were blocked with 200 μL 50 mM PBS, containing 1% bovine serum albumin (BSA), pH 7.4, at 4°C, overnight. The washing procedure was performed as described above. After that, 50 μL of 300 μg/mL anti-bovine neutrophil antibody, conjugated with BT, were added and the samples were incubated at 37°C for 2 hours in a shaker. Then, they were washed again. ST solution (10 μg/mL in 50 mM Tris, 50 mM NaCl, pH 8) (50 μL) were added and were incubated at 37°C for 2 hours in a shaker. The samples were washed. BT-DNA 40 mM in 2 x SCC, pH 7, (50 μL) were added and the samples were incubated at 37°C for 1 hour in a shaker. Then, they were washed again. Finally, 200 μL of fluorescent dye Yodam1 0.5 μg/mL in 50 mM PBS, pH 7.4, were added and incubated at 37°C for 10 min.

The absorbance of the samples was measured on microplate reader Rayto RT-2100C (492 nm wavelength). The fluorescence intensity was measured on Perkin Elmer Spectrophotometer LS45 (excitation 476 nm, emission 511 nm, voltage 800 V).

ELISA with Ag-Ab-BT-ST-FITC

First steps of the assay were the same as described above (*ELISA with Ag-Ab-BT-ST-BT-DNA-Yodam1*). ST-FITC conjugate (10 μg/mL in 50 mM PBS, pH 7.4) (50 μL) were added in the wells after the anti-bovine neutrophil antibody-BT step. The samples were incubated at 37°C for 2 hours in a shaker.

The absorbance of the samples was measured on microplate reader Rayto RT-2100C (492 nm wavelength). The fluorescence intensity was measured on Perkin Elmer Spectrophotometer LS45 (excitation 495 nm, emission 518 nm, voltage 800 V).

RESULTS AND DISCUSSIONS

1. Proving of anti-bovine neutrophil antibody-biotin conjugate and purification

Anti-bovine neutrophil antibody – biotin conjugate was prepared to determinate the Bovine neutrophil fragments. The conjugating mixture is composed of antibody- biotin conjugate, free antibody and unconjugated Biotin. The mixture was filtrated with Sephadex G25 Medium for size-exclusion chromatography. The results of anti-bovine neutrophil antibody-BT filtration are shown on Figure 1. The obtained purified conjugate was in fraction number 6 and fraction number 7. They were mixed together. The successful conjugation was proved by 6900 UV/Vis Spectrophotometer JENWAY. UV-Vis spectrophotometric scan comparison was made (Figure 2).

The obtained conjugate had two peaks – the first at 222 nm and the second at 273 nm. The

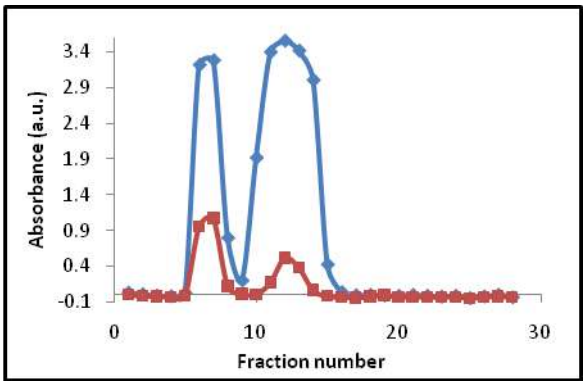

Fig. 1. Sephadex G-25gel filtration of anti-bovine neutrophil antibody-Biotin conjugate. Absorbance at 224 nm (♦) and 280 nm (■).

first one was a slightly shifted characteristic peak for biotin-NHS molecule (224 nm), and the second one was similar to uncoupled antibody peak (270 nm). This shift proves the antibody- Biotin coupling.

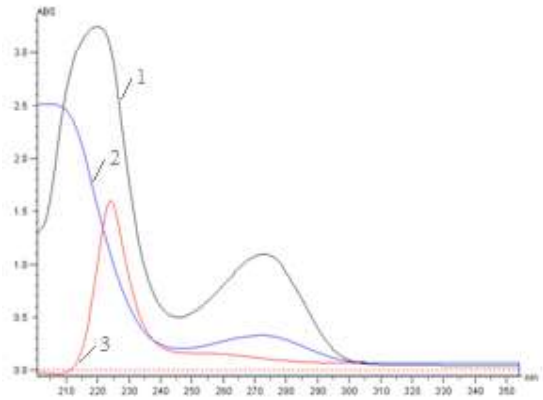

Fig. 2. UV-Vis spectrophotometric assay of the obtained anti-bovine neutrophil antibody-Biotin conjugate (1), uncoupled anti-bovine neutrophil antibody (2) and uncoupled Biotin-NHS (3).

2. Streptavidin-FITC conjugate purification and proving

The conjugating mixture has Streptavidin - fluorescent dye conjugate, free Streptavidin and unconjugated dye. The mixture was filtrated with Sephadex G25 Medium for size-exclusion chromatography. The conjugate has the highest molecular weight in the mixture and exits from the first column (fraction 3), (Fig. 3). The absorption of the fraction 3 was calculated with equations to prove the conjugation.

Fluorescent dye: protein ratio (F/P) is in optimal values (3–10).

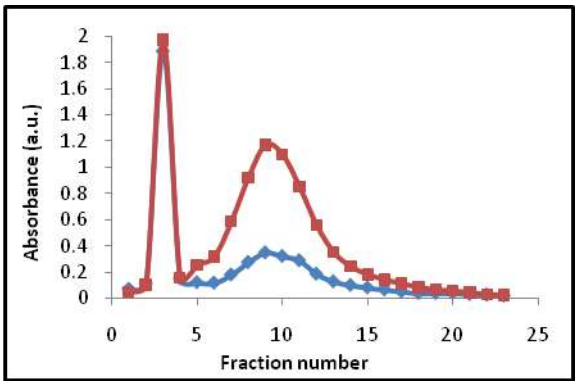

Fig. 3. Sephadex G-25gel filtration of a streptavidin-FITC conjugate. Absorbance at 280 nm (♦) and 495 nm (■).

Fraction 3 has 0.4 mg protein concentration and 3.8 F/P Scan of the fraction 3 with 6900 UV/Vis Spec trophotometer JENWAY was made to confirm the streptavidin –FITC coupling (Figure 3).

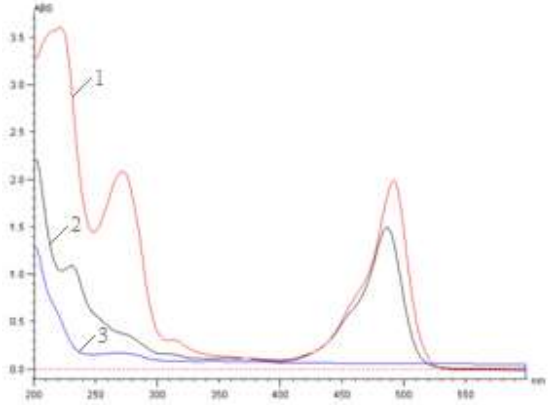

Fig. 4. UV-Vis spectrophotometric assay of the obtained streptavidin-FITC conjugate (1), uncoupled streptavidin (3) and uncoupled FITC (2).

The Streptavidin–FITC conjugate has two absorption maximums: the first at 275 nm and the second at 495nm.

The maximums absorbing wavelengths in conjugate spectrum, which are characteristic of protein and free FITC, were slightly shifted from 270 to 275 nm compared with free antibody and from 490 to 492 nm compare with free FITC (Fig. 4).

Figure 5 shows the fluorescence spectrophotometric analysis of the obtained conjugate and unbound FITC and was performed with Fluorescent Spectrophotometer F96Pro. The free FITC has a peak at 520 nm and *streptavidin* –FITC

conjugate has a peak at 525 nm. This shift proves the antibody-dye coupling.

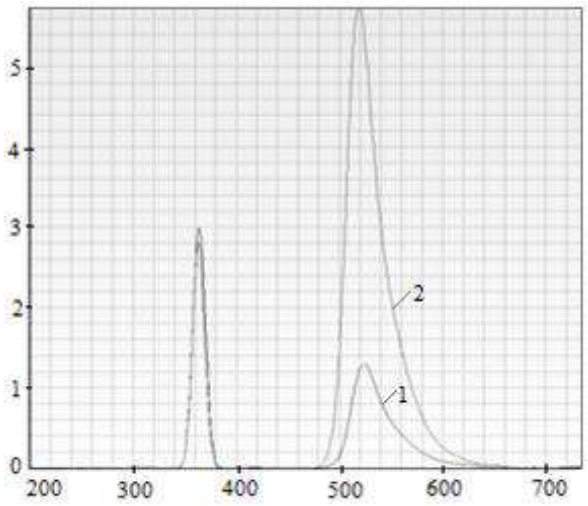

Fig. 5. Fluorescence spectrophotometric assay of the obtained streptavidin-FITC conjugate (1) and uncoupled FITC (2).

3. Calibration curves of fluorescence immunoassay for the detection of neutrophil fragments using the Yodam1/BT-DNA conjugate label and fluorescent molecular label.

In the system reported here, DNA structures serve as a template for assembling the intercalating dyes into fluorescent arrays. The biotinylated double-stranded oligonucleotide (BT-DNA) was obtained by hybridizing two complementary single-stranded oligonucleotides. The BT-DNA has a sequence with 9 thymine nucleotides at the biotin end acting as a spacer to reduce the steric hindrance between BT-DNA and the surface-confined Ag/BT-Ab/SA interaction. High densities of fluorophores are assembled in a very small region of base pairs in the DNA helix, yet the DNA template keeps them far enough away from each other to prevent self quenching. All the experimental data obtained above support our notion that the Yodam1/BT-DNA conjugate can be used effectively to attach multiple fluorescent labels in immunoassays. The assay protocol described in the Experimental Section was established after a series of optimization experiments were performed to determine the optimal concentration, reaction time, and temperature for neutrophil fragments/BT-Ab immunoreaction and biotin/streptavidin binding. The optimal conditions for the binding of BT-DNA/ Yodam1 conjugate to the surface-attachedAg/BT-Ab/SA immunocomplex were investigated as follows. The concentrations of the reagents for the formation of the immunocomplex were: neutrophil fragments (Ag) from 20 to 1000 μg/mL for plate coating, 300 μg/mL BT-Ab for immunoreaction, and 10 μg/mL SA for BT-Ab binding. BT-DNA 40 mM were then added to the plate. After binding of BT-DNA to SA on the surface, 200 μL of fluorescent dye Yodam1 0.5 μg/mL were added into the plate and the fluorescence intensity was measured.

After all the reaction parameters were optimized, a direct comparison was made between the dye label and the dye/DNA conjugate label format in the immunoassay for neutrophil fragments. The experiment is illustrated in Scheme 1. Neutrophil fragments coating and BT-Ab reaction were performed in the same way for (with) the two labelling formats, with the neutrophil fragments concentration varied from 20 to 1000 μg/mL. The results obtained in the comparison experiment are shown in Figure 6.

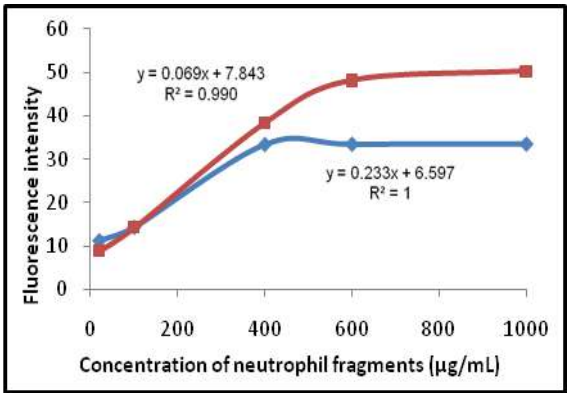

Fig. 6. Fluorescence immunoassay for the detection of Neutrophil fragments using the Yodam1/BT-DNA conjugate label (■) and FITC molecular label (♦). Each data point is the average of three replicate measurements.

Under the optimal conditions, the fluorescence intensity was proportional to the neutrophil fragments concentration. The typical fluorescence curves of Ag-Ab-BT-ST-BT-DNA-Yodam1 and Ag-Ab-BT-ST-FITC at different concentrations in the range from 20 to 1000 μg/mL are shown in Figure 6. Yodam1 was selected, because its fluorescence excitation and emission maximum wavelengths are close to that of fluorescein, to which the Yodam1/DNA conjugate is going to be compared. In both assays, the fluorescence signal is progressively higher with increasing neutrophil fragments concentra-

tion, suggesting that both methods can be used for quantitative detection of immunoassays.

However, in the whole range of the Ag concentration examined, the intensity of the Yodam1/DNA labelled assay is persistently higher than the dye-labelled assay. It was found that the linear range under optimal conditions is 100- 400 μg/mL with calculated limit of lower detection - 70 μg/mL neutrophil fragments for the dye-labeled assay and 20- 600 μg/mL with calculated limit of lower detection 10 μg/mL neutrophil fragments for the dye/DNA conjugate-labelled assay, respectively. Obviously, the dye/DNA multiple labelling strategy improved the detection sensitivity for neutrophil fragments.

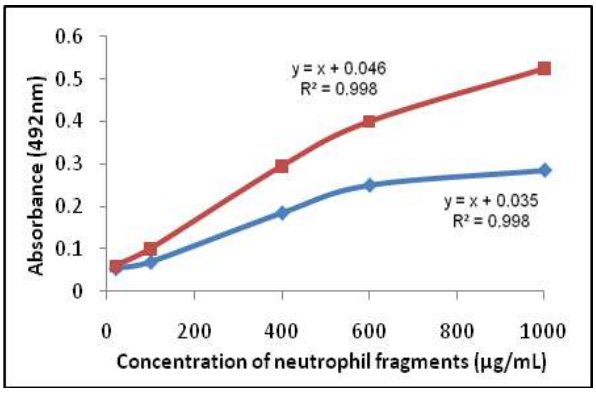

Fig. 7. ELISA test for the detection of Neutrophil fragments using the the Yodam1/BT-DNA conjugate label (■) and FITC molecular label (♦)

The sensitivity improvement of immunoassay by using Dye/DNA conjugate is confirmed also by the measured absorbance of the samples on microplate reader Rayto RT-2100C (492 nm wavelength). As illustrated in Figure 7, for both methods, absorbance is increased with increasing the neutrophil fragments concentration. The results show that the absorption values for the dye-labelled assay are lower than the absorption values for the dye/DNA conjugate-labelled assay.

REFERENCES

1. Berson, S. A. and R. S Yalow. Assay of plasma insulin in human subjects by immunological methods. *Nature*, 1959, 184, 1648–1649.

2. Li, T. M., and R. F. Parrish. Fluorescence and Immunodiagnostic Methods. In: *Topics in Fluorescence Spectroscopy. Volume 3*: *Biochemical Applications*. Lakowicz, J. R. (Ed.). Springer US, New York. 2002.p p 273–287.

3. Blackburn, G. F., H. P. Shah, J. H. Kenten, J. Leland, R. A. Kamin, J. Link, J. Peterman, M. J. Powell, A. Shah and D. B. Talley. Electrochemiluminescence detection for development of immunoassays and DNA probe assays for clinical diagnostics. *Clin. Chem.* 1991. 37, 1534–1539.

4. Hahn, M. A., J. S. Tabb, and Krauss, T. D. Detection of single bacterial pathogens with semiconductor quantum dots. *Anal. Chem.* 2005, 77, 4861–9.

5. Byassee, T. A., W. C. Chan, and Nie, S. Probing single molecules in single living cells. *Anal. Chem.* 2000, 72, 5606–5611.

6. Xu, X. H., and Yeung, E. S. Direct measurement of single-molecule diffusion and photodecomposition in free solution. *Science*. 1997, 275, 1106–1109.

7. Zhang Q. and L. Guo. Multiple Labeling of Antibodies with Dye/DNA Conjugate for Sensitivity Improvement in Fluorescence Immunoassay. *Bioconjugate Chem.*, 2007, 18, 1668-1672.

8. Zhang Q., Z. Shengchao, and L.Guo, Dye/DNA Conjugates as Multiple Labels for Antibodies in Sensitive Fluorescence Immunoassays, Sonny S. Mark (ed.), *Bioconjugation Protocols: Strategies and Methods*, Methods in Molecular Biology, vol. 751, Springer Science and Business Media, LLC 2011

9. Becheva Z., K. Gabrovska and T. Godjevargova. Immunofluorescence icroscope assay of neutrophils and somatic cells in bovine milk. *Food and Agricultural Immunology*, 2017.

ANNUAL OF ASSEN ZLATAROV UNIVERSITY, BURGAS
BULGARIA, 2017, v. XLVI (1)

CHEMICAL COMPOSITION, ANTIOXIDANT AND ANTIMICROBIAL ACTIVITIES OF DILL ESSENTIAL OILS (*Anethum graveolens L.*)

Milen Dimov, Krasimira Dobreva[1], Stanka Damyanova[2], Albena Stoyanova[3]
E-mail: midimow@abv.bg

[1]Trakia University, Faculty of Technics and Technologies, 38 Graf Ignatiev St, 8600 Yambol, Bulgaria
[2] University of Russe "Angel Kanchev", Razgrad Branch, 47 Aprilsko Vastanie Blvd. 7200 Razgrad, Bulgaria
[3]University of Food Technologies, Technological Faculty, 26 Maritza Blvd., 4003 Plovdiv, Bulgaria

ABSTRACT

The chemical composition of dill (Anethum graveolens L.) commercial essential oils was studied. Carvone (46.89%) and limonene (28.93%) were the dominant compounds in the dill seed oil. The major components in dill weed oil were carvone (27.81%), limonene (16.94%), α-phellandrene (15.87%) and p-cymene (14.18%). The antioxidant and antimicrobial activities of essential oils were also determined.

Key words: *dill, essential oils, chemical composition, antioxidant and antimicrobial activities*

INTRODUCTION

Dill oil is obtained from the dill plant (*Anethum graveolens* L.) family Apiaceae in two different forms:

Dill seed oil is obtained by steam distillation of the crushed ripe fruits of the dill plant. Its main components are limonene (up to 40%) and (+)-carvone (up to 60%). [5, 10, 11, 13, 15, 19, 20, 26, 28]**.**

Dill weed oil is obtained by steam distillation from dill weed (herb) before the fruits become mature. Its main components are α-phellandrene (10 – 20%), limonene (30 – 40%) and carvone (30 – 40%) [3, 5, 9, 10, 18, 20, 23, 29].

The oils demonstrate antimicrobial [4, 7, 8, 10, 14, 15, 17, 19, 24] and antioxidant [1, 2, 25, 26] properties and have been traditionally used for food products [3, 12].

The aim of the present study was to determine the chemical composition, antimicrobial and antioxidant activities of Bulgarian commercial essential oil from dill (*Anethum graveolens* L.).

EXPERIMENT

Samples of essential oils. Essential oils of dill were commercial Bulgarian samples.

The physical-chemical properties of the oils were measured according to Russian Pharmacopoeia [22].

Chemical composition of essential oils. Gas chromatography (GC) analysis was performed using gas chromatograph Agilent 7890A; column HP-5 ms (30 m x 250 μm x 0.25 μm); temperature: 40°C/3 min, 5°C/min to 300°C for 5 min, total 60 min; carrier gas helium 1mL/min constant speed; split ratio 30:1.

GC/MS analysis was carried out on a mass spectrometer Agilent 5975C, carrier gas helium, the column and temperature were the same as in the GC analysis.

The identification of the chemical compounds was made by comparison with their relative retention time and library data. The identified components were arranged in order of the retention time and their quantity was given in percentage.

Antioxidant activity determination

DPPH assay. The 1,1-diphenyl-2-picryl hydrazyl radical (DPPH) (Sigma) scavenging activity assay was performed according to the procedure described by Thaipong et al. [27] with some modifications by Marchev et al. [16].

ABTS assay. The procedure was previously described by Re et al. [21] and some modifications by Marchev et al. [16].

Ferric reducing antioxidant power (FRAP). FRAP assay was conducted by the modified method by Benzie and Strain [6] from Marchev et al [16].

Cupric reducing antioxidant capacity (CUPRAC). The method was adapted according to Apak et al. [1].

Oxygen radical antioxidant capacity (ORAC) assay. The lipophilic Oxygen Radical Absorbance Capacity (L-ORAC) assay measures by Marchev et al. [16].

Antimicrobial activity. Microorganisms which are frequent micro flora in cosmetic and food products were examined as test culture: Gram-positive bacteria *Staphylococcus aureus* ATCC 6538, *Kocuria rhizophila ATCC 9341 (Micrococcus luteus)* and *Bacillus subtilis ATCC 6633;* Gram-negative bacteria: *Escherichia coli* ATCC 8739, *Pseudomonas aeruginosa* and *Salmonella abony* NTCC 6017.

The microorganisms were received from the National Bank of Industrial Microorganisms and Cell Cultures, Sofia.

The antimicrobial activity of the oils was investigated by the method of diffusion in agar using pits with a diameter of 8 mm under standardized conditions [30]. Testing was done on Oxoid nutrient medium [Lab-Lemco Powder (Oxoid L 29) – 3.0 g, Peptone (Oxoid L 7) – 5.0 g] with 2% agar. 50 μl of the corresponding oils were dripped in the pits. After their cultivation at 37^{O}C for 24 h the diameters of the sterile zones were accountted in mm.

RESULTS AND DISCUSSION

Some of the physical and chemical characteristics of the oils are shown in Table 1. As can be seen, the values of the physical and chemical characteristics of the oils are almost equal with the literature data.

Table 1. Physical-chemical properties of oils.

Properties	Dill seed oil	Dill weed oil
Color	dark - yellow	pale - yellow
Specific gravity (d_{20}^{20})	0.9472	0.9039
Optical rotation (α_D)	55.00°	55.06°
Refractive index (n_D^{20})	1.3435	1.5135
Acid number (mg KOH/g oil)	15.7	1.2

The chemical composition of the essential oils is listed in Table 2.

Remarkable quantitative differences between both studied essential oil samples were detected.

Table 2. Chemical composition of the essential oils, %

№	components	RI	Dill seed oil	Dill weed oil
1.	α-Pinene	939	0.65	1.49
2.	β-Pinene	979	0.11	0.73
3.	β-Myrcene	991	0.09	0.55
4.	α-Phellandrene	998	nd*	15.87
5.	p-Cymene	1024	5.03	14.18
6.	Limonene	1030	28.94	16.94
7.	Terpinolene	1088	0.18	0.27
8.	β-Linalool	1092	0.15	0.41
9.	Dihydrocarvone	1179	4.22	5.78
10.	Dihydrocarveol	1192	3.10	3.68
11.	cis-Carveol	1202	0.25	2.07
12.	Carvone	1205	46.89	27.81
13.	Neodihydrocarveol	1208	0.65	0.88
14.	2,3-Pinanediol	1278	nd	0.22
	Identified, %		90.25	90.88

* not determined

As can be seen, 12 components representing 90.25% of the total content were identified in dill seed oil. Five of them were in concentrations over 1% and the rest 7 constituents were in concentrations under 1%. The major constituents (up to 3%) of the oil were as follows: carvone (46.89%), limonene (28.93%), p-cymene (5.03%), dihydrocarvone (4.22%) and dihydrocarveol (3.10%).

As can be seen, 14 components representing 90.88% of the total content were identified in dill weed oil. Eight of them were in concentrations over 1% and the rest 6 constituents were in concentrations under 1%. The major constituents (up to 3%) of the oil were as follows: carvone (27.81%), limonene (16.94%), α-phellandrene (15.87%), p-cymene (14.18%), dihydrocarvone (5.78%) and dihydrocarveol (3.68%).

The results of the chemical composition do not contradict the literature data.

The distribution of the major groups of aroma substances in the dill seed oil is shown in Fig. 1.

Oxygen monoterpenes (61.23%) were the dominant compounds in the dill seed oil, followed by monoterpene hydrocarbons (33.2%), phenylpropanoids (5.57%) and oxygen monoterpenes (31.04%).

The dominant compounds in the dill weed oil were oxygen monoterpenes (44.95%) and monoterpenes hydrocarbons (39.45%), followed by phenylpropanoids (15.60%).

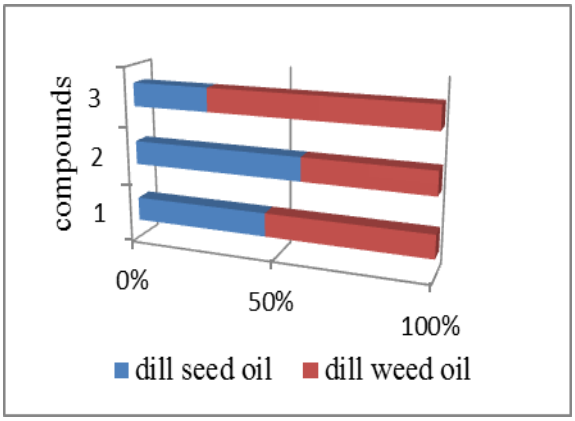

Fig. 1. Groups of components in dill essential oils: 1 – monoterpene hydrocarbons; 2 – oxygen monoterpenes; 3 – phenylpropanoids.

The results of the antioxidant activity are presented in Table 3.

Table 3. Antioxidant activity of dill essential oils.

Sample	DPPH	FRAP	CUPRAC
	µM Trolox Eq./ml oil	µM Trolox Eq./ml oil	µM Trolox Eq./ml oil
Dill seed oil	2578.2	7583.6	71696.6
Dill weed oil	683.0	1833.5	109958.4

As the results show, independently of the method used, both oils have antioxidant activity, more pronounced in the seed oil. The difference in activity is explained by the chemical composition, such as the content of monoterpene oxygen components, which is higher in the seed oil. The results for antioxidant activity do not contradict the literature data.

The results of antimicrobial testing are presented in Table 4. As can be seen, Gram positive bacteria *Staphylococcus aureus* and *Kocuria rhizophila* were sensitive to the dill seed oil (Fig. 2 and 4). *Bacillus subtilis* was slightly sensitive to the dill weed oil (Fig. 3).

Gram negative bacteria *Escherichia coli* and *Salmonella abony* were sensitive to the investigated oils (Fig. 5 and 7). *Pseudomonas aeruginosa* was slightly sensitive to the dill seed oil and insensitive to dill weed oil (Fig. 6).

Table 4. Antimicrobial activity of essential oils.

Test- microorganisms	Diameter of inhibition, mm			
	Dill seed oil		Dill weed oil	
	1*	2	3	4
Staphylococcus aureus ATCC 6538	23,5	22,4	16,3	20,4
Bacillus subtilis ATCC 6633	17,5	17,7	12,6	14,1
Kocuria rhizophila ATCC 9341	21,5	21,9	15,8	17,3
Escherichia coli ATCC 8739	13,6	13,3	13,3	15,2
Pseudomonas aeruginosa ATCC 9027	12,9	13,2	0	0
Salmonela abony NCTC 6017	13,4	16,1	11,6	12,6

* parallel samples

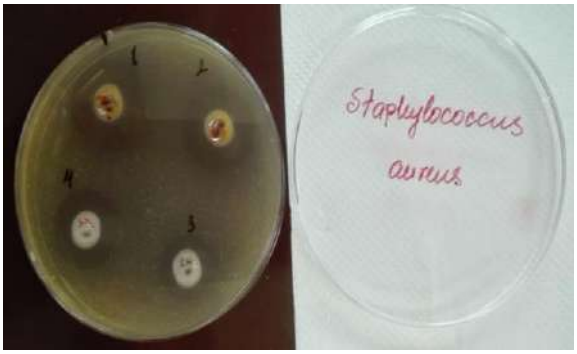

Fig. 2. Antimicrobial activity against *Staphylococcus aureus*.

Fig. 3. Antimicrobial activity against *Bacillus subtilis.*

Fig. 4. Antimicrobial activity against *Kocuria rhizophila.*

Fig. 5. Antimicrobial activity against *Pseudomonas aeruginosa.*

Fig. 6. Antimicrobial activity against *Escherichia coli.*

Fig. 7. Antimicrobial activity against *Salmonella aboy.*

CONCLUSION

The chemical composition, antioxidant and antimicrobial activity of commercial dill seed and weed oils are investigated.

ACNOWLEDGMENTS

The studies are conducted with the financial support of Trakia University under contract 5FTT/2016.

REFERENCES

1. Apak R., K. Guclu, M. Ozytirek, S. Karademir (2004). Novel total antioxidant capacity index for dietary polyphenols and vitamins C and E, using their cupric Ion reducing capability in the presence of neocuproione: CUPRAC method, J, Agric. Food. Chem, **52**, № 26, p. 7970.
2. Ayoughi F., M. Barzegar, M.A. Sahari, H. Naghdi Badi (2009) Antioxidant effect of dill (*Anethum graveolens* Boiss.) oil in crude soybean oil and comparison with chemical antioxidants**,** Journal of Medicinal Plants, **8**, № 30, p. 71.
3. Baeva M., T. Sapundzhieva, P. Merdzhanov, A. Pavlova, I. Alexieva, A. Stoyanova (2013). Investigation of some local Bulgarian culinary spices. 1. Dill (*Anethum graveolens* L.). Journal of Food and Packaging Science Technique and Technologies, **2**, p. 129.
4. Babri R., I. Khokhar, Z. Mahmood, S. Mahmud (2012). Chemical composition and insecticidal activity of the essential oil of *Anethum graveolens* L., Science International (Lahore), **24**, № 4, p. 453.
5. Bauer K., D. Garbe, H. Surburg (2001). Common fragrance and flavour materials. Preparation, properties and uses. IV Compl. Revised Edition. Wiley-VCH Verlag GmbH, Weinheim. Germany.
6. Benzie I., J. Strain (1996). The ferric reducing ability of plasma (FRAP) as a measure of "antioxidant power", The FRAP assay. Anal. Biochem, **239**, № 1, p. 70.
7. Delaquis P., K. Stanich B. Girard, G. Mazza (2002). Antimicrobial activity of individual and mixed fractions of dill, cilantro, coriander and eucalyptus essential oils, International Journal of Food Microbiology, **74**, №1/2, p.101.
8. Fatore M., R. Marwah, A. Onifade, J. Ochei, Y. Al Mahroqi (2006). ^{13}C NMR analysis and antifungal and insecticidal activities of Oman

dill herb oil, Pharmaceutical Biology, **44**, № 1, p. 44.
9. Huopalati R., R. Lahtinen, R. Hiltunen, I. Laakso (988). Studies on the essential oils of dill herb (*Anethum graveolens* L.) carbon-dioxide-extracted oil, Flavour and Fragrance Journal, **3**, 1988, №3, p. 121.
10. Jirovetz L., G. Buchbauer, A. Stoyanova, E. Georgiev, S. Damianova (2003). Composition, quality control, and antimicrobial activity of the essential oil of long-time stored dill (*Anethum graveolens* L.) seeds from Bulgaria, Food Chemistry, **51**, № 13, p. 3854.
11. Jirovetz L., G. Buchbauer, A. Stoyanova, Z. Denkova, I. Murgov (2004). Animicrobial testings and chiral phase gas chromatographic analysis of dill oils and related key compounds, Ernährung/Nutrition, **28**, № 6, p. 257.
12. Kostova I., D. Dimitrov, M. Ivanova, R. Vlaseva, S. Damianova, N. Ivanova, A. Stoyanova, O. Gubenia (2014). The possibilities of using of essential oils in dairy products. 2. Dill (*Anethum graveolens*), Ukrainian Food Journal, **3**, Issue 4, p. 516.
13. Lawrence B. (1996). Dill oil, Perfumer and Flavourist, **21**, p. 64.
14. Lopez P., C. Sanchez, R. Batlle, C. Nern (2005). Solid- and vapor-phase antimicrobial activities of six essential oils: susceptibility of selected foodborne bacterial and fungal strains, Journal of Agricultural and Food Chemistry, v. **53**, № 17, p. 6939.
15. Mahmoodi A., L. Roomiani, M. Soltani, A. Basti, A. Kamali, S. Taheri (2012). Chemical composition and antibacterial activity of essential oils and extracts from *Rosmarinus officinalis, Zataria multiflora, Anethum graveolens* and *Eucalyptus globules*, Global Veterinaria, **9**, № 1, p. 73.
16. Marchev A., I. Ivanov, P. Denev, M. Nikolova, V. Gochev, A. Stoyanova, A. Pavlov, V. Georgiev . (2015). Acetylcholinesterase inhibittory, antioxidant, and antimicrobial activities of *Salvia tomentosa* Mill. essential oil, Journal of BioScience and Biotechnology, **4**, № 2, p. 219.
17. Naseri M., A. Haeidari (2006). Spasmolytic effect of *Anethum graveolens* (dill) fruit extract on rat ileum, Physiology and Pharmacology, **1**, p. 99.
18. Pino J. (1999). Herb oil of dill (*Anethum graveolens* L.) grown in Cuba, Journal of Essential Oil Research, **7**, p. 219.
19. Ortan A., M. Popescu, A. Gaita, C. Dinu-Pîrvu, G. Câmpeanu (2009). Contributions to the pharmacognostical study on *Anethum graveolens*, Dill (*apiaceae*) **,** Romanian Biotechnological Letters, **14**, № 2, p. 4342.
20. Radulescu V., M. Popescu, D. Ilies (2010). Chemical composition of the volatile oil from different plant parts of *Anethum graveolens* L. (*Umbelliferae*) cultivated in Romania, Farmacia, **58**, № 5, p. 594.
21. Re R., N. Pelegrini, A. Proteggente, A. Pannala, M. Yang, C. Rice-Evans (1999). Antioxidant activity applying an improved ABTS radical cation decolorization assay. Free Radical Biol. Med., **26**, № 9/10, p. 1231.
22. Russian Pharmacopoeia. Moscow (1990).
23. Saleh-e-In M., A. Sultana, M. Husain, S. Roy (2010). Chemical constituents of essential oil from *Anethum sowa* L. herb (leaf and stem) growing in Bangladesh, Bangladesh Journal of Scientific and Industrial Research, **45**, №2, p. 173.
24. Seo S.-M., J. Kim, S.G.Lee, C.H. Shin, S.C. Shin, I.K. Park (2009). Fumigant antitermitic activity of plant essential oils and components from ajowan (*Trachyspermum ammi*), allspice (Pimenta dioica), caraway (*Carům carvi*), dill (*Anethum graveoiens*), geranium (*Pelargonium graveoiens*), and litsea (Litsea cubeba) oils against Japanese termite (*Reticulitermes speratus kolbe*)**,** Journal of Agricultural and Food Chemistry, **57**, № 15, p. 6596.
25. Shyua Y.-S., J.-T. Linb, Y.-T. Changc, C.-J. Chiangd, D.-J. Yangd (2009). Evaluation of antioxidant ability of ethanolic extract from dill *(Anethum graveolens* L.) flower, Food Chemistry, **115**, № 2, p. 515.
26. Singh G., S. Maurya, M. de Lampasona, C. Catalan (2005). Chemical constituents, antimicrobial investigations, and antioxidative potentials of *nethum graveolens* L. essential oil and acetone extract: Part 52, Journal of Food Science, **70**, № 4, p. 208.
27. Thaipong K., U. Boonprakob, K. Crosby, L. Cisneros-Zevallos, D. Byrne (2006). Camparasion of ABTS, DPPH, FRAD, and ORAC assay for estimating antioxidant activity from guava fruit extracts, J. Food Comp, Anal.: an official publication of the United National University, International Net work of Food Data Systems, 19, № 6/7, p. 669.
28. Vera R., J. Chane-Ming (1998). Chemical composition of essential oil of dill (*Anethum graveolens* L.) growing in Reunion Island, Journal of Essential oil Research, v. **10**, № 5, p. 539.
29. Vokk R., T. Lõugas, K. Mets and M. Kravets (2011). Dill (*Anethum graveolens* L.) and

parsley (*Petroselinum crispum* (Mill.) Fuss) from Estonia: Seasonal differences in essential oil composition, Agronomy Research 9 (Special Issue II), p.515.

30. Zaika L. (1988).Species and herbs: their antimicrobial activity and its determination, Food Safety, p. 97.

ANNUAL OF ASSEN ZLATAROV UNIVERSITY, BURGAS
BULGARIA, 2017, v. XLVI (1)

INFRARED STUDY ON VEGETABLE OILS AGING PROCESSES

Krasimira Georgieva, Petko Petkov, Nikola Todorov, Yordan Denev
E-mail: krasiianeva@yahoo.com

ABSTRACT

The aim of present work is the study of aging processes during thermal degradation of edible oils at 130 ^{0} C. The changes in the chemical structure of the studied five different oils were analysed using two different approaches. The first approach is the calculation of a new oxidative spectroscopic index (OSI), using as a basis a limited spectral region where significant changes are observed (from 3050 to 2750 cm-1). The second approach is based on chemometric processing of the entire spectrum (from 4000 to 400 cm-1). The results clearly show that FTIR is a suitable method for analysis and quantitative determination of the changes during the thermal aging of edible oils.

Key words: *thermal aging, edible oils, FTIR, OSI, mathematical approaches*

INTRODUCTION

Edible oils contain mainly triacylglycerols, which are glycerol molecules with three long chain fatty acids attached to the hydroxy groups via ester links. Oxidation of lipids such as triacylglycerols is an undesirable chemical change that occurs at high temperature and in the presence of oxygen. The main compounds obtained in the oxidation of vegetable oils are hydroperoxides, aldehydes, alcohols and acids. Oxidation processes occur mainly in three phases: induction period, propagation phase and termination phase. The products of each of these phases increase/decrease its concentration over time, and this fact makes quantitative analysis of lipid oxidation very difficult. Multiple methods have been developed to study the oxidation of oils. These approaches are based on the measurement of the concentration of some of the oxidation products. Among these methods are iodometric titration, gas chromatography, liquid chromatography and mass spectrometry. These methods provide detailed information about the oxidation process, but are not applicable for prediction of the oils stability because they require much time for analysis. In comparison to the above methods, infrared spectroscopy is known as a reliable method for studying the degradation of lipids under the influence of oxygen [1 - 4].

In this study two main different approaches were used for the interpretation of the results obtained from the study of oil oxidative degradation and of determination of its stability. The first approach is the calculation of a new oxidative spectroscopic index (OSI), using as a basis a limited spectral region where significant changes are observed (from 3050 to 2750 cm-1). The second approach is based on chemometric processing of the entire spectrum (from 4000 to 400 cm^{-1}) to obtain the necessary information. The results of the application of the two approaches are compared in order to assess their reliability.

EXPERIMENT

The characteristics of the used vegetable oils are desribed in Table 1 (1-olive oil; 2-sunflower oil; 3-palm oil; 4-soybean oil; 5-corn oil).

Table 1. Composition of the studied oils

Carboxylic acids, %	Oil				
	1	2	3	4	5
Saturated	14.1	12.5	40	15	14.5
Monounsaturated	68.3	22.5	46	24	33
Polyunsaturated	9.2	57.5	14	61	52.5

Accelerated oxidative aging of oils was conducted in pot furnace at 130°C in the presence of air. The aging was conducted for 2 hrs and samples for the analysis were taken every 40 min. The infrared spectra of the vegetable oils were recorded with a Fourier transform infrared spectrometer, Bruker Tensor 27, interfaced to a personal computer operating under Windows-based software OPUS 6.5. All spectra were recorded from 4000 to 400 cm^{-1} with resolution better than 4 cm^{-1}, co-adding 32 interferograms with frequency resolution better than 0.01 cm^{-1}. A thin film of a small amount of each sample (approxi-

mately 2 μL) was deposited between two discs of KBr to avoid the presence of air. The frequency of each band was obtained automatically using command of the instrumentation software OPUS 6.5.

RESULTS AND DISCUSSION

The infrared spectra of studied oils are shown in figure 1.

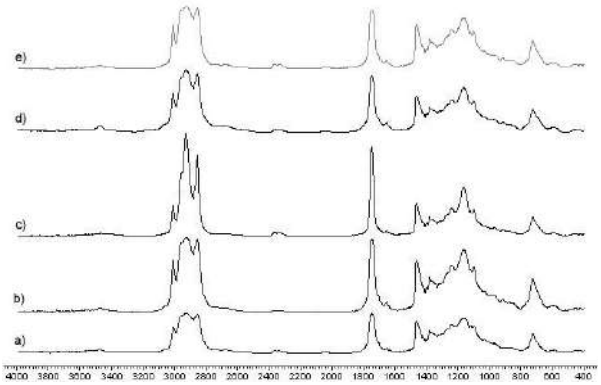

Fig.1. Infrared spectra of studied oils: a) olive oil; b) sunflower oil; c) palm oil; d) soybean oil and e) corn oil

The association of bands to specific functional groups was made by comparison of the peak frequencies with literature data for vibrational mode in fats and oils [5]. The numerical values of wave numbers corresponding to the functional groups of the analyzed oils were identified directly from the recorded IR spectra as shown in Table 2.

Table 2. Infrared absorbance bands used in studied spectra

Wavenumbers, cm^{-1}	Function	Type of vibrations
3450	OH	Stretching
≈ 3008	CH	Stretching
2953	CH	Asymm. stretching
2925	CH	Asymm. stretching
2854	CH	Symm. stretching
1746	C=O	Stretching
1463	CH	Scissoring
1376	CH	Symm. deformation
1238	CH	Out of plane bend
1164	C-O	Stretching
1025	C-O-C	Stretching
966	CH	Out of plane bend
722	CH	Rocking

An oxidative spectroscopic index (OSI) (Equation 1) was used for monitoring the kinetics of oil aging:

$$I_{C=C} = \frac{\left[sp^2/\left(sp^2+sp^3\right)\right]T_t}{\left[sp^2/\left(sp^2+sp^3\right)\right]T_0} \quad (1)$$

where sp^2 is the area of the cis-CH stretching vibration band (HC=C), centered at 3008 cm^{-1} and (sp^2 +sp^3) is the area from 3050 to 2750cm^{-1} including the cis-CH band and the -CH asymmetric and symmetric stretching bands from CH_3 and CH_2 aliphatic compounds. Areas are measured at given time (T_t) and at the initial time (T_0). This relative index is based on ratio between area values rather than absolute absorbance values to eliminate all variations due to the preparation and to the thickness of samples. For initial spectra, the index was equal to 1. The OSI values of studied oils in the aging period were shown in the table 3 (1-olive oil; 2-sunflower oil; 3-palm oil; 4-soybean oil; 5-corn oil).

Table 3. Values of oxidative spectroscopic index of oils during the aging

Time, min	OSI				
	1	2	3	4	5
0	1	1	1	1	1
40	0.777	0.921	0.914	0.824	0.928
80	0.406	0.860	0.882	0.813	0.660
120	0.526	0.820	0.879	0.790	0.592

The data clearly show the lack of a lasting trend in the change of values of oxidative spectroscopic index. This is evidence of the complex processes that accompany the oxidation of lipids and the diversity of products that are formed during aging. Obviously, the concentration of different products varies substantially in different stages of thermal degradation.

It is well known that the high content of unsaturated acids in vegetable oils makes them more sensitive and susceptible to oxidation [6]. The next figures (Figures 2-6) describe the changes in spectra of olive oil in different times during aging at 130 °C in two separate spectral regions.

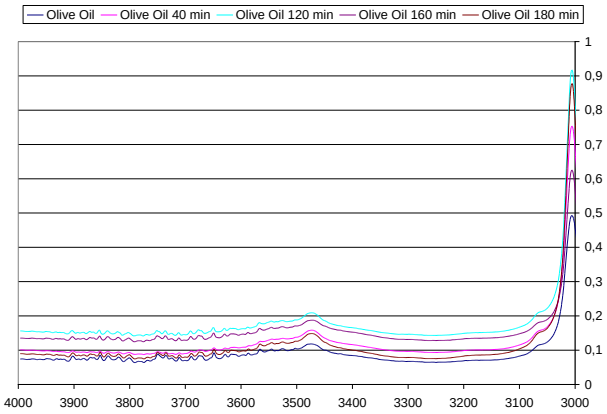

a)

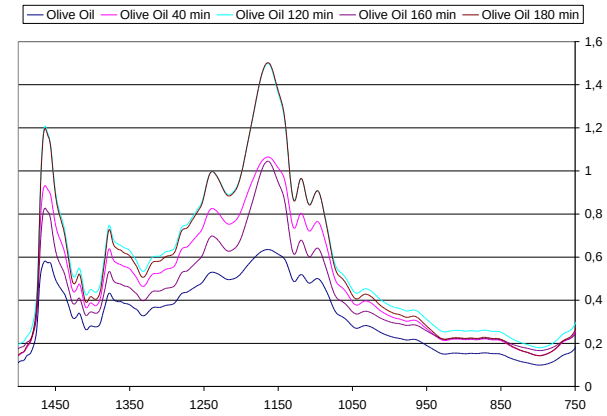

b)

Fig. 2. Infrared spectra of olive oil in different times of aging:
from 3000 to 4000 cm^{-1} (a) and from 750 to 1500 cm^{-1} (b)

During the oxidation, the band at 3008 cm^{-1} associated with the vibration of the double bonds of the aliphatic chains reduces their intensity after the induction period of aging (fig. 3a). There are numerous other spectral changes in the rest of the infrared region. A band at 3473 cm^{-1} associated with overtones of the carbonyl absorption of triglycerols or overlapping shifts of the more intense band at 3464 cm^{-1} (Fig. 3a).

This peak is explained by the presence of hydroperoxides which are the primary products of oxidation [7]. After the induction period, a new band appears in the higher wave numbers area (3535 cm^{-1}). This frequency is characteristic for alcohols or secondary products of oxidation [7, 8] and increases its intensity. This is evidence that the concentration of these products increased after the induction period.

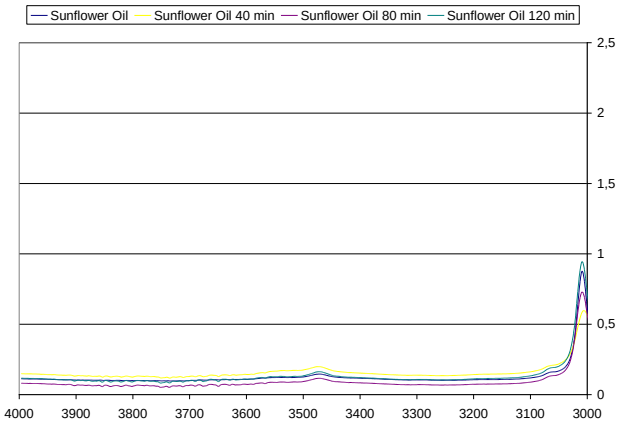

a)

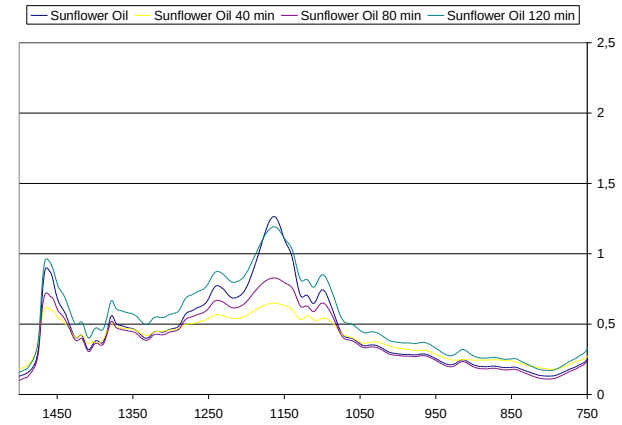

b)

Fig. 3. Infrared spectra of sunflower oil in different times of aging:
from 3000 to 4000 cm^{-1} (a) and from 750 to 1500 cm^{-1} (b)

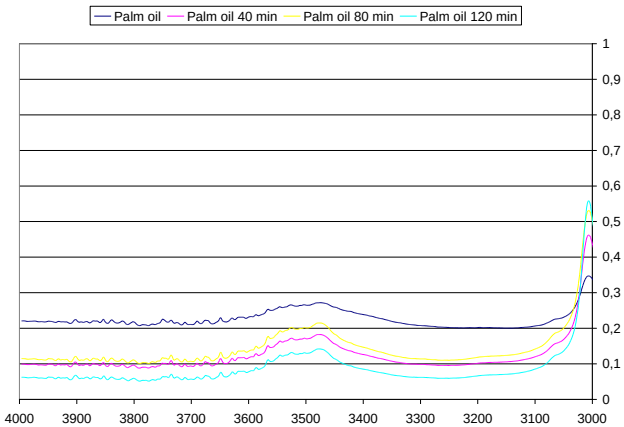

a)

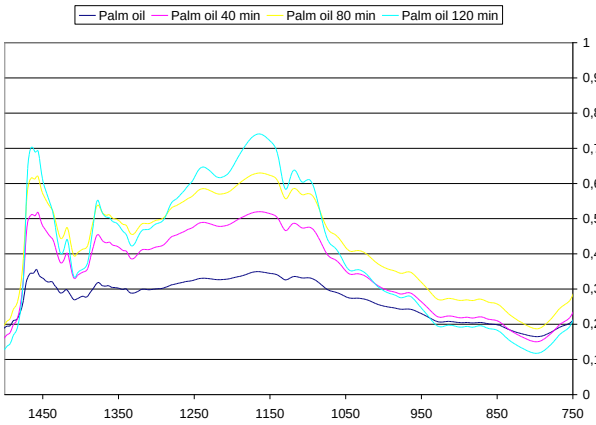

b)

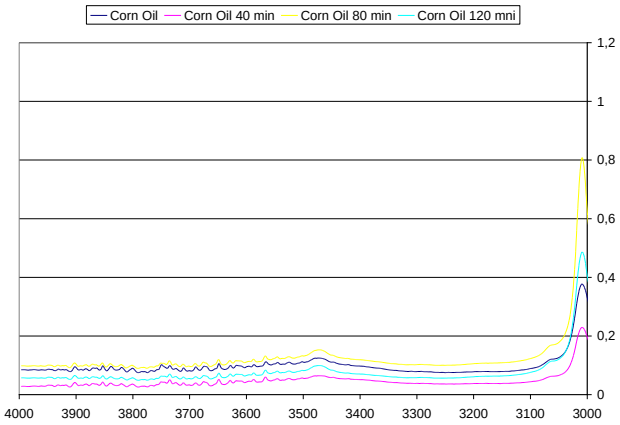

a)

Fig. 4. Infrared spectra of palm oil in different times of aging:
from 3000 to 4000 cm^{-1} (a) and from 750 to 1500 cm^{-1} (b)

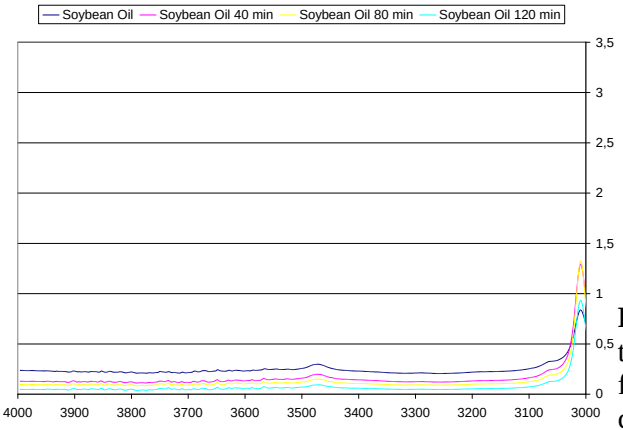

a)

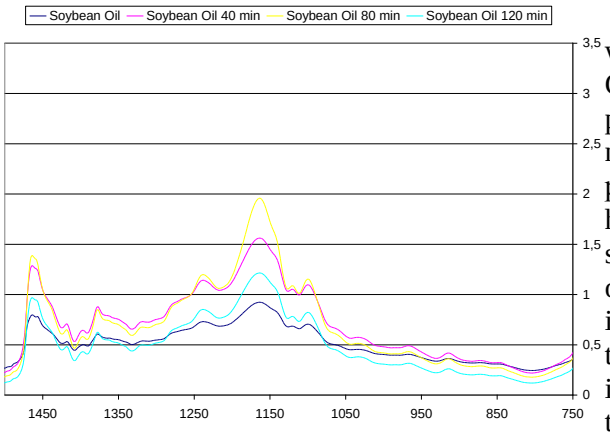

b)

Fig. 5. Infrared spectra of soybean oil in different times of aging:
from 3000 to 4000 cm^{-1} (a) and from 750 to 1500 cm^{-1} (b)

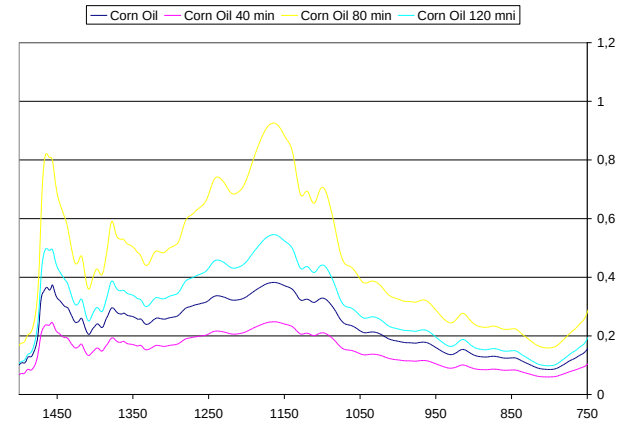

b)

Fig. 6. Infrared spectra of corn oil in different times of aging:
from 3000 to 4000 cm^{-1} (a) and from 750 to 1500 cm^{-1} (b)

Fresh oils show a weak band at 1645 cm^{-1}, which is associated with stretching vibrations of C = C cis-olefins (Fig. 3b). It decreases or disappears with increasing of oxidation process and a new band appears at 1627 cm^{-1}, which is explained by the presence of α, β-unsaturated aldehydes and ketones [9]. There is also a weak absorption at 966 cm^{-1}, which is responsible for out of plane bending of CH functional groups from isolated trans-alkenes. It overlaps after the induction period of two low-intensity bands. The first is positioned at 987 cm^{-1} and is associated with the bending vibrations of CH trans-conjugated olefinic groups [9]. The second, at 975 cm^{-1}, is associated with secondary oxidation products such as aldehydes and ketones with isolated trans-double bonds. The band at 987 cm^{-1} rapidly disappears after induction period at the expense of increasing the intensity of the band at 975 cm^{-1}. The compounds with conjugated double bonds (as defined by the strips at 966 and 987 cm^{-1}) are intermediate products of the oxidative process.

This fact is confirmed by a number of literature sources [10, 11]. The infrared spectra of studied oils in region 1600 – 1850 cm^{-1} are shown in Figure 7.

During the oxidation at the moment when the cis-CH band begins to decrease, the expansion of a band at 1746 cm^{-1} associated with the C = O carboxyl group of triglycerols increases its intensity. At the same time, increasing of oxidation is observed and the appearance of peak at 1721 cm^{-1} associated with the CO group of aliphatic aldehydes [12] and 1706 cm^{-1} associated with free fatty acids [13].

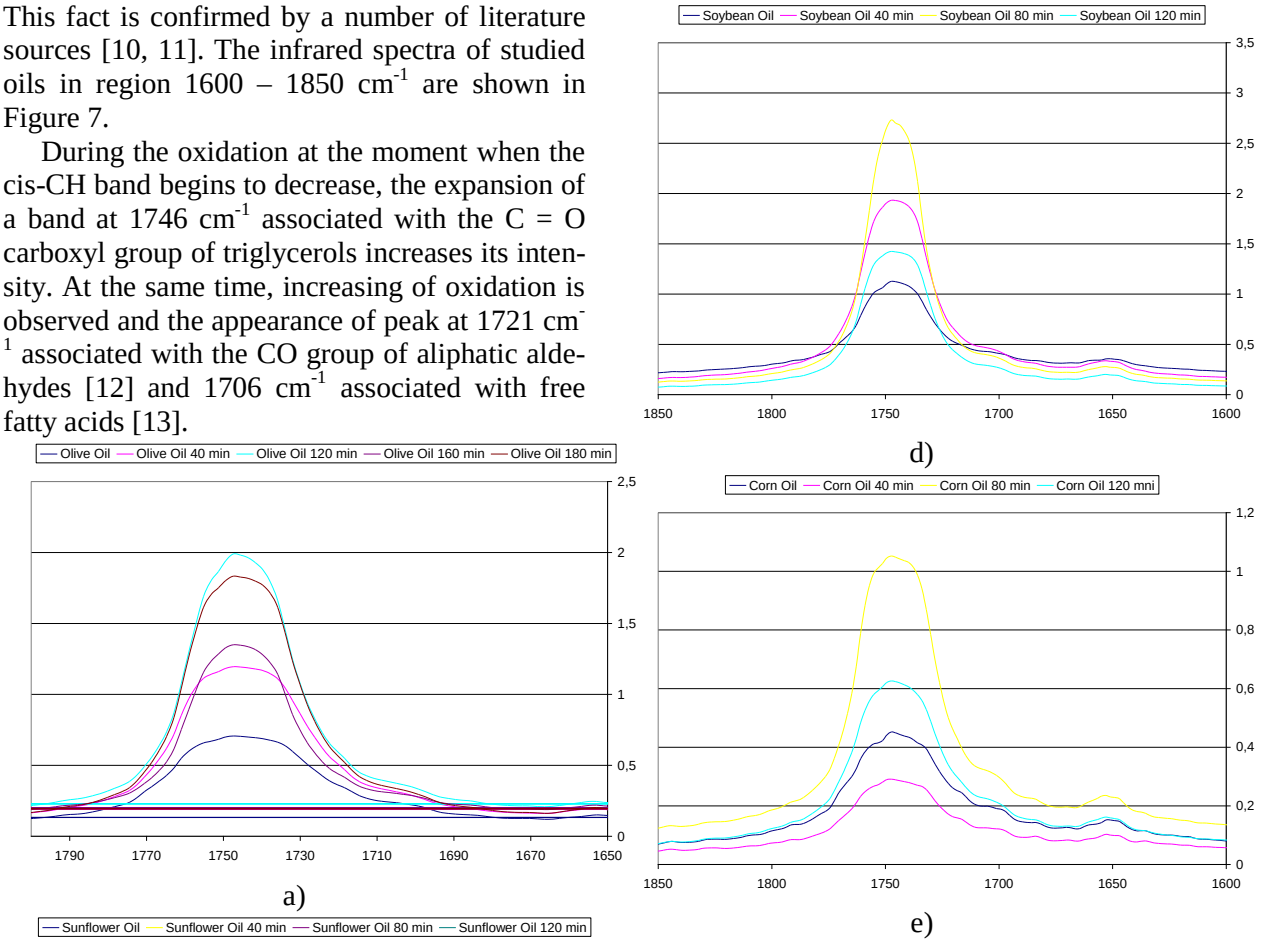

Fig. 7. Infrared spectra of studied oilds during the oxidation in region 1600 – 1850 cm^{-1} (a-olive oil; b-sunflower oil; c-palm oil; d-soybean oil; e-corn oil)

There is also a peak at 1786 cm^{-1}, which can be explained by the CO group of acetic acid [14]. The changes in the spectra at selected wave numbers were tracked and as expected, according to the literature, there is an increase in absorption for all selected frequencies except 3008 and 710 cm^{-1}. The increase in intensity is logically connected with the apparent increase in the concentration of products and the reduction in the above positions is related to the disappearance of cis-isomerisation links because of the oxidation process.

Most of the absorbance values show three distinct phases, as shown by the results described in the literature [15]: they start with a different induction period, during which there is a little variation in absorbance intensity; later they increase (or decrease) its intensity during the oxidation phase at distinct rates for different functional groups; sharpest decrease (or potential reduction to zero) intensity is a proof of the end of the oxidation process.

From the experimental data there is clearly a tendency of increase in the intensity of the two bands at 985 and 970 cm^{-1}, followed by stabilization. Absorbance at 970 cm^{-1} is increased to a higher degree than that at 985 cm^{-1}, although at the end of the study, both bands have almost the same absorbance intensity.

CONCLUSIONS

The thermal oxidative decomposition of the vegetable oils at 130°C in the presence of oxygen from the air was studied. The complex mechanism of degradation was assessed by calculating the oxidative spectroscopic index during the whole process of aging. The obtained values clearly prove the presence of three phases of degradation, which correlates with mechanisms data described in the literature. The infrared spectra of the edible oils over a period of time were studied and relationships in some characteristic bands describing specific degradation products (alcohols, aldehydes and ketones) were established. It was demonstrated and proved the possibility of using of the infrared spectral analysis for evaluation of oxidative processes occurring in vegetable oils during aging. The results can be used for choosing suitable sources for biodiesel fuel synthesis and for describing their use and behaviour.

REFERENCES

1. Stuart B. *Infrared Spectroscopy: Fundamentals and Applications*; Wiley & Sons, 2004, pp. 45-48.
2. Smith B. *Fundamentals of Fourier Transform Infrared Spectroscopy*; CRC Press, 2011, pp. 2-8.
3. Le Dreau Y., N. Dupuy, J. Artaud, D. Ollivier, J. Kister. Infrared study of aging of edible oils by oxidative spectroscopic index and MCR-ALS chemometric method. – *Talanta*, 2009, v.77, pp. 1748- 1756.
4. Climaco Pinto R., N. Locquet, L. Eveleigh, D.N. Rutledge. Preliminary studies on the mid-infrared analysis of edible oils by direct heating on an ATR diamond crystal. – *Food chemistry*, 2010, v.120, pp. 1170- 1177.
5. Safar M., D. Bertrand, P. Robert, M. F. Devaux, C. Genot. Characterization of edible oils, butters and margarines by Fourier transform infrared spectroscopy with attenuated total reflectance. – *Journal of Oil & Fat Industries*, 1994, v.71(4), pp. 371-377.
6. Neff, W.E., El-Agaimy, M. Effect of Linoleic Acid Position in Triacylglycerols on their Oxidative Stability. – *Lebensmittel-Wissenschaft und-Technologie*, 1996, v.29 (8), pp. 772-775.
7. van de Voort, F.R., A.A. Ismail, and J. Sedman. A Rapid, Automated Method for the Determination of cis and trans Content of Fats and Oils by Fourier Transform Infrared Spectroscopy, - *J. Am. Oil Chem. Soc*., 1995, v.72, pp. 873–880.
8. Yang H.,Irudayaraj J. & Paradkar M.M. Discriminant analysis of edible oils and fats by FTIR, FT-NIR and FT-Raman spectroscopy. – *Food Chem*., 2005, v.93(1), pp. 25-32.
9. Frankel E.N. Lipid oxidation: mechanisms, products and biological significance. – *J. Am. Oil Chem. Soc*., 1984, v.61(12), p. 1908-1917.
10. Moreno M.C., D. Mendoza Olivares, F.J. Amezquita Lopez, V. Peris Martinez, F. Bosch Reig. Determination of unsaturated grade and trans isomers generated during thermal oxidation of edible oils and fats by FTIR. – *Journal of Molecular Structure*, 1999, v. 482–483, pp. 557-561.
11. Guillén M.D., N. Cabo. Some of the Most Significant Changes in the Fourier Transform Infrared Spectra of Edible Oils under Oxidative Conditions. - *Journal of the Science of Food and Agriculture*, 2000, v.80(14), 2028-2036..
12. Tay A., R.K. Singh, S.S. Krishnan, J.P. Gore. Authentication of Olive Oil Adulterated with Vegetable Oils Using Fourier Transform Infrared Spectroscopy. – *Lebensmittel-Wissenschaft und-Technologie*, 2002, v.35(1), p. 99.
13. Guillén MD, Cabo N. Study of the effects of smoke flavourings on the oxidative stability of the lipids of pork adipose tissue by means of Fourier transform infrared spectroscopy. – *Meat Science*, 2004, v.66(3), pp. 647-657
14. Shimanouchi T. National Bureau of Standards 1 (1972).
15. Priéri F.; Gresser, E.; Le Dréau, Y.; Obiols, J.; Kister, J. New Method of Simulation to Evaluate the Sensitivity to Oxidation of Lubricating Oils: An Aging Cell Coupled with Fourier Transform Infrared Spectroscopy. – *Applied Spectroscopy*, 2008, v.62(7), pp. 810-816.

ANNUAL OF ASSEN ZLATAROV UNIVERSITY, BURGAS
BULGARIA, 2017, v. XLVI (1)

DEPOLYMERIZATION OF PET WITH GLYCERIDES OF OLEIC ACID

Nikola Todorov, KrasimiraYaneva, YordanDenev
E-mail: steel_nick@yahoo.com

ABSTRACT

With the increased use of polyethylene terephthalate (PET) as packaging material, as well as biodiesel production, the necessity has arisen to utilize the waste PET and the crude glycerol whichis a side product of biodiesel production. The present paper describes a possibility to obtain glycerides of the oleic acid and crude glycerol followed by a chemical recycling of PET waste with the glycerides of the oleic acid (GOA) synthesized.Numerous depolymerization processes were carried out under varying conditions:weight ratio GOA/PET, temperature, process duration and content of catalyst.The products of the depolimerization were studied by spectral methods of analysis.

Keywords*:chemical recycling, waste PET, utilization, glycerides*

INTRODUCTION

As a pressing measure in the struggle with the ecologic crisis, Directive 94/62 EU on packaging and packaging waste was adopted by the European Parliament and Council.The essential requirements of the Directive include: minimizing the weight and volume; minimizing the content of hazardous substances and the designof packaging to permit its reuse or recovery [1].

Polyethylene terephthalate (PET) is a polymer complying with all the criteria. It has excellent properties, structural strength and crystal transparency which creates good appearance and provides numerous possibilities for application in attractive packaging where the product contained can be clearly seen, it is resistant to breaking and does not whiten under bending. PET is easily processed thermally and is stable at temperatures from -40˚C to +70˚C. It is non-toxic and environment friendly. It is also safe in contact with food products and medications, for printing and gluing.

In the last decade, it became the most suitable material for beverage bottles and packaging for food and medications. According to the report of Smithers Pirafor 2014, the world production of PET packaging has reached 16 million tons and it is expected to increase on the average by 4.6% per year to reach 19.9 million tons in 2019 [2]. PET packaging for food products is usually discarded by the consumers in less than a month. About 29% of PET packaging is reused – mainly in the developing countries. The rest of the amount of PET bottles (more than 70%) is discarded as waste. They are the biggest polymer contaminant in the environment and it is the most widely spread plastic in waste depots. PET accounts for about 8% of the weight and 12% of the volume of the hard wastes in the world [3]. PET does not pose direct threat for the environment when deposited but it is considered to be a hazardous material because its high volume and high durability (more than 100 years) lead to overfilling of waste depots [4].

PET wastes can be recycled, which is completely in accordance with environment protection. A number of methods for PET recycling have been published in the literature, e.g. hydrolysis, glycolysis, methanolysis and aminolysis[3]. Glycolysis takes place under the action of various monomer compounds with two or more OH groups – monoethylene glycol, diethylene glycol[3], pentaeriythritol[4],glycerol [5], etc.

No data were found in the available literature on the depolymerization of PET with glycerides obtained from oleic acid (OA) and crude glycerol (CGly). CGlyis a side product of biodiesel production. Usually, 1 t. biodiesel is produced from 1 t. oil and 110 kg methanol, which gives 110 kg glycerol which is non-refined – crude glycerol. According to Directive 2003/30/ of the European Union, 5.75% of the diesel fuel offered at the petrol stations should be “bio” in 2010 and 20% in 2020.With the increase of biodiesel production, the amounts of crude glycerol rapidly grew. On world scale, methods are researched for the

utilization of this side product [3] which is essential for the support of the biodiesel industry.

From ecological point of view, the utilization of both waste materials – PET and crude glycerol is very important, which is themain issue of the present paper: to synthesize glycerides from oleic acid and crude glycerol and use them for depolymerization of PET waste.

2.EXPERIMENT

1. Materials

Polyethylene terephthalate,obtained from beverage bottles.

Crude glycerol,purchased on the market.

Oleic acid, toluene, methanol, KOH, ethanol and tetrahydrofuran were purchased from Sigma Aldrich. The deionized water was prepared using the system for pure/ultra-pure water Purelab PRIMA of Thermo Scientific.

2. Preparation of glyceridesof the oleic acid (GOA)

In a round bottomed flask of 500 ml equipped with mechanical stirrer, Dean-Stark apparatus, thermometer and inert gas inlet, certain amount (Table 2) of crude glycerol and toluene (4,5 mass% with respect to the amount of glycerol) were placed. The stirrer was turned on and the flask was heated to the boiling temperature until full evaporation of the water contained in the crude glycerol. A calculated amount of heated to 180ºC oleic acid (Table 2) was added to the glycerol, as well as 5% preliminarily prepared glycerides. The interaction proceeded for 90 min at temperature of 180°C. Samples were taken in 15 min intervals and the acid number was determined. The conversion of the oleic acid was calculated by the following equation:

$$C_{OA},\% = \frac{A_i - A_t \,.\, 100}{A_i} \qquad (1)$$

where: $A_i$is the initial acid number;$A_t$is the acid number at moment t.

After turning the stirrer off, three layers formed which were separated in hot state with a separating funnel. The upper layer (glycerides) were rapidly cooled in water bath to temperature of 75°C,washed several times with water and extracted with methanol.The lowest layer (NaCl) was washed with methanol and dried.

3. Depolymerization of PET

In a round bottomed flask of 500 ml equipped with mechanical stirrer, thermometer and inert gas inlet, a certain amount of glycerides and catalyst (Table 3) were placed and heated to the necessary temperatureand then PET flakes were added. Processes of transesterification were carried out with durations from 6 to 8 hrs at temperatures 180, 190 and 200°C. The products obtainedwere cooled to room temperature and ethyl acetate was added to obtain solution and precipitate. The solution was decanted and distilled at low pressure to extract the ethyl acetate for reuse. After evaporating the moisture, the product of the depolymerization was obtained (PD). Hot deionized water was added several times to the precipitate to remove the non-reacted glycerol and NaCl. The non-solved PET was dried and its conversion was determined by the formula:

$$C_{PET},\% = \frac{W_i - W_f \,.\, 100}{W_i} \qquad (2)$$

where: W_i and$W_f$are the initial and final weight of PET, respectively

4. Analyses and characterization

The UVspectra were registered on a spectrophotometer Evolution 300 UV VISof Thermo Scientific Co. in a solution in THF in a 1 cm thick cuvette.

The FT IR spectra were taken on a spectrophotometer Nicolet IS 50 FT IR with thin film samples fixed on a KBr pellet.

Gel permeation chromatography was used to determine the molecular mass distribution.

RESULTS AND DISCUSSION

The studies were carried out in two stages. The first one was to obtain glycerides from oleic acid. Some important characteristics of the initial materials were determined (Table 1).

The content of free glycerol, water and ashes were determined by standard methods and the contents of matter organic non-glycerol (MONG) – from the difference (100 – [glycerol content,% +water content,% + ashes content, %]).

Table 1. Some important characteristics of crude glycerol and oleic acid

Characteristic	CGly	OA
Content of glycerol, wt %	80.5	-
Content of water, wt %	8.5	-
Content of MONG, wt %	4.9	-
Content of ashes, wt %	6.1	
Density at 20°C, g/cm^3	1.15	0.887
Content of OA,%		99
Solubility in Water	yes	no
Solubility in Methanol	yes	no
Solubility in Tetrahydrofuran	no	yes

It can be seen from Table 1 that the densities of CGlyand OA are quite different. This is the main problem for the interaction which should occur between them. The incompatibility is the reason to obtain di- and even triglycerides. To realize proper contact and obtain high content of monoglycerides, a number of conditions must be provided: intense stirring, excess of glycerol, temperature lower than 200°C. Numerous syntheses were carried out aiming to find the optimal conditions for the preparation of monoglycerides.

The conditions employed for four of them show the peculiarities of the process studied (Table 2). The samples denoted Gl-1, Gl-2 and Gl-4were obtained at CGly/OA ratio 1,2; 2,0 and 3,0, respectively, aiming to find out the importance of the excess of glycerol. In samples denoted Gl-2, Gl-3 and Gl-4, preliminarily prepared glycerides were added /Gl_{in}/.

Table 2.Contents of monoglycerides by varying synthesis conditions

	CGly, g	OA, g	CGly/OA, mol	Gl_{in}, %	Content of MG, %
Gl-1	54.8	113	1,2	-	43
Gl-2	80.0	98.9	2,0	3	55
Gl-3	80.0	98.9	2,0	5	68
Gl-4	102.8	84.8	3,0	5	69

The reaction was monitored by measuring the change of the acid number. Samples were taken every 15 min and the acid number was determined by a standard method. The conversion was calculated (Fig.1) by equation (1).

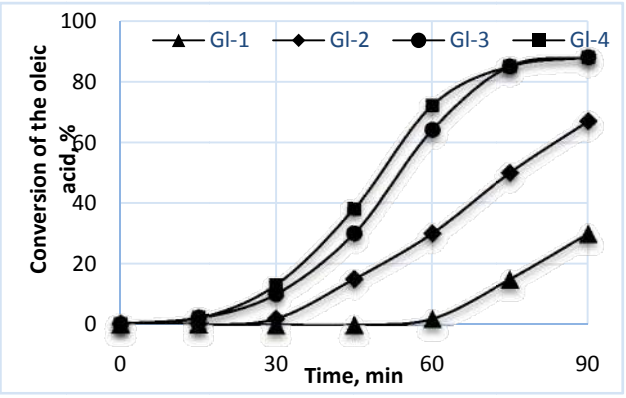

Fig.1. Conversion of oleic acid with time for Gl-1,Gl-2,Gl-3 andGl-4

As can be seen from Fig.1, Gl-1 had long induction period (about 1 hr) before registering some change.ForMG-2, this induction period was reduced to 30 min while for MG-3 andMG-4 the esterification began as early as the 15th minute. Different reaction rates were observed for the four samples.

After turning the stirrer off, three layers were obtained which were separated in hot state with a separating funnel.The lowest layer was NaCl.NaClhas good solubility in glycerol (6.1%) but it is insoluble in glycerides. After washing with methanol, the salt may be used for non-nutritious purposes. The middle layer was glycerol. It can be reused for preparation ofglycerides. The upper layer consisted mainly of glycerides. They were washed several times with water and extracted with methanol. The contents of monoglycerideswere determined by standard methods[9].It can be seen from the results (Table 2) that, although at a lower rate, glycerides of the oleic acid can be obtained without adding a catalyst because the impurities (MONG and salts) have themselves a catalytic effect. The addition of glycerides leads to a reduced induction period and increased content of monoglycerides.

The results obtained show that the main process taking place is:

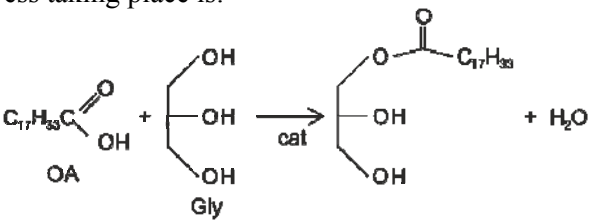

Scheme 1.Esterification of crude glycerol and oleic acid

It is important in this case to consider the effect of the impurities present in CGly. Table 1 shows that these are water, MONG and NaCl. Water is easily removed before the synthesis. The main components of MONG are fatty acids, methyl esters of fatty acids (FAMEs), mono-, di- and triglycerides. Under the conditions of the esterification, all the components can react with glycerol which results in the formation of monoglycerides (or diglyerides).Simultaneously, low molecular weight products are released (water or methanol), which are blown off by the inert gas. The last impurity is the salts, in this case NaCl which is insoluble in glycerides and can easily be separated.

The second stage in the present work was to carry out depolymerization of flakes of waste PET using the glycerides obtained at stage one.Numerous transesterifications were performed under varied conditions:temperature (T), weight ratio (GOA/PET), process duration (τ) and amount of catalyst (Table 3).The catalyst used in all depolymerizationprocesses was NaCl, which was released in the synthesis of glycerides (section 2.2.).

Table3.Conversion of PET under varied conditions

	T, ºC	τ, h	Cat., %	Weight ratio GOA/PET	C_{PET}, wt %
DG-1	180	7	1.5	4	38
DG-2	190	7	1.5	4	68
DG-3	200	7	1.5	4	91
DG-4	210	7	1.5	4	92
DG-5	200	6	1.5	4	78
DG-6	200	8	1.5	4	91
DG-7	200	9	1.5	4	92
DG-8	200	7	-	4	33
DG-9	200	7	2	4	92
DG-10	200	7	1.5	2	46
DG-11	200	7	1.5	3	78
DG-12	200	7	1.5	5	92

It can be seen from the Table that the optimal conditions for the transesterification process were: temperature 200ºC, mass ratio (GOA/PET)4, catalyst content 1,5 % with respect to PET PET and process duration 7 h.

After the transesterification process, a complex mixture of depolymerized products, non-reacted GOA, NaCl and PET was obtained. The depolymerized products were extracted with ethyl acetate. Some of its important characteristics are compared (Table 1) to those of the initial materials (PET and GOA).

Table 4.Some characteristics of polyethylene terephthalate (PET),glycerides of the oleic acid (GOA) and of depolymerized products (DP).

Characteristic	PET	GOA	DP
Physical state	solid	liquid	wax like
Color	colorless	brown	light brown
Thermo stability, °C	400	220	240
Solubility in:			
Methanol	no	yes	no
THF	no	yes	yes
Ethyl acetate	no	yes	yes

Obviously, the polymer molecules of PET flakes have been transformed into oligomer ones.

The chemical bonds were studied by spectral methods.

The UV spectra of the products dissolved in THF showed an absorption band in the interval 240-300 with maximum at 292 nm, which corresponds to the terephthalate units.

The following characteristic frequencies were found in the IR spectrum of the purified products:

♦3447 – broad band for intermolecular OH groups;

♦3100-3000 cm $^{-1}$ – stretch vibrations of the=C-H bond;

♦2926 and 2855 cm $^{-1}$ – stretch (asymmetric and symmetric, resp.) vibrations of the CH_2-groups;

♦2956 and 2878 cm $^{-1}$ – stretch (asymmetric and symmetric, resp.) vibrations of the CH_3-groups;

♦1727 cm $^{-1}$ – stretch vibrations of the C=O bonds;

♦1505 and 1595 cm $^{-1}$ – stretch vibrations of aromatic rings;

♦1462 cm $^{-1}$ – bending vibrations of the CH_2-groups;

♦1410 cm $^{-1}$ – bending vibrations of the C-H bond in the CH_2-O groups;

♦1378 cm $^{-1}$ – bending vibrations of the CH_3-groups;

♦1271 and 1174 cm $^{-1}$ – stretch vibrations of the C-O-C bonds;

♦1117 and 1049 cm $^{-1}$ – stretch vibrations of the C-O bonds in the C-OH groups;

♦1019 and 896 cm $^{-1}$ – p-substituted aromatic rings;

♦732 – ρ (CH_2)

The presence of characteristic Absorption Frequencies for both terephthalate units and glyceride units suggests that the depolymerization of PET with monoglycerides proceeded along the following scheme:

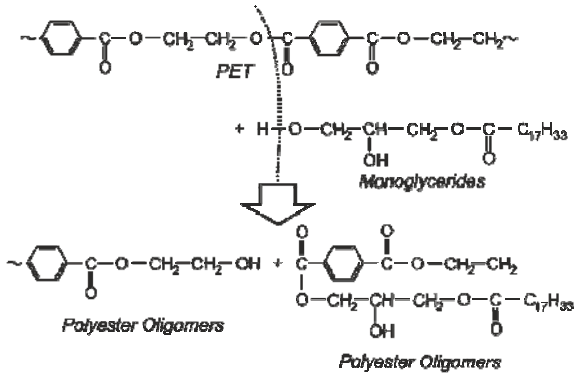

The precursor oligomers obtained can successfully be used as model compounds for chromatographic and spectral analyses, as well as for synthesis of alkyd resins.

CONCLUSION

The present paper describes a possibility to utilize both wastes from PET beverage bottles and crude glycerol, which is a side product of biodiesel production. To determine the optimal conditions for the preparation of glycerides of the oleic acid, numerous syntheses were carried out.It was found out that the impurities present in the crude glycerol (MONG and salts) have a certain catalytic effect. The addition of preliminarily prepared glycerides results in a shorter induction period of esterification and an increased content of monoglycerides.

The glycerides of oleic acid synthesized were successfully used as depolymerizing agent for PET.By varying the conditions,the best ones for the transesterification were found to be: temperature 200ºC, mass ratio GOA/PET = 4, process duration 7 hrs and amount of catalyst 1,5%. UsingFT IR and UV spectroscopy, it was proved that precursor polyester oligomers were obtained.

REFERENCES

1. Directive 94/62/EU of the European Parliament and of the Council of 20 December 1994 on packaging and packaging waste.

2.http://www.smitherspira.com/news/2014/april/demand-for-pet-packaging-material-in-2019

3.Geyer, B., G. Lorenz, and A. Kandelbauer, Recycling of poly (ethylene terephthalate), A review focusing on chemical methodsExpress Polymer Letters, *Express Polym Lett*, 2016, Vol.10, No.7, 559–586.

4. Monroy - Barreto, M., N. Esturau - Escofet, M. Romero - Ávila, and J. Recillas - Mota, NMR characterization of pentaerythritol glycolysis products of polyethylene terephthalate**,** *Int. J. Polymer Analysis & Characterization*, 2017, Vol. 22, p. 11-16.

5. Todorov, N, and D. Todorova, Study on the possibility to utilize crude glycerol and waste polyethylene terephthalate for production of alkyd resins, *IJSR, Environment Science*, 2014, Vol 3, № 10, pp.188-190.

6. Todorov, N., Synthesis of glycerides by utilization of the glycerol phase obtained by biodiesel production*, Indian J Appl Res*, 2016, Vol. 6, No.11, 2016, 697-699.

7. Xiao, Y, G. Xiao, and A. Varma, A Universal Procedure for Crude Glycerol Purification from Different Feedstocks in Biodiesel Production: Experimental and Simulation Study**,** *Ind. Eng. Chem. Res.*, 2013, Vol. *52,* No.39, 14291–14296.

8.Directive 2003/30/EC of the European Parliament and of the Council of 8 May 2003 on the promotion of the use of biofuels or other renewable fuels for transport.

9. http://www.oiv.int/public/medias/4050/e-coei-1-acigra.pdf.

**ANNUAL ASSEN ZLATAROV UNIVERSITY, BURGAS,
BULGARIA, 2017, v. XLVI (1)**

COMPARATIVE CHARACTERIZATION OF UV IRRADIATED POLYETHYLENE OXIDE FILMS CONTAINING ORGANIC COMPLEXES OF METAL ACETYLACETONATES

Mariana Tavlieva, Dimitrina Kiryakova, Atanas Atanassov
E-mail: dskiryakova@abv.bg

ABSTRACT

Polyethylene oxide films with organic complexes of metal acetylacetonates were obtained and characterized after exposure to UV light. It was found out that the irradiation for 5 hours had no significant effect on the tensile strength of the initial polyethylene oxide films. The use of iron (III) and cobalt (III) acetylacetonates at the time of the exposure reduced the strength of the materials to 0.9 and 4.5 MPa, respectively. The degradation kinetic parameters of the films prepared were determined by non-isothermal thermogravimetric analysis at a single heating rate by the Coats-Redfern method. The F_n function was chosen as the most probable mechanism function of thermal degradation of both types of polyethylene oxide films – with and without additives. It was proved that iron acetylacetonate is more effective for accelerating the degradation of polyethylene oxide foils after irradiation for 5 hours.

Key words: *non-isothermal TGA, polyethylene oxide films, metal acetylacetonates, UV light, kinetic parameters*

INTRODUCTION

In the literature there are differences on the mechanism of the processes occurring in polyethylene oxide (PEO) under UV irradiation [1, 2]. For explanation of the photooxidative destruction mechanism of polyethylene oxide (PEO) the following reactions were proposed [3, 4]:

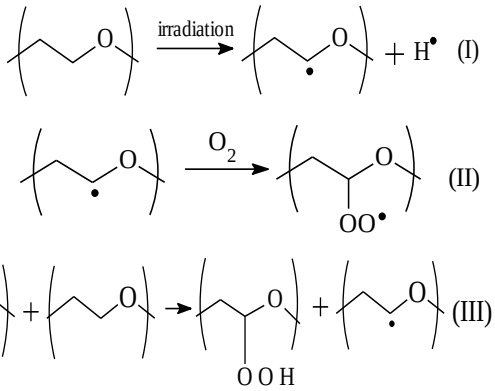

The first formed polymer radicals as a result of irradiation of PEO (1), in the presence of air, and reacted with O_2 to obtain peroxyl radicals (2). Then followed the intermolecular hydrogen abstraction and formation of the hydroperoxides (3); and homolytic cleavage of the hydroperoides (4) by photoinduced activation.

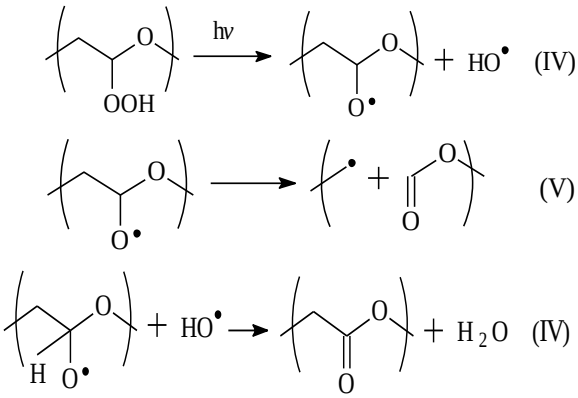

It is proposed that the scission of alkoxy radicals obtained in reaction (4) leads to the formation of formates (5), while in the radical disproportionation reaction (6) esters were obtained [3].

The kinetic parameters of thermal degradation of polyethylene oxide in the literature are related to the calculation of average values of activation energy E_A and the most probable models describing the process of degradation of PEO with different molecular weight [5–9], but there are no research articles on the effect of UV exposure and the use of additives to it.

The aim of the present work is to study the tensile and thermal properties, and kinetics of non-isothermal degradation of polyethylene oxide films containing cobalt (III) and iron (III) acetylacetonates under UV irradiation.

EXPERIMENTAL

Materials

The following materials were used for the preparation of the films: powdery polyethylene oxide (PEO), product of Neochim Co., Dimitrovgrad, Bulgaria, with melting temperature 68°C and molecular weight $M_V = 2.7\times10^6$; iron (III) acetylacetonate $Fe(acac)_3$ with chemical formula $Fe(C_5H_7O_2)_3$, melting temperature 180–182°C, molar weight 353.17 g/mol and density 5.24 g/cm^3 and cobalt (III) acetylacetonate $Co(acac)_3$ with chemical formula $Co(C_5H_7O_2)_3$, melting temperature 210–213°C, molar weight 356.26 g/mol and density 1.43 g/cm^3, products of Merck, Germany.

Sample Preparation

The initial PEO and the compositions containing 4 mmol/kg $Fe(acac)_3$ or $Co(acac)_3$ were homogenized in a laboratory mixer (MPW-802, Poland) at a rate of 10 s^{-1} for 15 min and then pressed in a laboratory press PHI (England) between aluminium foils. The conditions of films preparation were as follows: samples thickness about 200 μm, temperature 190°C, melting period 3 min at 190°C, pressing pressure 22 MPa for 1 min and cooling rate 40ºC/min.

UV exposure

The samples formed as 200 μm thick films were irradiated by UV light with wavelengths in the interval 185–254 nm emitted by 5 lamps of 8 W each, at room temperature for 1.5, 5, 10 and 90 hours.

Thermogravimetric measurements

The thermogravimetric analyses (TG-DTG-DSC) were carried out using a simultaneous thermal analyzer Netzsch STA 449 F3 Jupiter (Germany). Samples of about 4.6 ± 0.1 mg mass were used for the experiments at a hearing rate of 12.24°C/min up to 600°C in a flow of nitrogen at a rate of 10 cm^3/min under non-isothermal conditions. The samples were loaded without pressing in an open (6 mm diameter and 3 mm height) platinum crucible, without using a standard reference material. The degree of crystallinity of the samples was calculated at $\Delta H_{100\%}$ = 197 J/g for 100% crystalline PEO [10].

Tensile testing

The tensile strength and elongation at break of the initial PEO films and the PEO films containing 4 mmol/kg of the metal acetylacetonates mentioned above were measured on a dynamometer INSTRON 4203 (England) at room temperature and a speed of 50 mm/min.

RESULTS AND DISCUSSION

The process of destruction of polymer materials is related to deterioration of the mechanical properties such as strength and elongation at break. These properties are very sensitive to destruction and provide information on the degree of oxidation of the polymers. For this reason, the dependencies of the tensile strength and the elongation at break of the initial polyethylene oxide films and these containing 4 mmol/kg polymer of cobalt (III) and iron (III) acetylacetonate additives on irradiation duration with UV light were studied (Fig. 1). As can be seen from Fig. 1, the UV exposure for 5 hours had no significant effect on the strength of the initial PEO films. The use of $Fe(acac)_3$ and $Co(acac)_3$ simultaneously with the exposure reduced the tensile strength of the materials to 0.9 and 4.5 MPa, while for the initial PEO films this parameter was 8.4 MPa.

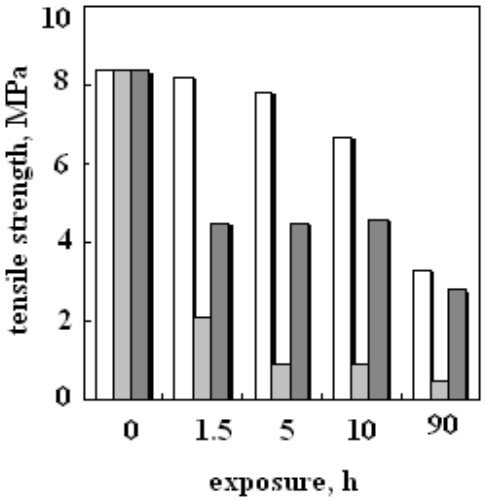

Fig. 1. Dependence of the tensile strength of foils of initial (□) PEO and materials based on it with $Fe(acac)_3$ (■) and $Co(acac)_3$ (■) at different exposure times

The change of the elongation at break follows the dependence of the tensile strength of the studied samples (Fig. 2). Upon exposure time of 1.5 hours, the elongation at break for the irradiated materials without additive decreased from 970% to 680%. The decrease of this parameter at the time of exposure was higher for the foils with additives – up to 30% for samples with $Co(acac)_3$

and up to 20% for samples with $Fe(acac)_3$. With increasing the duration of exposure to UV light the elongation at break and the tensile strength continued to decrease and at exposure time up to 90 hours the studied samples could not be tested because they became brittle and collapsed [11–13].

Table 1 shows the degree of crystallinity (α, %), temperatures of melting (T_m, °C) and crystallization (T_c, °C) of the PEO foils, as well as these with 4 mmol/kg additive $Fe(acac)_3$ or $Co(acac)_3$ before and after exposure to UV light for 1.5 and 5 hours. It can be seen that the temperatures of melting and crystallization of all tested samples of PEO with and without additives after irradiation remained almost unchanged and were in the range of 66.1–69.2°C and 143.3–146.8°C, respectively. It was found pot that the irradiation with UV light causes increase in the degree of crystallinity of PEO foils. The most noticeable increase in the degree of crystallinity (with

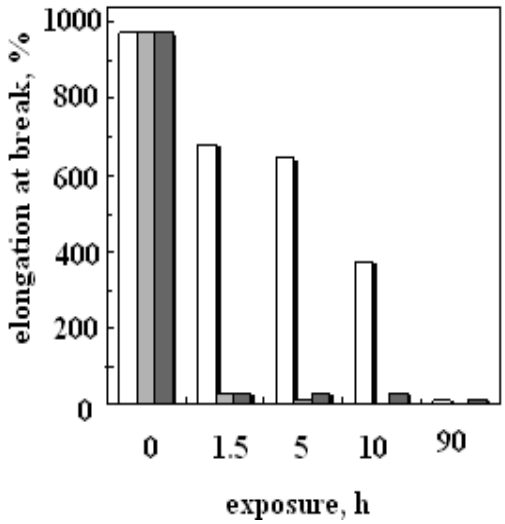

Fig. 2. Dependence of the elongation at break of foils initial (□) PEO and materials based on it with $Fe(acac)_3$ (■) and $Co(acac)_3$ (■) at different exposure times

Table 1. Characteristic temperatures of the initial PEO foils and irradiated materials based on it with and without additives at different exposure times [11–13]

Sample	T_m, °C	T_c, °C	$T_{initial}$, °C	T_{peak}, °C	T_{final}, °C	α, %
initial PEO						
Non-irradiated	67.8	143.3	259.7	400.1	490.8	69.9
Irradiated 1.5 hours	69.2	144.1	262.7	401.8	501.5	75.4
Irradiated 5 hours	68.1	145.1	272.1	401.7	501.9	81.6
PEO + 4 mmol/kg $Fe(acac)_3$						
Irradiated 1.5 hours	67.5	144.3	266.4	402.6	488.4	93.7
Irradiated 5 hours	66.1	144.8	292.2	402.5	485.2	94.3
PEO + 4 mmol/kg $Co(acac)_3$						
Irradiated 1.5 hours	68.1	145.2	287.0	401.7	492.0	77.1
Irradiated 5 hours	67.1	146.8	290.2	401.1	484.2	80.9

24.4% compared to that of the non-irradiated initial PEO films) was observed for the irradiated materials with iron (III) acetylacetonate.

The initial ($T_{initial}$), final (T_{final}) and peak (T_{peak}) temperatures of thermal degradation of the foils studied were determined from the TG (Fig. 3) and DTG curves and are shown in the same Table 1. It can be seen that for all of the samples tested $T_{initial}$ shifted towards higher temperature with the increase of irradiation times. For the non-irradiated PEO films it was 259.7°C and reached to 292.2°C for these containing iron (III) acetylacetonates under exposure time of 5 hours.

The T_{peak} value of the initial PEO foils was 400.1°C, almost the same as that reported by other authors [7, 8, 14]. Irradiation for 1.5 and 5 hours and the use of additives leads to increasing of T_{peak} to 402.6 and 401.7°C for the samples with $Fe(acac)_3$ or $Co(acac)_3$ irradiated 1.5 hours, respectively.

When comparing the T_{final} of the materials based on PEO containing additives, it was found that it was lower by ~ 6°C for these with $Fe(acac)_3$ and shifted towards higher temperatures for the irradiated foils with $Co(acac)_3$ (Fig. 3).

The kinetic parameters of the thermal degradation of the initial PEO foils and irradiated materials with and without additives in inert medium were determined by non-isothermal thermogravimetric analysis. The mathematical apparatus used was described earlier [11, 12].

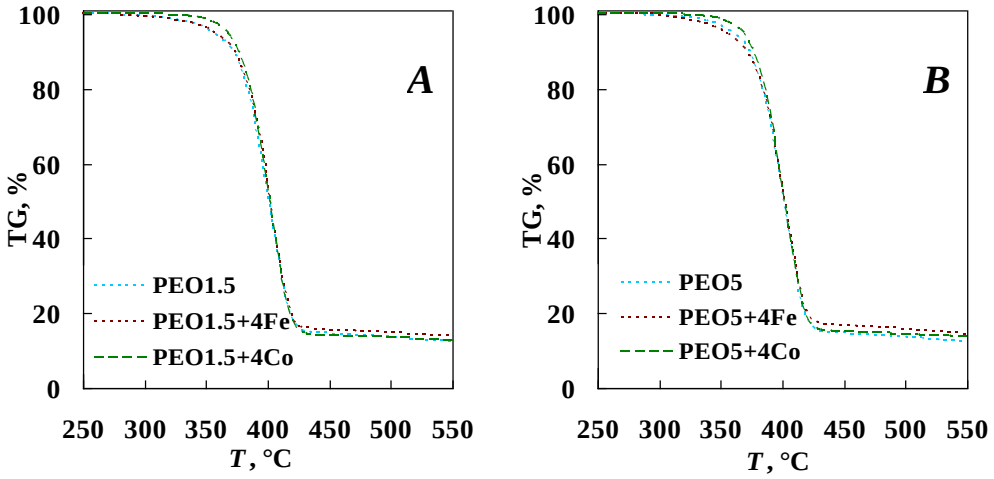

Fig. 3. TG curves of PEO foils and materials based on it with $Fe(acac)_3$ and $Co(acac)_3$ exposed to UV light for 1.5 h (*A*) and for 5 h (*B*)

The values of the activation energy E_A, the pre-exponential factor A and the most probable mechanism of the reactions were determined from the data of the TG curves by the linear form of the Coats-Redfern equation [15]

$$\ln\frac{g(\alpha)}{T^2} = \ln\frac{AR}{qE_A} - \frac{E_A}{RT} \qquad (1)$$

in the range of conversion degree α of 0.05 to 0.95. The dependence of $\ln[g(\alpha)/T^2]$ versus $1/T$ was plotted (not shown) using the mathematical expressions of each $g(\alpha)$ function [16]. The coefficient of determination R^2 and the value of E_A were used as a criterion for selection of the most probable mechanism function.

Table 2. Values of the reaction order n, activation energy E_A, pre-exponential factor A in the Arrhenius equation, change of enthalpy $\Delta H^{\neq}$, change of entropy $\Delta S^{\neq}$, and change of Gibbs free energy $\Delta G^{\neq}$ for PEO films [11–13]

Sample	n	E_A, kJ/mol	A, 1/min	R^2	ΔS, J/(mol.K)	ΔH, kJ/mol	ΔG, kJ/mol
initial PEO							
Non-irradiated	0.3405	164.45	1.27×10^{12}	0.9901	–62.34	158.85	200.82
Irradiated 1.5 hours	0.6207	191.90	1.32×10^{14}	0.9941	–23.75	186.29	202.32
Irradiated 5 hours	0.8624	221.58	1.18×10^{16}	0.9971	13.65	215.97	206.76
PEO + 4 mmol/kg $Fe(acac)_3$							
Irradiated 1.5 hours	0.3741	184.43	4.46×10^{13}	0.9960	–32.76	178.81	200.95
Irradiated 5 hours	1.8119	77.42	3.48×10^{5}	0.9788	–187.99	71.80	198.82
PEO + 4 mmol/kg $Co(acac)_3$							
Irradiated 1.5 hours	1.1541	276.81	4.15×10^{20}	1.0000	100.65	271.19	203.27
Irradiated 5 hours	1.2000	285.80	2.51×10^{21}	1.0000	115.62	280.20	202.24

The difference between the determination coefficients R^2 for the initial PEO foils and irradiated materials based on it with and without additives at different exposure times obtained by the D_2, D_3, D_4 or D_5 mechanism functions was insignificant (~0.003). At the same time the calculated value of E_A by the above mentioned mechanisms was inexplicably high. Thus, the F_n function was chosen as the most probable mechanism function for PEO films with and without additive in an amount of 4 mmol/kg PEO, exposed to UV light for 1.5 or 5 hours.

As can be seen from Table 2, the value of the reaction order n for non-irradiated sample of PEO was around 1/3 and increased in the sample irradiated for 5 hours. The addition of 4 mmol/kg PEO $Fe(acac)_3$ or $Co(acac)_3$ and exposure to UV light led to a notable change in the reaction order around 2 and 1.2, respectively, which corre-

sponds to a chemical process or mechanism of thermal degradation non-involving equations.

The values of the activation energy E_A and the pre-exponential factor A in the Arrhenius equation for the materials studied are presented in the same Table 2. For the initial PEO, E_A was within the range 140–185 kJ/mol as reported by Pielichowski and Flejtuch [7]. The activation energy of the irradiated samples of PEO and this containing cobalt (III) acetylacetonate was higher than that of non-irradiated foils. This is due to the fact that the exposure to UV light resulted in cross-linking of the polymer and therefore higher E_A [17]. Oppositely, the addition of iron (III) acetylacetonate and exposure time of 5 hours resulted in increased degradability of the foils and more than two times lower activation energy, namely 77.42 kJ/mol.

As can be seen from Table 2 the exposure of the PEO films to UV light resulted in the increase of the pre-exponential factor *A.* For the films containing 4 mmol $Co(acac)_3$ per kg PEO the increase of this kinetic parameter had 8–9 orders of magnitude higher value, i.e. the complex became more "loose" with increasing the irradiation time [16]. However, under exposure for 5 hours of the PEO films containing $Fe(acac)_3$ the pre-exponential factor had a seven orders of magnitude lower value.

The values of change of entropy $\Delta S^{\neq}$, change of enthalpy $\Delta H^{\neq}$ and change of Gibbs free energy $\Delta G^{\neq}$ (Table 2) for the formation of the activated complex of the PEO films studied were calculated at T_{peak}. The change of Gibbs free energy $\Delta G^{\neq}$ for the PEO films with and without additives had positive values, which indicates that the process of degradation of the studied materials was not spontaneous. The values of the change of enthalpy $\Delta H^{\neq}$ were also positive, i.e. the process of thermal degradation of the PEO films was connected with the introduction of heat. The need of heat introduction for thermal destruction of PEO foils with $Fe(acac)_3$ under 5 hours expo-sure was lower by 87 kJ/mol, while for the samples with cobalt (III) acetylacetonate it was higher by ~ 120 kJ/mol compared to that of initial PEO films (158.85 kJ/mol).

As can be seen from the Table 2, the values of the change of the entropy $\Delta S^{\neq}$ for the materials studied were negative or positive. When the $\Delta S^{\neq}$ was negative, it meant that the activated complex formed was more structured or "organized" than the initial reagents. The change of the entropy $\Delta S^{\neq}$ was positive for the samples of PEO irradiated 5 hours and these containing $Co(acac)_3$ irrespective on the duration of exposure. This meant that the formation of activated complex for these samples was with lower degree of arrangement than that of initial reagents, corresponding to a higher number of degrees of freedom in the Gibbs` phase rule. Therefore, it could be concluded that at the thermal degradation of polyethylene oxide films in an inert atmosphere two competing processes occurred: destruction and recombination.

Table 3. Values of the lifetime t_f of PEO films in the temperature range of 25 to 200°C [11–13]

Sample	Temperature, °C							
	25	50	75	100	125	150	175	200
initial PEO								
Non-irradiated	2.58×10^{15}	1.52×10^{13}	1.88×10^{11}	4.18×10^{9}	1.50×10^{8}	7.95×10^{6}	5.86×10^{5}	5.69×10^{4}
Irradiated 1.5 hours	1.61×10^{18}	4.04×10^{15}	2.40×10^{13}	2.82×10^{11}	5.80×10^{9}	1.89×10^{8}	9.00×10^{6}	5.92×10^{5}
Irradiated 5 hours	2.86×10^{21}	2.84×10^{18}	7.60×10^{15}	4.50×10^{13}	5.08×10^{11}	9.73×10^{9}	2.90×10^{8}	1.25×10^{7}
PEO + 4 mmol/kg $Fe(acac)_3$								
Irradiated 1.5 hours	2.32×10^{17}	7.34×10^{14}	5.31×10^{12}	7.43×10^{10}	1.78×10^{9}	6.61×10^{7}	3.55×10^{6}	2.60×10^{5}
Irradiated 5 hours	5.52×10^{6}	4.93×10^{5}	6.22×10^{4}	1.04×10^{4}	2.16×10^{3}	5.44×10^{2}	1.59×10^{2}	5.31×10^{1}
PEO + 4 mmol/kg $Co(acac)_3$								
Irradiated 1.5 hours	3.90×10^{26}	6.90×10^{22}	4.22×10^{19}	6.97×10^{16}	2.57×10^{14}	1.84×10^{12}	2.28×10^{10}	4.50×10^{8}
Irradiated 5 hours	2.43×10^{27}	3.25×10^{23}	1.56×10^{20}	2.10×10^{17}	6.44×10^{14}	3.92×10^{12}	4.22×10^{10}	7.34×10^{8}

The lifetime t_f of the PEO films was defined as the time when the mass loss reaches 5 mass% by equation [16]:

$$t_f = \frac{\left(1-0.95^{1-n}\right)}{A(1-n)}\exp\left(\frac{E_A}{RT}\right) \qquad (2).$$

As can be seen from Table 3, the lifetime of the PEO films in nitrogen atmosphere decreased with increasing the temperature from 25 to 200°C. The most stabile under irradiation were foils with cobalt (III) acetylacetonate, for which t_f was 2.43×10^{27}. In contrast, the same parameter for the films containing $Fe(acac)_3$ after 5 hours exposure had the lowest value 5.31×10^{1}. Therefore irradiation for 5 hours and the addition of iron (III) acetylacetonate accelerated the thermal degradation of polyethylene oxide foils.

CONCLUSIONS

The kinetic parameters of non-isothermal degradation of non-irradiated and irradiated polyethylene oxide films containing organic complexes of polyvalent metal acetylacetonates were determined using Coats-Redfern method. It was found that the exposure to UV light resulted in increase of activation energy compared to that of non-irradiated PEO foils with exception of foils with iron (III) acetylacetonate after 5 hours exposure for which the activation energy decreased to 77.42 kJ/mol. The most probable mechanism function of thermal degradation of PEO films with and without additives was F_n, where *n* had values between 1/3 and 2. It was found that the most stabile under irradiation were foils with cobalt (III) acetylacetonate, while these with iron (III) acetylacetonate after 5 hours irradiation accelerated the process of thermal degradation of polyethylene oxide foils.

REFERENCES

1. Fraisse, F., S. Morlat-Thérias, J.-L. Gardette, J.-M. Nedelec and M. Baba. *J. Phys. Chem. B*, **110**, (2006), p. 14678.
2. Koo, G.-H. and J. Jang. *J. Korean Soc. Dyers Finishers*, **21**, (2009), p. 16.
3. Claire, P. S. *Macromolecules*, **42**, (2009), p. 3469.
4. Zainuddin, J. Albinska, P. Ulański and J. M. Rosiak. *J. Radioanal. Nucl. Chem.*, **253**, (2002), p. 339.
5. Calahorra, E., M. Cortazar and G. M. Guzmán. *J. Polym. Sci. Pt. C - Polym. Lett. Ed*., 23, (1985), p. 257.
6. Wang, F.-Y., C.-C. M. Ma and W.-J. Wu. *J. Appl. Polym. Sci.*, **80**, (2001), p. 188.
7. Pielichowski, K. and K. Flejtuch. *J. Anal. Appl. Pyrolysis*, **73**, (2005), p. 131.
8. Vrandečić, N. S., M. Erceg, M. Jakić and I. Klarić. *Thermochim. Acta*, 498, (2010), p.71.
9. Erceg, M, J. Makrić and T. Kovačić. *ECCM14*, Budapest, Hungary, (2010), Paper ID: 245-ECCM145, p. 1.
10. Wunderlich, B. *Macromolecular physics, Vol. I, Crystal structure, morphology, defects,Academic press, New York, 1973*.
11. Tavlieva, M., D. Kiryakova and A. Atanassov. *Sci. Technol*., **6**, (2016), p. 20.
12. Tavlieva, M., D. Kiryakova and A. Atanassov. *Ind. Technol*., **3**, (2016), p. 210.
13. Tavlieva, M., D. Kiryakova and A. Atanassov. *Proceedings of University or Ruse*, **55**, (2016), p. 80.
14. Bizarria, M., M. Ávila and L. Mei. *Braz. J. Chem. Eng.*, **31**, (2014), p. 57.
15. Coats, A. W. and J. P. Redfern. *Nature*, **201**, (1964), p. 693.
16. Vlaev, L. T., V. G. Georgieva and M. P. Tavlieva. *On the kinetic mechanism of non-isothermal degradation of solids*, Eds. by Tiwari, A. and B. Raj, John Wiley & Sons, Hoboken, 2015, p. 547.
17. Doytcheva, M., D. Dotcheva, R. Stamenova, A. Orahovats, Ch. Tsvetanov and J. Leder. *J. Appl. Polym. Sci.*, **64**, (1997), p. 2299.

ANNUAL OF ASSEN ZLATAROV UNIVERSITY, BURGAS,
BULGARIA, 2017, v. XLVI (1)

SYNTHESIS OF DIBLOCK COPOLYMERS OF POLY(ALLYL GLYCIDYL ETHER) AND POLYGLYCIDOL

Miroslava Valchanova[1,2], Emilya Ivanova[2], Sevdalina Turmanova[2], Stanislav Rangelov[1]
E-mail: m.a.valchanova@abv.bg

[1] *Institute of Polymers, Bulgarian Academy of Sciences, Sofia 1113, Bulgaria*
[2] *Department of Materials Science, Prof. Assen Zlatarov University, Burgas 8010, Bulgaria*

ABSTRACT

Novel diblock copolymers of poly(allyl glycidyl ether) and polyglycidol a containing hydrophobic residue were synthesized. First, poly(allyl glycidyl ether) was synthesized by ring-opening anionic polymerization of allyl glycidyl ether initiated by sodium dodecanoate. In the second stage, poly(allyl glycidyl ether) was used to initiate ring-opening anionic polymerization of ethoxyethylene glycidyl ether (protected glycidol), which gave a series of diblock copolymers with various ratios between the two blocks. After releasing the protective groups, a series of diblock copolymers of the type poly(allyl glycidyl ether)-b-polyglycidol containing a hydrophobic dodecyl residue were obtained. The copolymers were characterized by various structural methods of analysis.

Key words: *diblock copolymers, ring-opening anionic polymerization, poly(allyl glycidyl ether), polyglycidol*

INTRODUCTION

Contemporary science exhibits great interest in the creation of new synthetic polymer materials of predetermined composition and properties. They are the basis of a versatile class of polymers of special scientific importance with their different biomedical applications and possibilities to control their composition, structure and, hence, properties. Beside the classical methods of *living* anionic and cationic polymerizations, new methods of controlled polymerization have been developed in recent decades, such as the atom transfer radical polymerization (ATRP) [1], nitroxide–mediated polymerization (NMP) [2], reversible addition–fragmentation chain–transfer polymerization (RAFT) [3, 4], and ring-opening metathesis polymerization (ROMP) [5,6]. The most important achievement of the methods of controlled polymerization is the opportunity to synthesize specially designed co-polymers with certain macromolecular structure, chemical composition, functionality, low dispersity and heterogeneity.

Various amphiphilic block copolymers with different chain architecture, topology, and functionality can be synthesized by controlled polymerization processes. They have a great potential for creation of supramolecular nanoparticles with preliminarily designed properties. The controlled synthesis of new functional polymers is of crucial importance for the preparation of polymer carriers of drugs and biologically active substances.

Diblock copolymers have linear chain architecture. The typically used blocks can be entirely hydrophilic, entirely hydrophobic or sensitive to external stimuli, such as temperature, pH, etc., under which they can undergo transitions from soluble to insoluble states.

The scientific interest in polyglycidols as a class of highly functional polymers is on account of their flexible hydrophilic chain, which in many aspects is similar to that of polyethylene glycols, but is functionalized with a hydroxymethylene group at each monomer unit. Various approaches to the synthesis of branched and linear polyglycidols as well as their copolymers have been reported in the scientific literature. The reports show that polyglycidols are suitable precursors for the synthesis of various amphiphilic copolymers. In a number of papers, *Rangelov et al.* have reported the preparation of series of well-defined triblock copolymers polygly-cidol-poly(propylene oxide)-polyglycidol with varying content of polyglycidol and fixed molar mass of

the block of poly(propylene oxide) [7-13]. These copolymers can be considered analogous to the copolymers of the *Pluronic* trade mark, in which the polyoxyethylene blocks are substituted by blocks of polyglycidol.

The present paper reports on the synthesis of novel diblock copolymers of poly(allyl glycidyl ether) and polyglycidol by ring-opening anionic polymerization. The novel copolymers bear a hydrophobic dodecyl residue and have a latent chemical functionality: a double bond and a hydro-xymethylene group at each monomer unit of the poly(allyl glycidyl ether) and polyglycidol blocks, respectively, which provides versatile possibilities for further chemical modification.

EXPERIMENTAL

Materials and reagents

All solvents (methanol, dichloromethane, tetrahydrofuran) as well as the ethyl vinyl ether (99%, Aldrich) were purified by distillation. The allyl glycidyl ether (99% Fluka) and glycidol (96% Aldrich) were distilled at reduced pressure. The other substances used were HCI (32% Aldrich), KOH, benzene, toluene sulfonic acid, $AlCl_3$. $6H_2O$ (Merck). The ethoxyethyl glycidyl ether (EEGE) was prepared by a reaction of glycidol with ethyl vinyl ether as described elsewhere [14].

Synthesis of macroinitiator poly(allyl glycidyl ether) (PAGE)

In a glass reactor equipped with magnetic stirrer, 0.18 g (3.21×10^{-3}mol) of KOH and 1.0056 g (5.39×10^{-3}mol) of 1-dodecanol were placed and heated to 50°C for 2 h in inert medium. After cooling the reaction mixture to room temperature, 1.0 ml of dry benzene was added to the mixture and the system was vacuumed for 2 h to remove the water released by the reaction. The procedure was repeated several times for full removal of the water. Then the temperature was raised to 70°C and 30.60 g (0.269 mol) of AGE were added. The polymerization proceeded at 70°C for 24 h in an inert medium. The polymerization was stopped by adding of 3.0 ml of methanol. Then the water layer was neutralized with 15.0 ml of methanol and 5.0 ml of HCl and the product was dried in vacuum. The PAGE yield was ~ 9.5 g.

Synthesis of diblock copolymer by controlled polymerization with opening of the EEGE ring

To 2 g (17.54×10^{-3} mol) of PAGE placed in a glass reactor equipped with magnetic stirrer and reflux condenser, (0.016 g, 0.022 g or 0.032 g,) of KOH were added and the mixture was heated to 50°C for 2 h**.** After cooling the reaction mixture to room temperature, 1.0 ml of dry benzene were added to the mixture and the system was vacuumed for 2 h to remove the water released by the reaction. The procedure was repeated several times until full removal of the released water and then the temperature was raised to 90°C. Different amounts (0.993 g, 2.686 g, 6.132 g) of EEGE were added at portions. The polymerization reaction proceeded at 90°C in an inert medium until the whole amount of monomer was consumed, which was monitored by ^{1}H NMR. The reaction was stopped by adding a mixture of methanol and dichloromethane. After neutralization with methanol and HCl, the copolymers were dissolved in tetrahydrofuran and the dispersions were centrifuged to remove the salt formed by the neutralization. The solvent was then removed and the copolymers were dried in a vacuum desiccator at room temperature until constant weight.

Removal of the ethoxyethylene protective groups

To a certain amount of PAGE-*b*-PEEGE copolymer, $AlCl_3.6H_2O$ and CH_3OH were added in mole ratio EEGE:$AlCl_3.6H_2O$:CH_3OH 100:1:800 and the mixture was stirred for 1 h at 25°C. The reaction product was then filtered through Hylfo Super gel (Diatomic earth) and the solvent was removed under reduced pressure.

Analyses

Nuclear magnetic resonance (NMR)

The ^{1}H NMR spectra of the samples analyzed were registered on a Bruker (Germany), Avance II, 600 MHz apparatus in deuterated chloroform ($CDCl_3$) or dimethyl sulfoxide (DMSO-d_6). The internal standard used was tetramethylsilane.

Gel-permeation chromatography (GPC)

The relative molecular weights of the copolymers and their molecular mass distribution were determined on a Wyatt apparatus, equipped with two PL gel MIXED-C columns and one 100 Å PSS GRAM column with DMF as an eluent at 40°C. The flow rate was 1 ml/min. The system was calibrated with styrene standards.

RESULTS AND DISCUSSION

A series of three diblock copolymers PAGE-*b*-*PG* bearing a hydrophobic dodecyl residue were synthesized by sequential ring-opening anionic polymerization of AGE and EEGE followed by removal of the protective groups. In the first stage, illustrated in Scheme 1, the polymerization of AGE was initiated by partially deprotonated dodecanol. The polymerization proceeded in absence of organic solvent at 70°C for 24 h, which appeared to be the optimal conditions. The polymer obtained was characterized by ^{1}H NMR and GPC (Figs. 1 and 2).

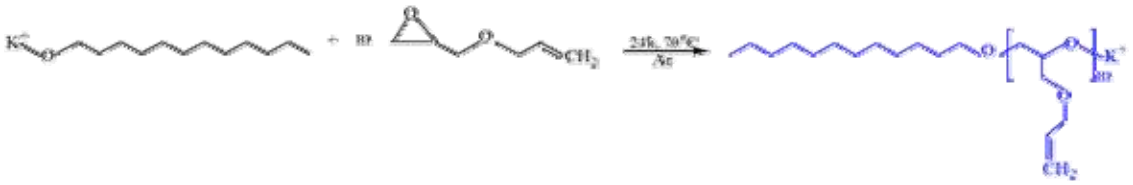

Scheme 1. Preparation of poly(allyl glycidyl ether) by ring-opening anionic polymerization the AGE, initiated by partially deprotonated dodecanol.

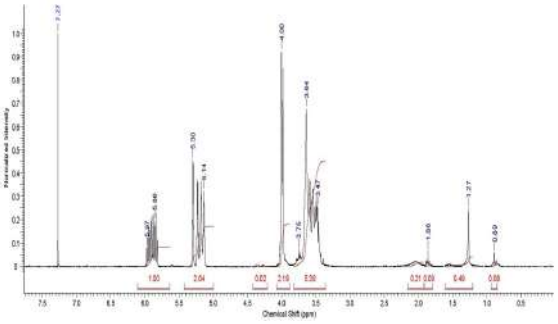

Fig. 1. ^{1}H NMR spectrum of PAGE in $CDCl_3$.

Fig. 1 shows the ^{1}H NMR spectrum of PAGE, from which the number average molecular weight was determined: M_n = 4900, corresponding to a degree of polymerization DP = 44. The gel permeation chromatography gave the number average and weight average molecular weights of the PAGE precursor of 6630 and 7530, respectively (Fig. 2).

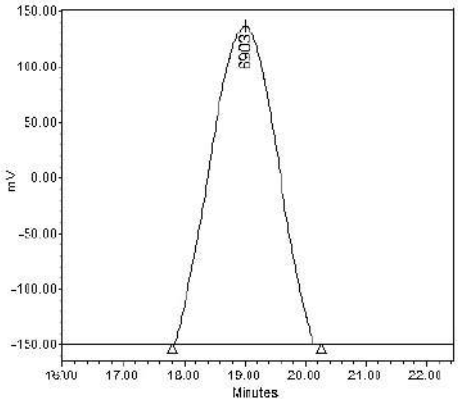

Fig. 2. Gel permeation chromatogram of PAGE.

The data obtained from the GPC analysis indicated a narrow molecular weight distribution with a dispersity index M_w/M_n=1.14.

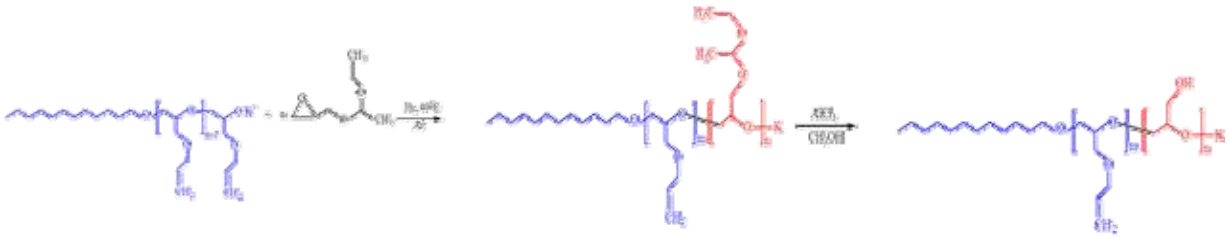

Scheme 2. Preparation of diblock copolymer PAGE-*b*-PG with hydrophobic dodecyl residue.

The PAGE synthesized and characterized in the first stage was used as a macroinitiator for polymerization of EEGE (protected glycidol). The reaction scheme including the final stage of removal of the protective ethoxyethyl groups and the formation of a block of PG is presented in Scheme 2.

A representative gel permeation chromatogram of the PAGE-*b*-PEEGE copolymer is shown in Fig. 3. The shift of the curve to the lower elution times compared to that of the initial PAGE, shown in Fig. 2, indicated for the successful polymerization and formation of a second block of PEEGE.

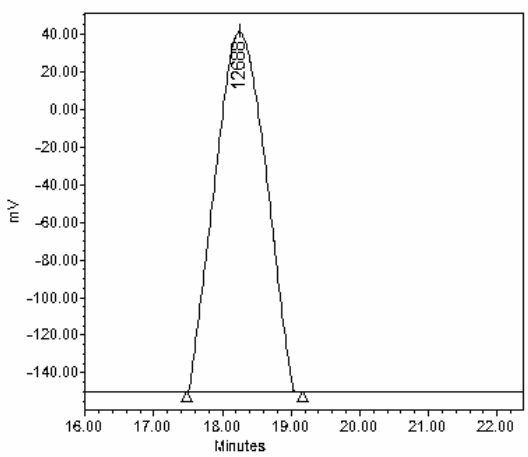

Fig. 3. Gel permeation chromatogram of PAGE-b-PEEGE.

The ^{1}H NMR spectra of the precursor PAGE-*b*-PEEGE and its corresponding copolymer after the removal of the protective groups are presented in Figs. 4 and 5. The disappearance of the signals for the methine proton at 4.6 – 4.7 ppm and the methyl protons at 1.1-1.2 and 1.3 ppm characteristic for the acetal group prove the transformation of the PEEGE block into PG block. The results obtained from the two analyses are summarized in Table 1.

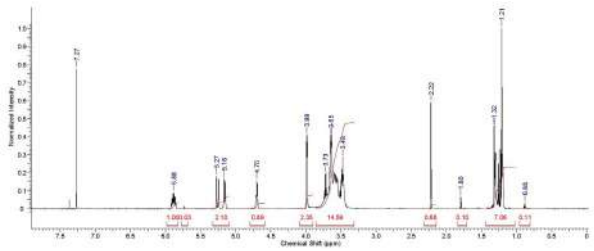

Fig. 4. ^{1}H NMR spectrum in $CDCl_3$ of PAGE-*b*-PEEGE.

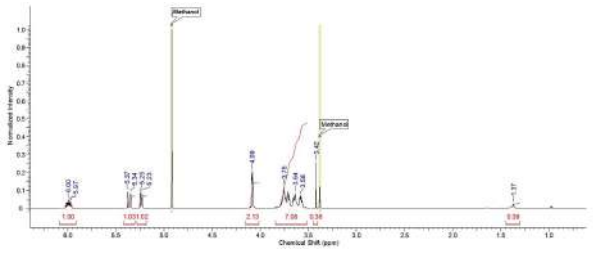

Fig. 5. ^{1}H NMR spectrum in $CDCl_3$ of PAGE-*b*-PG.

Table 1. Molecular mass and characterizing parameters of PAGE-*b*-PEEGE and PAGE-*b*-PG diblock copolymers determined by GPC and ^{1}H NMR. a – determined by GPC; b – determined by ^{1}H NMR

M_n (PAGE-*b*-PEEGE)[a]	DP of the block from PEEGE[a]	PG mol %[b]
7200	16	25
10600	39	50
19200	98	70

CONCLUSION

Using ring-opening anionic polymerization, a series of diblock copolymers PAGE-*b*-PG containing allyl and hydroxyl functional groups at each monomer unit of the corresponding block were synthesized. The copolymers contained a hydrophobic residue at the end of the chain. They were of fixed molar mass of the PAGE block (Mn=4900) corresponding to degree of polymerization of 44 and increasing content of polyglycidol (25, 50 and 70 mol %) corresponding to degrees of polymerization of 16, 39 and 98, respectively.

REFERENCES

1. Braunecker, W. and K. Matyjaszewski. *Prog. Polym. Sci.,* 32, (2007), p. 93.
2. Hawker, C., A. Bosman and E. Harth. *Chem. Rev*., 101, (2001), p. 3661.
3. Destarac, M. *Polym. Rev*., 51, (2011), p. 163.
4. Moad, G., E. Rizzardo and S. Thang. *Aust. J. Chem.,* 65, (2012), p. 985.
5. Trnka, T. and R. Grubbs. *Acc. Chem. Res*., 34, (2001), p. 18.
6. Coates, G. *Chem. Rev*., 100, (2000), p. 1223.
7. Halacheva, S., S. Rangelov and Ch. Tsvetanov. *Macromolecules,* 39, (2006), p. 6845.
8. Rangelov, S., M. Almgren, S. Halacheva and Ch. Tsvetanov. *J. Phys. Chem. C*, 111, (2007), p. 13185.
9. Halacheva, S., S. Rangelov and V. Garamus. *Macromolecules*, 40, (2007), p. 8015.

10. Halacheva, S., S. Rangelov and Ch. Tsvetanov. *J. Phys. Chem. B*, 112, (2008), p. 1899.
11. Halacheva, S., S. Rangelov and Ch. Tsvetanov. *Macromolecules,* 41, (2008), p.7699.
12. Rangelov, S., S. Halacheva, V. Garamus and M. Almgren. *Macromolecules,* 22, (2008), p. 8885.
13. Halacheva, S., S. Rangelov, Ch. Tsvetanov; V. Garamus, *Macromolecules,* 43, (2010), p. 772.
14. Fitton, A., J. Hill, D. Jane and R. Miller. *Synthesis*, (1987), p. 1140.

ANNUAL OF ASSEN ZLATAROV UNIVERSITY, BURGAS
BULGARIA, 2017, v. XLVI (1)

REACTION KINETICS OF BUTYL ACETATE SYNTHESIS IN THE PRESENCE OF PYRIDINIUM-BASED ACIDIC IONIC LIQUIDS

Ivaylo Tankov, Magdalena Mitkova, Dicho Stratiev
E-mail: igtankov@yahoo.com

ABSTRACT

The reaction kinetics of acetic acid esterification with butanol to butyl acetate using pyridinium-based acidic ionic liquids as homogeneous catalysts is investigated in an isothermal batch reactor. The second order pseudo-homogeneous kinetic model is developed from the reaction mechanism. It is established that the model predictions and experimental results are in a good agreement. The influence of the process parameters temperature (343, 353 and 363 K), initial molar ratio butanol-to-acetic acid (1, 3, 5 and 7) and catalyst loading (5, 10 and 15 mass.%) on the reaction kinetic constant is also investigated. It is found out that the kinetic constant value increases with reaction temperature due to the exothermic nature of the esterification process. The activation energy and pre-exponential factor are determined from the Arrhenius plot. The increase of both catalyst concentration and initial reactants molar ratio leads to higher values of acetic acid conversion and favours the esterification rate.

Key words: *reaction kinetics, ionic liquids, esterification, butyl acetate*

INTRODUCTION

Butyl acetate is an important organic solvent which can dissolve ethylcellulose, cellulose acetate butyrate, polystyrene, and kinds of natural gum.

The industrial process for butyl acetate production is the esterification of acetic acid and 1-butanol catalyzed by mineral acids such as H_2SO_4, H_3PO_4, HNO_3, HCl due to their high activity and stability [1]. However, the strong corrosion effect of these catalysts on the chemical equipment and hard isolation of the reaction products are the purpose for numerous heterogeneous catalysts such as heteropoly acids [2], molecular sieves [3], resins [4] and supported metal oxides [5, 6] to be studied in the esterification processes.

In recent years, acetic acid esterification in the presence of acidic ionic liquids (ILs) as environmentally friendly catalysts has attracted much attention [7, 8] because of their non-corrosiveness, negligible volatility and excellent thermal stability [9].

Fraga-Dubreuil and co-workers [7] describe the reaction of acetic acid with C_5–C_7 alcohols using ionic liquids (l-butyl-3-methylimidazol, l-hexyl-3-methylimidazol) containing hydrogen sulphate anion. Similar to the imidazolium, in the area of organic synthesis pyridinium-based ionic liquids can also be used as catalysts. For example, the production of 2,3-disubstituted quinolines via one-pot three-component reaction of arylamines, arylaldehydes and aliphatic aldehydes is highly improved by adding of butylpyridinium tetrachloroindate-(III) [10]. Aupoix et al. [11] have found that N-alkyl-pyridinium trifluoromethane sulfonate catalyzed the benzoin condensation giving good yields within short reaction time using solvent-free microwave activation conditions.

Taking into account that the esterification is a slow-rate and highly reversible reaction, the chemical equilibrium influences the conversion of the reactants [12, 13]. In order to reach a maximum conversion of the reagent during the esterification process, some approaches are proposed: (*i*) using alcohol in a large excess and/or (*ii*) physical separation of water, mainly by means of a distillation procedure.

Considering that the design of a chemical reactor is based on the reaction rate equation, for optimization of a given industrial process, the reaction kinetics should be well determined. Generally, the appropriate rate equation depends on the reaction mechanism, including the elementary steps of the primary and side reactions.

Considering the research papers related to the esterification reactions, only little information about the kinetics of acetic acid esterification using pyridinium-based acidic ionic liquids can be found. Thereby, the reaction kinetics of butyl acetate synthesis in the presence of pyridinium-based acidic ionic liquids is investigated in the current paper.

EXPERIMENT

1. Catalysts preparation

The preparation procedure of pyridinium hydrogen sulphate involves a dropwise addition of equimolar (with respect to pyridine) sulphuric acid to an aqueous solution (5 mass./mass.%) of pyridine over a period of 1.5 h under vigorous stirring. The aqueous solution of pyridinium hydrogen sulphate is distilled at 333 K and reduced pressure (0.085 MPa). The resulted colourless solid product ($[H–Pyr]^+[HSO_4]^-$) is dried until the weight of the residue remains constant. Then, $[H–Pyr]^+[HSO_4]^-$ is washed with diethyl ether (0.100 L) three times and dried in vacuum (0.050 MPa) at 353 K for 12 h. The synthesis procedure of the ionic liquids $[H–Pyr]^+[H_2PO_4]^-$ and $[H–Pyr]^+[NO_3]^-$ does not differ from the one described for $[H–Pyr]^+[HSO_4]^-$.

2. Apparatus

The catalytic experiments are carried out in a three-neck round bottom flask of 0.250 L capacity, equipped with a condenser, a Dean-Stark trap, a port for sample withdrawal and a thermometer.

Mixing of the reaction fluid is performed by a magnetic stirrer. In a typical procedure for esterification, acetic acid (0.2778 mol), ionic liquid (5, 10 or 15 mass.% with respect to the mass of acetic acid) and inert solvent (hexane, cyclohexane or heptane) for water removal in the form of azeotrope mixture are placed in the reactor. Once the desired reaction temperature (343, 353 and 363 K) is obtained, a known quantity of butanol (0.2778, 0.8834, 1.3890 and 1.9446 mol to reach a butanol-to-acetic acid molar ratio (*M*) of 1, 3, 5 and 7, respectively), separately heated to the set temperature is added into the reactor. This time is considered as zero reaction time (t = 0). The total reaction time for the kinetic experiment is 70 min.

$$X_A = \frac{C_{A_0} - C_A}{C_{A_0}} \quad (1)$$

where, X_A is acetic acid conversion (%); C_{A0} is initial acetic acid concentration (mol L^{-1}) and C_A is acetic acid concentration (mol L^{-1}) at time t (min). The reaction progress at given reaction time is monitored by measuring the water content in continuously distilled azeotrope mixture during the reaction. In order to confirm the reaction progress, GC analysis is carried out. For this purpose, at regular intervals of time (10 min) samples (1 ml) are withdrawn and immediately cooled in an ice bath. The acetic acid concentration is analyzed by GC 7890A (Agilent Technologies), equipped with a flame ionization detector and capillary column HP-INNOWAX, 30 m × 0.32 mm × 0.25μm. High purity helium at a flow rate of 0.0015 L min^{-1} is used as a carrier gas. The analytical uncertainty of GC is less than 3%, which is in accordance with the acceptable limits. The acetic acid conversion is calculated according to Eq. (1).

3. Kinetic models

The esterification of acetic acid with butanol (Sheme 1) in the presence of $[H–Pyr]^+[HSO_4]^-$, $[H–Pyr]^+[H_2PO_4]^-$ and $[H–Pyr]^+[NO_3]^-$ catalysts is proposed as second-order reversible reaction. Based on it, two pseudo-homogeneous kinetic models are presented. The first one is used to fit the experimental data in cases where M is 3, 5 and 7. The second kinetic model is used when the reactants (acetic acid and butanol) are taken in stoichiometric amounts (M = 1).

$$A + Y \overset{k_1}{\rightarrow} B + Z$$
$$Z + B \overset{k_2}{\rightarrow} Y + A$$

Scheme 1. Esterification of acetic acid with butanol. *A*, *Y*, *B* and *Z* are acetic acid, butanol, butyl acetate and water, respectively. k_1 and k_2 are rate constants of forward and backward reaction, respectively.

3.1. Kinetic model at $M \neq 1$ ($C_{A_0} \neq C_{Y_0}$)

Since the acetic acid esterification with butanol is proposed as a second-order reversible reaction (Scheme 1), the rate equation can be represented as:

$$-r_A = -\frac{dC_A}{dt} = k_1 C_A C_Y - k_2 C_B C_Z \quad (2)$$

where, C_A, C_Y, C_B and C_Z describe the concentration (mol L^{-1}) of acetic acid, butanol, ester and water at reaction time t (min), respectively.

The proposed kinetic model is based on the following limitations: (*i*). Assuming that the reaction products (*B* and *Z*) are not present in the initial reaction mixture, their concentrations (C_{B_0}, C_{Z_0}) at t = 0 are equal to zero.

Therefore, with respect to the acetic acid conversion, C_A, C_Y, C_B and C_Z can be written as:

$$C_A = C_{A_0}(1 - X_A) \quad (3)$$
$$C_A = C_{A_0}(1 - X_A) \quad (4)$$
$$C_B = C_Z = C_{A_0} X_A \quad (5)$$

(*ii*). Since the esterification of acetic acid with butanol is conducted via a reactive distillation process (expressed by continuous removal of water in the form of azeotrope), it was suggested that at any time of the reaction the concentration of water (C_Z) in the reaction zone is zero. Consequently, the second member of the right hand side ($k_2 C_B C_Z$) of the Eq. (2) can be neglected. Hence, after rearranging of the variables and integration, Eq. (2) becomes as follows:

$$\frac{1}{C_{A_0}(M-1)}\left[\ln\frac{M - X_A}{M(1 - X_A)}\right] = k_1 t \quad (6)$$

The plot of $\frac{1}{C_{A_0}(M-1)}\left[\ln\frac{M-X_A}{M(1-X_A)}\right]$ versus time (*t*) is a straight line passing through the origin. The slope of the line represents the kinetic constant value. Equation (6) is used to fit the experimental data obtained at $M = 3$ for different reaction temperatures, various catalysts and several catalyst concentrations.

3.2. Kinetic model at M = 1 ($C_{A_0} = C_{Y_0}$)

Taking into account the above-mentioned limitations, in Eq. (3) with conditions $C_{A_0} = C_{Y_0}$ and $C_{B_0} = C_{Z_0} = C_Z = 0$, the rate of expression is:

$$\frac{1}{C_{A_0}}\left(\frac{X_A}{1 - X_A}\right) = k_1 t \quad (7)$$

Similar to the kinetic model for $M \neq 1$ (Eq. (6)), the plot of $\frac{1}{C_{A_0}}\left(\frac{X_A}{1-X_A}\right)$ versus *t* is a straight line passing through the origin. The kinetic constant value is represented by the line slope.

RESULTS AND DISCUSSION

1 Catalyst Performance

The esterification of butanol with acetic acid in the presence of different acidic ILs as catalysts is conducted for testing the reaction kinetics at 363 K, an alcohol-to-acid molar ratio of 3 and catalyst loading of 10 mass.% (Fig. 1A and B).

It is known that the esterification of carboxylic acids proceed via formation of active carbonyl complex (pronated acid) as a consequence of an interaction between the carboxylic acid and catalyst [14]. Since the extent of catalyst acidity correlates to the number of above-mentioned active complexes, it could be assumed that the concentration of pronated acid depends on the catalyst capacity to produce hydrogen cations [15].

Taking into account that the cation ($[H–Pyr]^+$) in all samples does not differ, X_A should depend mainly on the anion nature. Based on the latter, it is expected that the highest values of X_A can be reached when $[H–Pyr]^+[H_2PO_4]^-$ is used as a catalyst. In contrast, $[H–Pyr]^+[NO_3]^-$ catalyst should possess the lowest activity.

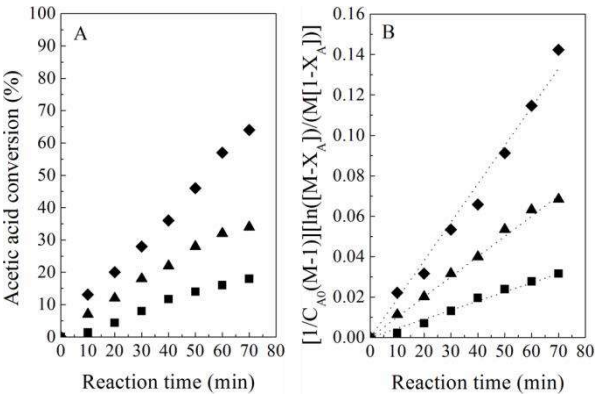

Fig. 1. Influence of different catalysts on the acetic acid conversion **(A)** and the kinetic constant value **(B)** with time: $[H–Pyr]^+[HSO_4]^-$ (◆), $[H–Pyr]^+[H_2PO_4]^-$ (▲), $[H–Pyr]^+[NO_3]^-$ (■), kinetic model (----). *T* – 363 K, *M* – 3, catalyst loading – 10 mass.%, *t* – 70 min.

The results show that a maximum X_A value of 64% is obtained when $[H–Pyr]^+[HSO_4]^-$ is used as a catalyst (Fig. 1A). In the cases where the esterification process is conducted in the presence of $[H–Pyr]^+[H_2PO_4]^-$ and $[H–Pyr]^+[NO_3]^-$ catalysts, the acetic acid conversion reaches 37 and 19%, respectively.

The dissimilarity between the experimental data and proposed catalytic activity of $[H–Pyr]^+[HSO_4]^-$ and $[H–Pyr]^+[H_2PO_4]^-$ samples could be explained on the basis of the electronic effects in anions $[HSO_4]^-$ and $[H_2PO_4]^-$. The structure of the hydrogen sulphate anion ($[(HO)SO_3]^-$) contains three oxygen atoms, which are not attached to hydrogen atoms (in the form of HO^- group). Due to the high electronegativity of the oxygen atom [16, 17], the electron density is drawn toward those atoms by an induc-

tive effect. As a result, the electron density on the sulphur atom decreases and a slight positive charge ($S^{\delta+}$) is formed. The latter is partially compensated by shifting the electron density from the O–H bond, which increases its polarity. Thus, the O–H bond becomes more suitable for cleavage to proton (H^+). In contrary to $[(HO)SO_3]^-$, dihydrogen phosphate anion ($[(HO)_2PO_2]^-$) possesses two oxygen atoms, unbounded to hydrogen atoms. Consequently, it could be expected that the polarization of OH groups in $[(HO)_2PO_2]^-$ will be less pronounced than that in $(HO)SO_3]^-$.

Based on the observed electronic effects in the anions $[HSO_4]^-$ and $[H_2PO_4]^-$, it could be concluded that a greater number of hydrogen cations during the esterification may generate $[H–Pyr]^+[HSO_4]^-$ sample in comparison with $[H–Pyr]^+[H_2PO_4]^-$ one.

Kinetic constant (k_1) values of the esterification reaction conducted in the presence of different catalysts are estimated by plotting the left hand side of Eq. (6) versus *t* (Fig. 1B). It is found out that the proposed kinetic model fits the experimental data well. The calculated kinetic constant values for $[H–Pyr]^+[HSO_4]^-$, $[H–Pyr]^+[H_2PO_4]^-$ and $[H–Pyr]^+[NO_3]^-$ at given reaction conditions are 19.38 ± 2.53 (L $mol^{-1}min^{-1}$, × 10^{-4}); 10.12 ± 0.83 (L $mol^{-1}min^{-1}$, × 10^{-4}) and 5.28 ± 0.59 (L $mol^{-1}min^{-1}$, × 10^{-4}), respectively. Since the $[H–Pyr]^+[HSO_4]^-$ sample possess the highest catalytic activity, it is preferred for further studies.

2. Effect of catalyst loading

The effect of $[H–Pyr]^+[HSO_4]^-$ catalyst loading on the conversion value of acetic acid to butyl acetate is studied with respect to time (Fig. 2A and B). The acetic acid conversion during the non-catalytic (blank) reaction is also included.

The amount of the catalyst plays a major role in the conversion of carboxylic acid to ester via esterification. At the start of an esterification process the concentration of the carboxylic acid is high which leads to a clearly pronounced interaction between the acid and catalyst. However, during the reaction progress, the acid concentration decreases which results in a poorer acid–catalyst interaction. Therefore, for increasing the overall conversion the amount of catalyst plays a crucial role.

The results show that after 70 minutes reaction time the value of acetic acid conversion during esterification in the absence of catalyst (blank reaction) is 7%. The conversion value increases proportionally to the catalyst loading.

When catalyst loading increases from 5 to 15 mass.%, X_A changes from 46 to 93%. Feijt et al. [18] study the esterification of myristic acid with propanol using *p*-toluene sulphonic acid as catalyst and show that the increasing of catalyst loading enhances the number of H^+ ions available for acid activation. Thus, higher conversion value (93%) at catalyst loading of 15 wt.% with respect to the conversion value (46%) at catalyst loading of 5 wt.% is related to a greater number of active carbonyl complexes.

Plotting the left hand side of Eq. (6) versus *t* allows determination of kinetic constant values at different catalyst loading (Fig. 2B). Thus, the rate constant values of 2.12 ± 0.14 (L $mol^{-1}min^{-1}$, × 10^{-4}); 13.18 ± 0.98 (L $mol^{-1}min^{-1}$, × 10^{-4}); 19.38 ± 2.53 (L $mol^{-1}min^{-1}$, × 10^{-4}) and 47.31 ± 3.11 (L $mol^{-1}min^{-1}$, × 10^{-4}) are obtained for blank (non-catalyzed) reaction and the esterification carried out using 5, 10 and 15 mass.% $[H–Pyr]^+[HSO_4]^-$ catalyst, respectively.

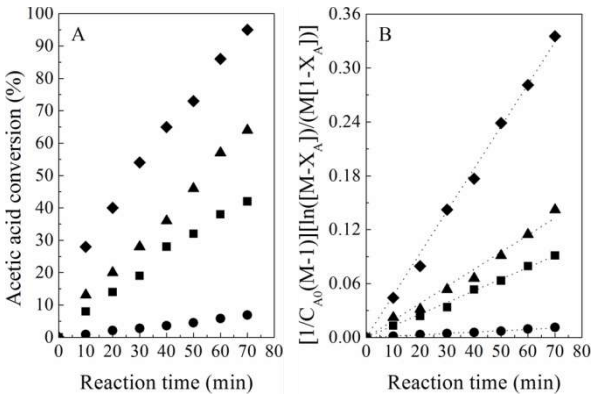

Fig. 2. Effect of $[H–Pyr]^+[HSO_4]^-$ catalyst loading on the acetic acid conversion **(A)** and the kinetic constant value **(B)** with time: 15 mass.% (◆), 10 mass.% (▲), 5 mass.% (■), blank reaction (●), kinetic model (----). *T* – 363 K, *M* – 3, *t* – 70 min.

3. Effect of initial reactants molar ratio

The alteration of acetic acid conversion as a function of molar ratio of butanol-to-acetic acid is established at temperature of 363 K and catalyst loading of 10 mass.% (Fig. 3A and B). The experimental data indicate that the acetic acid conversion to ester is significantly affected by the *M* value. The variation of molar ratio value from 1 to 3 strongly increases the conversion of acetic acid from 33 to 68% (Fig. 3A). It is established that at *M* = 5 the acetic acid conversion

reached its maximum value (73%). At initial reactant molar ratio of 7 the acid conversion value of 67% is registered. The increasing of the acetic acid conversion with reactant molar ratio is not surprising, considering the fact that the high reactants concentration shifts the reaction equilibrium toward the left side of stoichiometry equation.

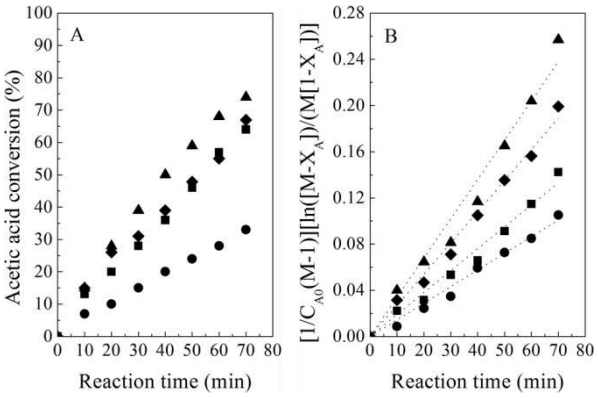

Fig. 3. Effect of initial molar ratio (*M*) butanol-to-acetic acid on the acetic acid conversion **(A)** and the kinetic constant value **(B)** with time: *M* = 1 (●), *M* = 3 (◆), *M* = 5 (▲), *M* = 7 (■), kinetic model (----). *T* – 363 K, catalyst loading – 10 mass.%, *t* – 70 min.

However, the decreasing of the X_A value from 73 to 67% during the *M* alteration from 5 to 7 suggests that a critical value of acetic acid concentration is achieved. At those *M* values, the acetic acid concentration is changed from 1.5476 to 1.2057 mol L^{-1}. Above a critical value of butanol concentration (in the present work it varies from 7.7381 to 8.4401 mol L^{-1} for *M* = 5 and *M* = 7, respectively), a decreasing in overall acetic acid conversion due to a dilution effect is observed. The influence of molar ratio of reactants on the rate constant with time is investigated by means of Eqs. (6) and (7). The results show that the kinetic constant values depend on the reactants molar ratio (Fig. 3B). Accordingly, for *M* = 1, 3, 5 and 7 the kinetic constant values of 14.16 ± 0.83 (L $mol^{-1}min^{-1}$, × 10^{-4}); 19.38 ± 2.53 (L $mol^{-1}min^{-1}$, × 10^{-4}); 34.28 ± 5.41 (L $mol^{-1}min^{-1}$, × 10^{-4}) and 27.08 ± 2.73 (L $mol^{-1}min^{-1}$, × 10^{-4}) were obtained, respectively.

4. Effect of reaction temperature

The effect of temperature ranging from 343 to 363 K on the conversion of acetic acid is investigated using $[H–Pyr]^+[HSO_4]^-$ as catalysts.

As seen from Fig. 4A, X_A increases rapidly with increasing the reaction temperature. For example, at 343 K the conversion of acetic acid after 70 min is 28%. However, when the temperature is raised up to 363 K, X_A reaches 93%. Since the esterification reaction is exothermic in nature, the registered alteration in acetic acid conversion (from 28 to 93%) is due to enhanced number of effective impacts between reactants, a consequence of the acquired kinetic energy.

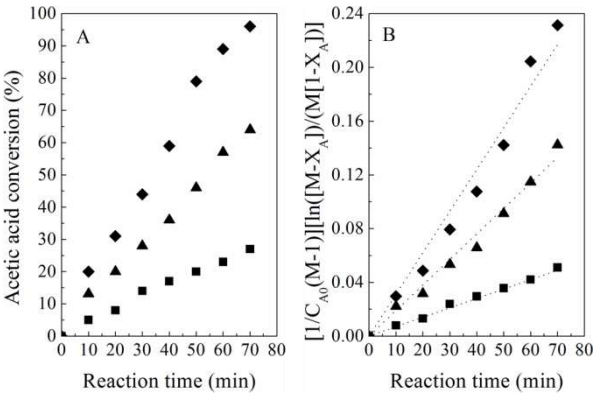

Fig. 4. Effect of reaction temperature on the acetic acid conversion **(A)** and the kinetic constant value **(B)** with time: 363 K (◆), 353 K (▲), 343 K (■), kinetic model (----). *M* – 3, catalyst loading – 10 mass.%, *t* – 70 min.

It is observed that a plot of Eq. (6) versus *t* is a straight line passing through origin, thus suggesting that the developed model is adequate to represent the system for different temperatures (Fig. 4B). The calculated kinetic constant values at reaction temperature of 363, 353 and 343 K are 31.43 ± 5.64 (L $mol^{-1}min^{-1}$, × 10^{-4}); 19.38 ± 2.53 (L $mol^{-1}min^{-1}$, × 10^{-4}) and 7.27 ± 0.65 (L $mol^{-1}min^{-1}$, × 10^{-4}), respectively.

Applying the Arrhenius law (Eq. (8)) in its linear form, the corresponding activation energy and pre-exponential factor are found.

$$\ln k_1 = \ln A - \frac{E_A}{RT} \tag{8}$$

where, k_1 – kinetic constant (L $mol^{-1}min^{-1}$), *A* – pre-exponential factor (kmol min^{-1}), E_A – activation energy (kJ mol^{-1}), *R* – gas constant (J $mol^{-1}K^{-1}$) and *T* – thermodynamic temperature (K).

The plot of $\ln k_1$ versus $1/T$ gives a straight line with the slope of $-\frac{E_A}{R}$ and intercept of ln*A* (Fig. 5). Based on the Eq. (10), the values of 77.25 kJ mol^{-1} and 767.39 kmol min^{-1} × 10^4 are

obtained as activation energy and pre-exponential factor, respectively. The calculated E_A (77.25 kJ mol^{-1}) for [H–Pyr]$^+$[HSO$_4$]$^-$ catalyst in this work is close to E_A (70.66 kJ mol^{-1}) reported by Gangadwala et al. [19] for butyl acetate synthesis in the presence of Amberlyst-15 resin. However, the pre-exponential factor values for these two catalysts are quite different – 767.39 kmol min^{-1} × 10^4 and 202.80 kmol min^{-1} × 10^3, respectively. Consequently, it could be assumed that the kinetic constant value is mainly influenced by the pre-exponential factor.

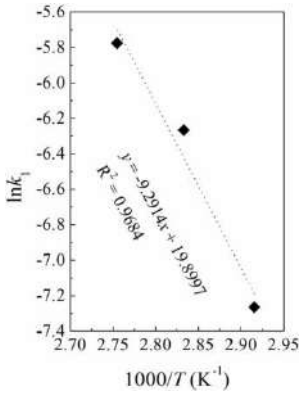

Fig. 5. Arrhenius plot for butyl acetate synthesis in the presence of [H–Pyr]$^+$[HSO$_4$]$^-$ catalysts. The dot line represent the regression of lnk_1 versus 1000/T. M – 3, catalyst loading – 10 mass.%, t – 70 min.

CONCLUSIONS

Kinetics of butyl acetate synthesis in the presence of the ionic liquids [H–Pyr]$^+$[HSO$_4$]$^-$, [H–Pyr]$^+$[H$_2$PO$_4$]$^-$ and [H–Pyr]$^+$[NO$_3$]$^-$ as catalysts is investigated in a batch reactive distillation unit.

Maximum conversion of acetic acid (64%) is obtained when [H–Pyr]$^+$[HSO$_4$]$^-$ is used as catalyst. In the cases where the process is promoted by [H–Pyr]$^+$[H$_2$PO$_4$]$^-$ and [H–Pyr]$^+$[NO$_3$]$^-$, the acetic acid conversion reaches 37 and 19%, respectively. The observed catalytic behaviour is related to the different acidity of the anion.

The acetic acid conversion increases proportionally to the catalyst loading as a consequence of the greater number of active carbonyl intermediates. It is established that above a certain value (5) of the initial reactants molar ratio, the acetic acid conversion decreases due to the dilution effect.

Two second-order pseudo-homogeneous kinetic models are successfully applied for correlation of the experimental data. Considering the kinetic equation, the activation energy and pre-exponential factor are found to be 77.25 kJ mol^{-1} and 767.39 kmol min^{-1} × 10^4, respectively.

REFERENCES

1. Sawant, D. P., A. Vinu, J. Justus, P. Srinivasu and S. B. Halligudi. *J. Mol. Catal. A: Chem.*, **276**, (2007), p. 150.
2. Das, J. and K. M. Parida. *J. Mol. Catal. A: Chem.*, **264**, (2007), p. 248.
3. Jermy, B. R. and A. Pandurangan. *J. Mol. Catal. A: Chem.*, **237**, (2005), p. 146.
4. JagadeeshBabu, P. E., K. Sandesh and M. B. Saidutta. *Ind. Eng. Chem. Res.*, **50**, (2011), p. 7155.
5. Mitran, G., O. D. Pavel and I. C. Marcu. *J. Mol. Catal. A: Chem.*, **370**, (2013), p. 104.
6. Mitran, G., T. Yuzhakova, I. Popescu and I.-C. Marcu. *J. Mol. Catal. A: Chem.*, **396**, 2015,p. 275.
7. Fraga-Dubreuil, J., K. Bourahla, M. Rahmouni, J. P. Bazureau and J. Hamelin. *Catal. Commun.*, **3**, (2002**)**, p. 185.
8. Tao, D.-J., X.-M. Lu, J.-F. Lu, K. Huang, Z. Zhou and Y.-T. Wu. *Chem. Eng. J.*, **171**, (2011), p. 1333.
9. Deng, Y. Q., F. Shi, J. J. Beng and K. Qiao. *J. Mol. Catal. A: Chem.*, **165**, (2001**)**, p. 33.
10. Anvar, S., I. Mohammadpoor-Baltork, S. Tangestaninejad, M. Moghadam, V. Mirkhani, R. Khosropour, A. L. Isfahani and R. Kia, *Comb. Sci.*, **16**, (2014**)**, p. 93.
11. Aupoix, A., B. Pégot and G. Vo-Thanh. *Tetrahedron* **66**, (2010**)**, p. 1352.
12. Wang, H., X. Bu, Z. Huang, J. Yang and T. Qiu. *Ind. Eng. Chem. Res.*, **53**, (2014), p. 17317−17324.
13. Robert, R., S. Tapio, V. Antti, H. Heikki, L. Juha, S. Anna and T. Esko. *Chem. Eng. Sci.*, **52**, (1997), p. 3369.
14. Salciccioli, M., M. Stamatakis, S. Caratzoulas and D. G. Vlachos. *Chem. Eng. Sci.*, **66**, (2011), p. 4319.
15. Schmitt, M., S. Blagov and H. Hasse. *Ind. Eng. Chem. Res.*, **47**, (2008), p. 6014.
16. Pauling, L. JACS, **54**, (1932), p. 3570.
17. Sarmini, K. and E. Kenndler. *J. Biochem. Biophys. Methods*., **38**, (1999), p. 123.
18. de Jong, M. C., R. Feijt, E. Zondervan, T. A. Nijhuis and A. B. de Haan. *Appl. Catal. A: Gen.*, 365, (**2009**), p. 141.
19. Gangadwala, J., S. Mankar and S. Mahajani. *Ind. Eng. Chem. Res.*, 42, (**2003**), p. 2146.

ANNUAL OF ASSEN ZLATAROV UNIVERSITY, BURGAS
BULGARIA, 2017, v. XLVI

EVALUATION OF COLLOIDAL INSTABILITY INDEX BY SARA METHOD

Yordanka Tasheva, Anton Palichev, Todor Palichev
E-mail: jtasheva_2006@abv.bg

ABSTRACT

To investigate heavy petroleum fraction stability by saturate, arene, resin and asphaltene analyses nine types of fractions with different components were used. The applied method for SARA quantification was used and the colloidal instability index (CII) was calculated from SARA values as well. In comparison between CII results, the values of heavy petroleum fraction compositions demonstrated that stability of asphaltenes in heavy petroleum fractions is a phenomenon that is related to all these components and it cannot be associated with only one of them, individually.

Key words: *hydrocarbon composition, SARA method, colloidal index*

INTRODUCTION

Crude oil and heavy petroleum fractions can be fractionated into four components (SARA). A reliable compositional characterization of crude oil fractions is very important for optimization, products performance evaluation, refining processes, structure property, oil source correlations, and environmental issues [1].

Chromatographic techniques have been extensively used for hydrocarbons group type determination, such as SARA fractionation. Studies in this area were first done by Jewlle et al. [2]. In these four fractions, asphaltenes have an important role in organic deposition during petroleum production and processing [1].

Deposition of asphaltenes is a well-known problem that generates an enormous cost increase in the petroleum industry. This phenomenon seriously affects petroleum production and refining operations as well. A small change in petroleum components causes asphaltene dropouts [3].

According to the Classical colloidal model, solid particles exist with a core formed by stacks of asphaltenes surrounded by resins and aromatic molecules [4]. The idea is to identify the ratio of asphaltene sources that may cause asphaltene deposition [5]. Also, reservoirs with deposited asphaltene might not be those with large amounts of asphaltene in the oil; on the contrary they might be those with high saturate fractions [2].

Colloidal instability index (CII) is an approach to determine the instability of heavy oil based on the chemical composition of crude oil [6]. The colloidal instability index (CII) suggested by Yen et al. is also applied as a widely used monitoring criterion to recognize the aphaltene deposition potential of petroleum systems [7]. In this article, a study was developed to provide experimental data of the petroleum (SARA) fractions in different crude oils mixtures and the role of these fractions on the stability of asphaltenes.

EXPERIMENT

The samples studied in this work were obtained from two kinds of petroleum, namely Tyulenovski oil and Dolno-Dabnishki petroleum, which are extracted in Bulgaria. The petroleum is processed in the Bulgarian Petroleum Refinery – Sofia. The physical and chemical properties and the composition of petroleum are given in [8].

Table 1 gives the weight percentages of mixing blends used to achieve the objective of this work.

The analyses of saturates, aromatics and resins of crude oils are obtained from ASTM D893-14. All weight percentages related to petroleum fractions have been demonstrated in Table 2.

Asphaltene fraction is one of the fractions in a categorization of crude oil samples in saturate, aromatic, resin and asphaltene (SARA) forms. Having the highest molecular weight with most enigmatic compounds of crude oils, asphaltene fractions toluene/benzene are soluble but n-heptane and n-pentane are insoluble. Asphaltene

fractions are obtained from nine heavy oil blends by a method described in [9].

From Table 2, it can be seen that the resin and asphaltene fractions are smaller than saturate and aromatic fractions.

Table 1. Weight percentages of petroleum blends

Sample	Tyulenovski oil, %	Dolno-Dabnishki oil, %
B-1	10	90
B-2	20	80
B-3	30	70
B-4	40	60
B-5	50	50
B-6	60	40
B-7	70	30
B-8	80	20
B-9	90	10

Table 2. Weight percentages of maltene fractions

No	saturates	aromatics	resins	asphaltenes
1	47.6	35.1	17.3	0.30
2	46.7	35.7	17.6	0.36
3	45.8	35.8	18.4	0.42
4	45.3	35.8	18.9	0.44
5	44.7	35.7	19.6	0.48
6	44.3	34.9	19.8	0.54
7	43.9	34.9	21.2	0.58
8	43.5	32.8	23.7	0.66
9	43.1	32.8	24.1	0.70

The CII is expressed as the sum of asphaltenes and saturates per the sum of aromatics and resins:

CII = (Saturates + Asphaltenes)/(Resins + Aromatics) (1)

If oil has a CII value below 0.7, it is defined as stable and if the CII is higher than 0.9, it is considered as unstable.

Those practical methods are considered as a preliminary screening analysis for asphaltene deposit problems. It is strongly recommended to have more studies on laboratory experiments to solve the potential problems. From Table 3, it can be seen that the ratio of asphaltenes to resins (As. /Re.) and saturates to aromatics (Sa. /Ar.), as well as the results of CIIs are tabulated for the nine crude oil blends.

Based on the results from Table 3, the CII value from sample No. 1 is 0.91. The CII values from sample No 2 to 9 are from 0.7 to 0.9.

The correlation between saturates, resins, aromatics, asphaltenes and CII are given in figures 1 to 4.

Table 3. Hydrocarbon group ratio and CII results

No.	As/Res.	Sat/Arom	CII
1	0.01734	1.3561	0.91
2	0.02045	1.3081	0.88
3	0.02283	1.2793	0.85
4	0.02328	1.2654	0.84
5	0.02449	1.2521	0.82
6	0.02727	1.2693	0.82
7	0.02736	1.2579	0.79
8	0.02785	1.3262	0.78
9	0.02905	1.3140	0.77

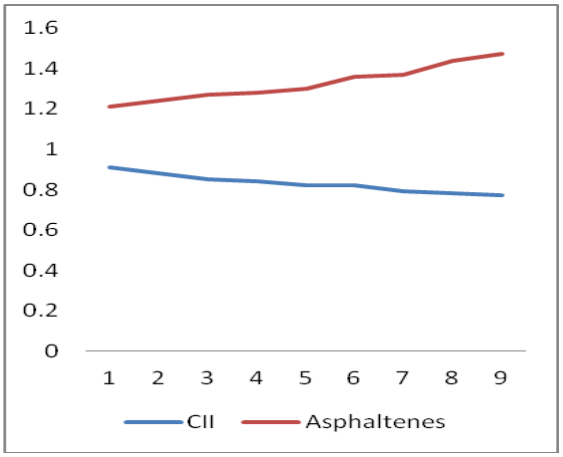

Fig. 1. Correlation between asphaltenes and colloidal instability index

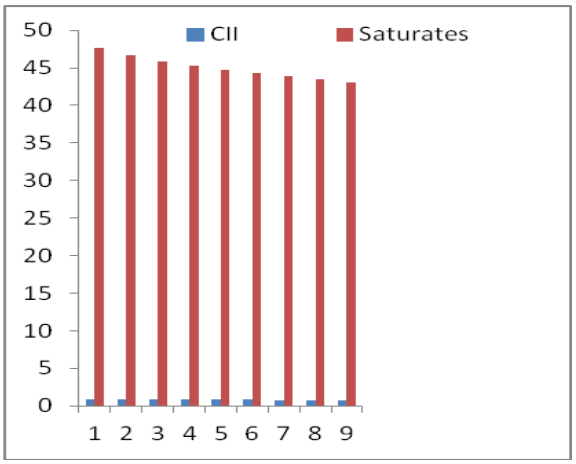

Fig. 2. Correlation between saturates and colloidal instability index

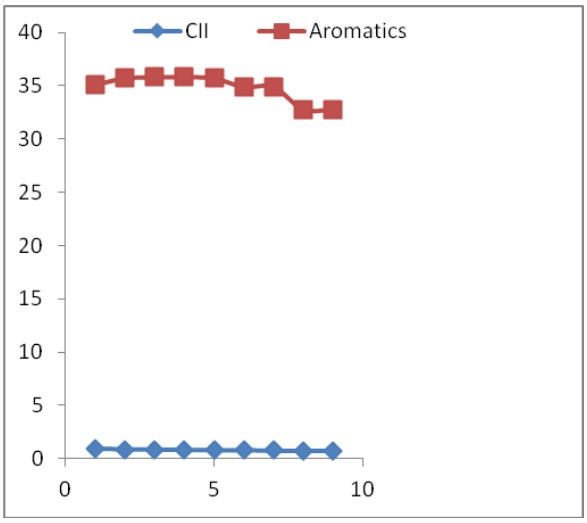

Fig. 3. Correlation between aromatics and colloidal instability index

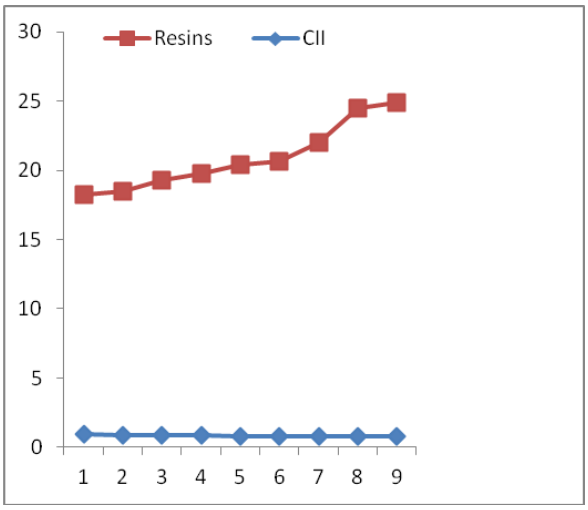

Fig. 4. Correlation between resins and colloidal instability index

RESULTS AND DISCUSSION

According to the above figures, it is generally accepted that each of the fractions influence the stability of crude oil mixtures. Stable oil blend has higher polar fraction values, i.e. for asphaltene, resin and aromatic. Nonpolar fraction causes saturation of crude oil blend which has an important role in stability as well as in petroleum that has a higher value of saturate the probability of a decrease in stability becomes apparent.

By spot colloidal model provisions and the achieved results, it may be concluded that prcipitation is believed to occur when the resins are stripped from the colloid allowing aggregation and phase separation to occur. Resins have a strong tendency to associate with asphaltenes due to their opposite charge and are absorbed by asphaltenes to become a protective shield for asphaltene. When this protective shield of resins is removed, it might lead to the precipitation of asphaltenes. Probably, the destabilization (i.e. flocculation) of colloidal asphaltenes in oil production systems depends principally on breaking up the balance of attraction forces between the absorbed resin molecules and asphaltene particles. The resins are considered to be the crucial component in holding the asphaltene micelles in suspension.

Both resin and asphaltene have polar constituents but the difference between them depends on miscibility with n-pentane or n-heptane, asphalttene is insoluble, while resin is miscible.

Resins have a strong tendency to associate with asphaltenes. A larger precipitation of asphaltene results in a decrease in resin content. Resins adsorb onto the asphaltene aggregates and keep them dispersed in the crude oil medium. It may suggest that asphaltenes are the centres of micelles formed by adsorption or even by absorption of resins onto the surfaces or into the interiors of asphaltene particles as well. Hence for asphaltenes to stay in the solution, resins must be present. The core of the micelle is occupied by one or several asphaltene ‘‘molecules” and is surrounded by interacting resins. Resins are surrounded by aromatics which ensure a progressive transition to the bulk of petroleum where saturated hydrocarbons are usually predominant. Asphaltenes and resins are hetero compounds and form the most polar fraction of crude oil. Dilution of the resins below a certain threshold will cause the asphaltenes to precipitate.

It is generally accepted that the asphaltene molecules are dispersed in the oil by the polar molecules, aromatics, and resins, thus stating that the asphaltenes are colloidal dispersed in crude oil. Considering crude oil as a colloidal system, asphaltenes and resins comprise the dispersed phase while saturates and aromatics form the continuous phase. The overall structure would be of a micellar type: the cores of the nature of asphaltenes together with the nature of the dispersion medium are also important factors that determine the relative stability of crude oils and related materials. The interaction among both phases and their influence on the stability of the system is related to the peptizing power of the resins, the solvent effect of the aromatics, the precipitant properties of saturates and the flocculation tendency of asphaltenes. As mentioned before, resins are the most polar fraction, and

aromatic species are present in deasphalted oil and, it has been suggested, contribute to the enhanced solubility of asphaltenes in crude oil by solvating the polar and aromatic portions of the asphaltenic molecules and aggregates. In opposition to the contents of saturates, a higher percentage of aromatics and resins could confer to the oils a higher capacity to keep asphaltenes in solution. The attractive interactions experienced by colloidal-sized asphaltene aggregates near the onset of precipitation are probably dominated by nonpolar Van Der Waals forces. It is generally accepted that the asphaltene molecules are dispersed in the oil by the polar molecules, aromatics, and resins, thus stating that asphaltenes are colloidal dispersed in crude oil.

The study of the crude oil composition (saturates, aromatics, resins and asphaltenes) demonstrates that the stability of asphaltenes in crude oils is a phenomenon that is related to the behaviour of all these components and the influence of each fraction is on other fractions according to their polarity as well, but it cannot be associated with only one of them, individually.

REFERENCES

1. Verdier S., Experimental study and modeling of asphaltene precipitation caused by gas injection (Ph.D. thesis), Technical University of Denmark, (2006).
2. Ting D., Thermodynamic stability and phase behavior of asphaltenes in oil and of other highly asymmetric mixtures (Ph.D. thesis), Rice University of Houston, Texas, (2003).
3. Guilherme, P., M. Magorie, M., R. Vinicius, *Fuel* **115**, (2014), p. 190.
4. Petkova, N., M. Angelova, P. Petkov, *Petroleum & Coal*, **51**, (2009) p. 286.
5. Stratiev, D., I. Shishkova, T. Tsaneva, M. Mitkova, D. Yordanov, *Fuel*, **170**, (2016), p. 115.
6. Balabin R., R. Syunyaev, T. Schmid, J. Stadler, *Energy Fuels*, **25**, (2010), p. 189.
7. Ashoori S., M. Sharifi, M. Masoumi and M.Salehi, *Egyptian Journal of Petroleum*, **26,** (2017), p. 209.
8. Tasheva Y., A. Palichev, T. Palichev, *Industrial Technologies*, **4**, (2017), p. 132.
9. Tasheva, Y., I. Lazarov, *Petroleum&Coal*, **57,** p. 141.

ANNUAL OF ASSEN ZLATAROV UNIVERSITY, BURGAS
BULGARIA, 2017, v. XLVI (1)

PERSISTENCE, BIOACCUMULATION AND TOXICITY OF BIODEGRADED METABOLITES OF PETROLEUM BENZENE IN THE ENVIRONMENT

Yana Koleva, Yordanka Tasheva
E-mail: jtasheva_2006@abv.bg

ABSTRACT

Chemicals that are persistent in the environment, bioaccumulate in people and/or wildlife, and are toxic are called PBTs. Because of these features, as long as they remain on the market and can be therefore released in the environment, they will threaten the health of humans and wildlife. The nature of the risk will depend on their specific toxic properties, the size of the exposed population or ecosystem, and the extent and duration of exposure. Benzene is a simple cyclic organic compound which is found naturally in the environment at low concentrations. Benzene occurs naturally in crude oil and as a consequence is a constituent of petrol. The aim of this work is to predict the possible microbial metabolites of petroleum benzene and their persistence, bioaccumulation and toxicity using (Q)SAR Application Toolbox and PBT Profiler software.

Key words: *persistence, bioaccumulation, toxicity, metabolites, petroleum benzene, environment*

INTRODUCTION

The quality of life on earth is linked inextricably to the overall quality of the environment. Release of persistent, bioaccumulative and toxic chemicals has a detrimental impact on human health and the environment. Petroleum hydrocarbon is one common example of a chemical which enters the environment frequently and in large volumes through numerous routes. The problem is worldwide, but more severe in the developing countries, where there are no effective regulatory policies on the environment [1].

Changes in gasoline formulations to reduce benzene content and the use of fuel-efficient vehicles or natural gas-powered vehicles were considered to likely have the greatest impact in reducing benzene emissions in the environment. A marked decrease in benzene emissions has been noted since 1975 [2]. The four primary processes that control the rate and behaviour of benzene in the environment are (1) evaporation or volatilization into the gas phase coupled with diffusive transport in the gas phase; (2) sorption to soil, particularly to organic matter; (3) biodegradation; and (4) leaching by rainwater infiltrating through the unsaturated zone and/or dissolution in groundwater [3].

Organic substances that are persistent, bioaccumulative and possess toxic characteristics likely to cause adverse human health or environmental effects are called PBTs (Persistent, Bioaccumulative, Toxic substances). In this context, 'substance' means a single chemical species, or a number of chemical species which form a specific group by virtue of (a) having similar properties and being emitted together into the environment or (b) forming a mixture normally marketed as a single product. Depending on their mobility in the environment, PBTs could be of local, regional or global concern. Under the auspices of the United Nations Economic Commission for Europe (UNECE), the Convention on Long-Range Transboundary Air Pollution (CLRTAP), a protocol on persistent organic pollutants (POPs) has been drawn up, in which POPs are defined as 'a set of organic compounds that: (i) possess toxic characteristics; (ii) are persistent; (iii) are liable to bioaccumulate; (iv) are prone to long-range atmospheric transport and deposition; and (v) can result in adverse environmental and human health effects at locations near and far from their sources' [4].

The aim of this work is to predict the possible microbial metabolites of petroleum benzene and their persistence, bioaccumulation and toxicity using (Q)SAR Application Toolbox and PBT Profiler software.

MATERIALS AND METHODS

Compounds. The microbial metabolites of petroleum benzene were investigated and are presented in Table 1.

OECD (Q)SAR Application Toolbox. (Quantitative) Structure-Activity Relationships [(Q)SARs] are methods for estimating properties of a chemical from its molecular structure and have the potential to provide information on the hazards of chemicals, while reducing time, financial costs and animal testing currently needed. To facilitate the practical application of (Q)SAR approaches in regulatory contexts by governments and industry and to improve their regulatory acceptance, the OECD (Q)SAR project has developed various outcomes such as the principles for the validation of (Q)SAR models, guidance documents as well as the QSAR Toolbox [5].

Metabolic pathways documented for 200 organic chemicals in different mammals are stored in a database format that allows easy computer-aided access to the metabolism information. The collection includes chemicals of different classes, with a variety of functionalities, such as aliphatic hydrocarbons, alicyclic rings, furans, halogenated hydrocarbons, aromatic hydrocarbons and haloaromatics, amines, nitro-derivatives, and multifunctional compounds. *In vivo* and *in vitro* (predominantly, with liver microsomes as experimental systems) studies were used to analyze the metabolic fate of chemicals. Different sources, including monographs, scientific articles and public websites were used to compile the database [5, 6].

Criteria used by the PBT Profiler. The PBT Profiler is a screening-level tool that provides estimates of the persistence, bioaccumulation, and chronic fish toxicity potential of chemical compounds. It is designed to be used when data are not available. In order to help interested parties make informed decision on a chemical's PBT characteristics, the PBT profiler automatically identifies chemicals that may persist in the environment and bioaccumulate in the food chain. These chemicals are identified using thresholds published by the Environmental Protection Agency (EPA) [7].

Persistence criteria. The PBT Profiler combines the persistence criteria for water, soil, and sediment and highlights chemicals with an estimated half-life ≥ 2 months and < 6 months as persistent and those with an estimated half-life ≥ 6 months as very persistent. The half-life in air is not used in the PBT Profiler's Persistence summary (chemicals with an estimated half-life > 2 days are considered as persistent). The PBT Profiler uses 30 days in a month for its comparisons.

Bioaccumulation criteria. The PBT Profiler combines the bioaccumulation criteria and highlights chemicals with a BCF ≥ 1000 and < 5000 as bioaccumulative and those with a BCF ≥ 5000 as very bioaccumulative.

Toxicity criteria. To highlight a chemical that may be chronically toxic to fish, the PBT profiler uses the following criteria: Fish ChV (Chronic Value) > 10 mg/l (low concern), Fish ChV = 0.1 - 10 mg/l (moderate concern) and Fish ChV < 0.1 mg/l (high concern).

RESULTS AND DISCUSSION

The PBT profiler uses a well-defined set of procedures to predict the persistence, bioaccumulation, and toxicity of chemical compounds when experimental data are not available [8]. The persistence, bioaccumulation, and fish chronic toxicity values estimated by the PBT profiler are automatically compared to criteria published by EPA. Chemicals that are persistent, bioaccumulative, and toxic have the potential to concentrate to levels that may cause significant averse impact on human health and the environment.

The results of the possible observed microbial metabolites of petroleum benzene and their persistence, bioaccumulation and toxicity by softwares of (Q)SAR Application Toolbox and PBT Profiler are presented in Table 1.

Table 1. PBT Profiler estimate of observed microbial metabolites of petroleum benzene

Name of observed microbial metabolites of petroleum benzene	Persistence		Bioaccumulation	Toxicity
	Media (water, soil, sediment, air) Half-life (days)	Percent in Each Medium	BCF	Fish ChV (mg/l)
5,6-Dihydroxy cyclo	8.7; 17; 78; 0.026	43%; 57%; 0%;	3.2	0.4

hexa-1,3-diene		0%		
1,2-Benzenediol	15; 30; 140; 0.15	18%; 82%; 0%; 0%	3.2	14
2-Hydroxy-6-oxo-2,4-hexadienoic acid	8.7; 17; 78; 0.38	28%; 72%; 0%; 0%	3.2	0.46
2,4-Hexa diene dioic acid	8.7; 17; 78; 0.54	25%; 75%; 0%; 0%	3.2	8,500
2-Oxo-4-pentenoic acid	8.7; 17; 78; 0.36	34%; 66%; 0%; 0%	3.2	1000
4-Hydroxy-2-oxo pentanoic acid	8.7; 17; 78; 0.58	33%; 66%; 0%; 0%	3.2	18,000
2-oxo-propanoic acid	8.7; 17; 78; 26	34%; 66%; 0%; 0%	3.2	4,100
Acetaldehyde	15; 30; 140; 1	48%; 47%; 0%; 5%	3.2	12
Acetic acid	8.7; 17; 78; 22	35%; 62%; 0%; 3%	3.2	2,000
Formal dehyde	15; 30; 140; 1.7	43%; 54%; 0%; 3%	3.2	3.6
Formic acid	8.7; 17; 78; 36	35%; 61%; 0%; 4%	3.2	460

Analysis of the data in Table 1 reveals that some observed microbial metabolites of petroleum benzene are persistent and toxic (Fish ChV). The PBT Profiler estimates that the four observed microbial metabolites are not expected to bioaccumulate in the food chain because they do not exceed the BCF criteria. The compounds have moderate to low toxicity.

Predicted microbial metabolites of petroleum benzene and their persistence, bioaccumulation and toxicity using both software products are presented in Table 2.

Table 2. PBT Profiler estimate of predicted microbial metabolites of petroleum benzene

Name of predicted microbial meta bolites of petroleum benzene	Persistence		Bio accu mula tion	Toxi city
	Media (water, soil, sedi ment, air) Half-life (days)	Per cent in Each Me dium	BCF	Fish ChV (mg/l)
1,2-Benzenediol	15; 30; 140; 0.15	18%; 82%; 0%; 0%	3.2	14
2-Hydroxy-6-oxo-2,4-hexa dienoic acid	8.7; 17; 78; 0.38	28%; 72%; 0%; 0%	3.2	0.46
2-Hydroxy-2,4-penta dienoic acid	8.7; 17; 78; 0.26	42%; 56%; 0%; 1%	3.2	2.2

Analysis of the predicted microbial metabolites of petroleum benzene in Table 2 reveals that it is persistent and toxic and does not bioaccumulate in the food chain. The metabolites have moderate to low toxicity.

CONCLUSION

The PBT Profiler is an online risk-screening tool that predicts a chemical's potential to persist in the environment, bioconcentrate in animals, and be toxic, properties which cause concern for human health and the environment. Using this tool for the investigated, observed and predicted microbial metabolites of petroleum benzene, it was established that, according to the Criteria used by the PBT Profiler, they are persistent, do not bio-accumulate in the food chain and have moderate to low toxicity.

REFERENCES

1. Onuoha, S.C., V.U. Olugbue, J.A. Uraku and D.O. Uchendu. *International Journal of Agriculture & Biology*, **13** (2011), p.586.

2. Jacques, A.P. National inventory of sources and emissions of benzene (1985). Report EPS 5/AP/1. Environment Canada, Ottawa, 1990.
3. Canadian Soil Quality Guidelines for the Protection of Environmental and Human Health. Canadian Council of Ministers of the Environment, 2004.
4. UN-ECE. Draft Protocol to the Convention on Long-range Air Pollution on Persistent Organic Pollutants, (EB.AIR/1998/2), Convention on Long-range Transboundary Air Pollution, United Nations Economic and Social Council, Economic Commission for Europe, 1998.
5.OECD (Q)SARs Application Toolbox: http://www.oecd.org/document/23/0,3343,en_2649_34379_33957015_1_1_1_1,00.html
6. Mekenyan, O.G., S.D. Dimitrov, T.S. Pavlov, G.D. Veith. *Current Pharmaceutical Design*. **10** (2004), p.1273.
7. Criteria used by the PBT Profiler: http://www.pbtprofiler.net/criteria.asp; Girard, J.E. *Chapter 14. Organic chemicals in the environment. In Principles of Environmental Chemistry*, 2nd ed., Jones & Bartlett Publishers. LLC, 2010, p.402.
8. Koleva, Y.K.. *Annual Assen Zlatarov University-Burgas*, XLI (2012), p.64.

ANNUAL ASSEN ZLATAROV UNIVERSITY, BURGAS, BULGARIA, 2017, v. XLVI (1)

ASSESSMENT OF THE HUMAN RELIABILITY IN A COMPANY FROM THE CHEMICAL INDUSTRY

Sabina Nedkova [1], Plamena Atanasova [1], Ruska Myhailova [2], Marusia Lybcheva[2]
E-mail: sabina_nedkova@abv.bg

[1] *Department of Technologies, Materials and Material Science, Technical Faculty, Prof. Assen Zlatarov University, Burgas 8010, Bulgaria*
[2] *Prof. Assen Zlatarov University, Burgas 8010, Bulgaria*

ABSTRACT

Human reliability assessment for prevention and management of technological risks is a very important, yet not well enough explored area in Bulgaria. This fact can be explained by the specific features of our economy, where the place of the human, as the most valuable asset of any company, is still not well defined, along with the efforts directed towards assessment and development of human reliability. Most difficulties when assessing a worker are related to the diverse expressions of human behaviour, and their effect on different risk zones of the technological processes. The following study is aiming to assess how the human behaviour of workers in a chemical company influence the execution of their work duties, by using data from a test system and a mathematical model for risk assessment through integral risk index.

Key words: *human reliability, integral risk index*

INTRODUCTION

The following study is based on the application of the mathematical model for assessment of the integral risk index and human reliability of workers in a chemical company in Bulgaria. To collect the data needed for the research a test system developed for evaluation of the correlation between the theoretical model for the assessment of human reliability and the accuracy of its factors, their constituents and range is used [1].

The test system was applied on twenty-one people, working at different job positions in a factory producing phosphate compounds in Bulgaria. They included: a head of the shifts of operators, a technologist, a head of operational activity, an administrative assistant, an accountant, a financial controller, a chief legal consultant, a sales expert, a stock manager, a specialist of supplies. The applied test system was implemented as a questionnaire of 80 questions, divided into five groups according to the five basic factors chosen in the mathematical model for integral risk index: Professional characteristic, Personal characteristic, Team behaviour, Physical condition and Work environment. The five point scale response ranging from maximum to minimum was used: strongly agree, agree, neither agree nor disagree, disagree and strongly disagree. Every employee completed the questionnaire in person as a self-assessment of his/her characteristics. The test system included the following information groups: General information; Professional characteristics; Personal characteristics; Work environment; Physical condition and Collective/Team behaviour.

EXPERIMENT

The main idea of the study is to assess the human reliability of the tested workers in a qualitative and quantitative way, by implementing the gathered data in the developed mathematical model for integral risk index. The results should be interpreted as theoretical and could not be related to the image or the production of the company.

The main problem we faced when gathering experimental data and assessing the human reliability, was the reluctance of a company to spend the time of its employees on something, not directly related to its area of activity. This is particularly true in chemical companies, where employees have specific tasks with high importance and not enough time for additional activities such as scientific research. The company producing phosphate products not only

did not reject our request, but returned over twenty filled questionnaires-test systems, which made us proud and optimistic for the development of the subject of human reliability in the chemical industry sector in Bulgaria. The fact that this company took care of their employees deserves respect and admiration.

For the sake of the characteristic of our study-survey on the human reliability in the chemical industry, from all 21 respondents we had from all departments of the company, we chose those 12 from them who are directly involved in the technological process of chemical production, with the ensuing duties and responsibilities.

The test system was applied to 12 employees with different levels of responsibility and different work duties. Amongst them are: Head of shift - 2 people, Head of storage – 1 person, Device operator - 4 people, Device operator-drying and granulation (dg) - 1 person, Storage organizer - 1 person, Technologist – 2 people and a Manager of operational activity. The people had different years of work experience (YE). Using the data from the test system and the mathematical model for integral risk index, we calculated the risk index of each person both quantitatively and qualitatively (R_{int}) as well as their human reliability (HR) (Table 1).

Table 1. Integral risk index of employees, years of work experience and human reliability

profession	Head of shift	Head of shift	Head of storage	Device operator	Device operator	Device operato (dg)	Storage organizer	Techno-logist	Device operator	Device operator	Manager operational activity	Techno-logist
YE	11	14	11	9	1	16	5	11	10	7 months	-	2
R_{int}	0,291	0,368	0.321	0.389	0,381	0.348	0.305	0,300	0,406	0,517	0,379	0,350
Risk index	low	low	low	medium	medium	low	low	low	medium	medium	medium	low
HR	high	high	high	medium	medium	high	high	high	medium	medium	medium	high

RESULTS AND DISCUSSION

All of the assessed people, working in the technological process of the company have low and medium level of integral risk index, respectively high and medium level of human reliability.

This means that all of the respondents are developing their duties with responsibility and care in such a way that their behaviour can contribute to the realization of accidents on a comparatively small scale - because of their low and medium integral risk index - the lower the risk index is, the higher the human reliability.

The results obtained can be explained by the level of human reliability on the opposite way. The higher level of human reliability is, the lower is the probability of the person to develop conscious actions which can lead to a technological accident.

Although all the results of the respondents are in the low and medium risk scale, we would focus on the best result, which would be displayed with its integral risk index profile, through which the most important factor for this case would be seen (Fig. 1).

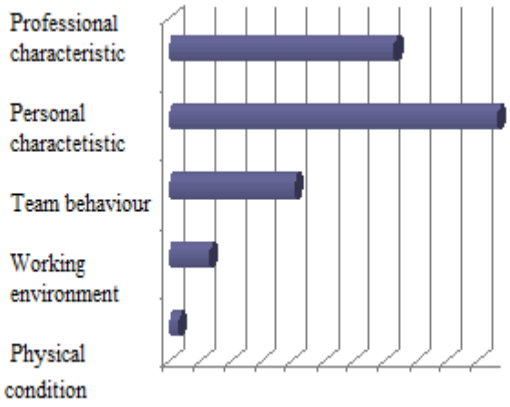

Fig. 1. Integral risk index profile of Head of shift with 11 years of experience

The best result we obtained belongs to the Head of shift with 11 years of work experience at this position. His integral risk index is in the low scale, which means that there is a low probability for his behavior and the way he executes his work obligations, solely or as a part of a team, to initiate a high scale accident, risk or critical event. Here it is quite important to underline, that our concept of human reliability is not related to task analysis which can be simply defined as the study of what a person is required to do, in terms of actions and mental processes, to achieve a goal [2]. Human reliability is inversely proportional to the integral risk index and this is an assessment of five general factors, which

assess the professional qualification of the respondent with its working obligations, the way its personal characteristic is relevant to his work, how he blends in the team, what is his physical condition and which are (if there are any) the dangers in the surrounding environment. We consider this analysis as more complex and challenging.

According to our research, the Head of the shift with 11 years of work experience had an integral risk index of 0.291, which means low risk and high human reliability.

As can be seen in Figure 1, this result is due not only to his professional qualification, but because of his personal characteristics. This person has only secondary education, he does not have many professional qualifications, but according to him, the theoretical knowledge is less needed than the practical that he has gained from his 11 years of work in the plant.

As head of shift, he has to manage a group of technologists, who should act as a team, while working on the plant. He has a management role for one production team/shift, which is why he should be responsible for developing efficient work methods, and collaborating with workers to increase productivity while maintaining the production process in a safe and effective way.

His personality is very important and the low level of his integral risk index comes exactly because the test system data, produced by the mathematical model, described that his personal profile fully meets the requirements of the position.

He is responsible, well organized, has a very good connection with the rest of the team, the people he manages like and respect him, he is fair and objective.

All 12 people engaged with the technological process, were asked to rank the five factors which are included in the integral risk index determination by importance for the effective and safe execution of their working activities. 7 respondents out of 11 ranked professional qualification as the most important for human reliability, 2 of them pointed out behaviour as the most important, 1 - the health condition of the worker and only 1 pointed out the personality (Fig. 2).

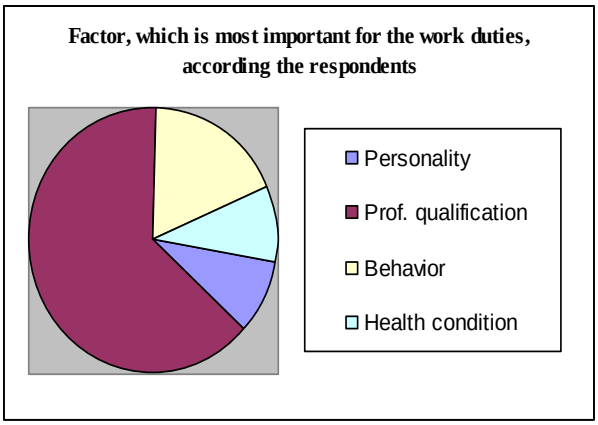

Fig. 2. Ranking of the five basic factors

People believe that training provides competences, so when competences have to be provided, education is the answer, but most of the time, training is overemphasized because it is the easy option. It is time-consuming and therefore expensive to assess a person's competence adequately, since it involves observation of their performance at work [3].

The results received by us prove this theory, but still the qualification people receive at university should be upgraded with practice, which is the case with the person with the best result, who does not have university education, but 11 years of success in management of the people and the technological process he is in charge of.

There is quite an interesting score in the question where the respondents are required to list the personal features of a person who would do their job in the best possible way, with less risk for a critical event. All respondents were invited to choose from a list of characteristics, giving more than one answer.

According to the respondents, the personal profile of the best worker is a person who is polite, calm, positive, decisive, persistent and talkative. Most of them pointed out "calmness" as the most important feature - 8 out of 11 people.

This fact can be explained with the intense working and production process, where a calm person would best contribute to the effectiveness of the process.

7 out of 11 people pointed out "positive", 6 chose "polite" and "decisive", five "talkative" while "persistent" came last (Fig. 3).

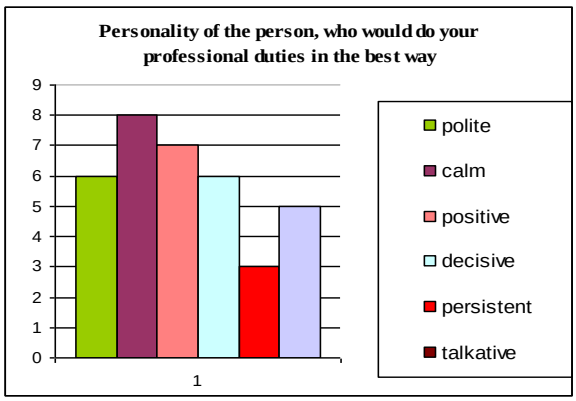

Fig. 3. Most needed personality features

The results show that the ability of the person to communicate with the rest of the team is of great importance for the formation of the so-called "safe' working environment in which the people behave and execute their activities without stress and tension. In this technological environment and the exact parameters which should be obtained, the importance of every person as part of a team increases. In this context the development of safe working environment, means to develop conditions which would reduce the probability of human error and prevent an accident from happening.

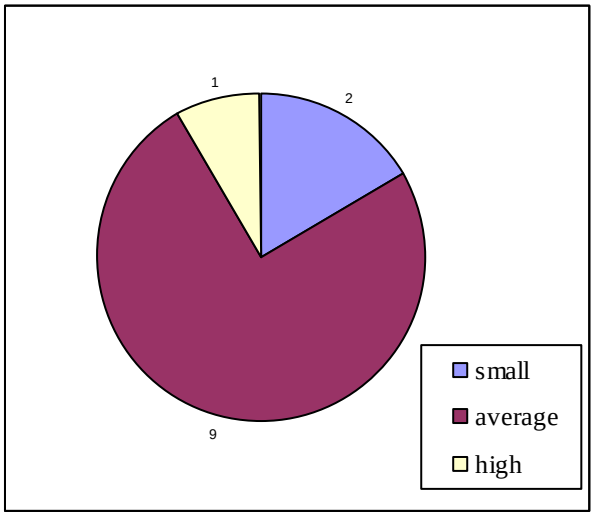

Fig. 4. Level of danger in the technological processes

This theory is proved by the results shown in Fig.4, which summarizes the data from the test system focused on the opinion of the respondents about the level of danger in the technological plant where they work. According to most of them, the danger is of average level (9 out of 12 people), small (2 out of 12 people) and high level (1 out of 12 people), which means that the technological equipment is effective and secure and the workers feel confident and well, working with it.

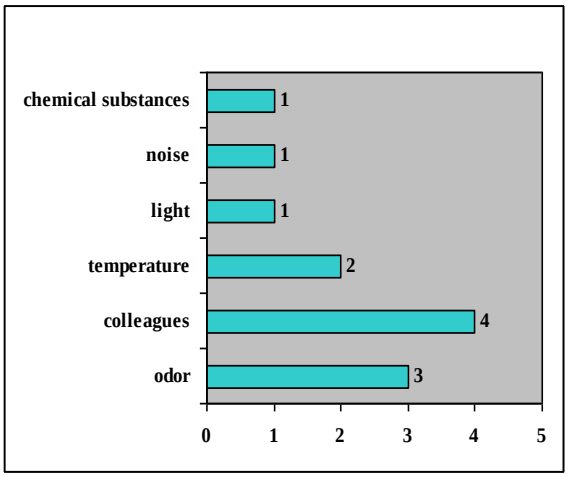

Fig. 5. What feature of the surrounding environment do you consider capable of generating danger on the technological site?

When asked about the sources of danger in the surrounding environment (Fig.5), most of the people pointed out "colleagues". The information can be connected with the results described in Fig. 3, and the most appreciated quality of a person, which is "calm". It seems that this personal feature is quite necessary for the development of safe and effective work area, which increases human reliability and the overall work efficiency.

CONCLUSION

The technological process is a complex process with lots of obvious and hidden risk zones, where people have to implement their knowledge and skills as a team, trying to meet both the high requirements of the process and the difficulties of working jointly in the team. The team is the area which acts like a mirror, strengthening the good qualities of the person when his place is right and his position includes the right duties and responsibilities, and deepening the bad qualities, if he does not feel wanted, understood or accepted. Without being part of the professional training, personal development is part of the development of a safe working environment, which is equally important for the efficiency of the working process. As a complex factor, human reliability should be a subject of research and the means of its increasing and improvement should be implemented in any type of system and process. This factor is not only related to the ratio between the failures and the correct actions of

the man-machine system, but to the complex evaluation of the sub-factors that influence it, one of the most important of which is the personal characteristic of the worker.

REFERENCES

1. S.Nedkova, R.Dimitrova, M.Lybcheva, Human reliability assessment, through integral risk index, International Journal of Scientific Research Volume: 4, Issue: 5, May – 2015, page 244-268

2. Kirwan,B. and Ainsworth, L.K. (1992) *A guide to task analysis*, Taylor and Francis

3. Boyle Tony, Health and Safety: Risk Management, Routledge, 2015

ANNUAL OF ASSEN ZLATAROV UNIVERSITY, BURGAS
BULGARIA, 2017, v. XLVI (1)

ESTIMATION OF THE SOLAR POTENTIAL IN THE MUNICIPALITY OF BURGAS

Zdravka Nikolaeva
E-mail: z.v.burieva@gmail.com

ABSTRACT

The paper reports the monthly average and annual estimation of the solar potential and the cloud cover made at three monitoring sites in the Municipality of Burgas: AMS Meden Rudnik, DOAS OPSIS and AMS Dolno Ezerovo. The data were taken at noon (12:00 local time, GMT+2), when the solar radiation has a maximum. The dependence between the measured and calculated cloud cover was studied. The total solar radiation and the corrected radiation were compared with respect to the cloud cover. The calculated total solar radiation can be used for scientific purposes, e.g. for estimation of the solar potential in the Municipality of Burgas. An estimation of the annual amount of solar radiation for the Municipality of Burgas was made, which can be used for practical purposes, e.g. design of photovoltaic parks, design of heating and cooling domestic installations, greenhouses, etc.

Key words: *solar potential, total solar radiation, cloud cover, regression model, coefficient of determination.*

INTRODUCTION

Solar radiation is the main source of energy for almost all natural physicochemical processes taking place on the ground and in the atmosphere [1, 2]. Only about 27% of the solar radiation, called direct solar radiation, reaches the surface of the earth [3]. Together with part of the diffused energy, which also reaches the surface, it forms the total solar radiation. According to the International System of Units (SI) [4], the amount of global radiation per unit area per unit time G is called intensity or "insolation".

The Earth's irradiation depends on a number of factors, but the orbital mechanics stipulating the planet trajectory and thus the distance and angle by which the planet stands against the Sun is the most important one. The average arithmetic insolation (solar or sun constant) reaching a surface perpendicular to the Sun's direction and at a distance from the Sun equal to the arithmetic average distance between the Earth and the Sun (astronomic unit AU = 149 597 870.691 km) is considered to be 1367.7 W/m^2, according the latest data from NASA [5] and it is denoted by I_{SC} [4].

The total global insolation incident directly on a horizontal area of the Earth (Global Horizontal Irradiation) GHI - G_0 is a function of the angle of the Sun above the horizon and the cloud cover. The monthly average and annual values of this radiation are mainly used for practical purposes, such as the design of solar energy parks, design of heating and cooling installations, greenhouses, etc.

The use of renewable energy is highly stimulated by the European Union and the main regulation dealing with the power generation by renewable sources is Directive 2001/77/ EC on the promotion of electricity produced from renewable energy sources in the internal electricity market. The national indicative goal for Bulgaria is to reach 16% of the total energy supply to be generated from renewable sources [6]. The total installed electricity generation power of the photovoltaic parks is planned to be 200 MW, which is about 5% of the total power generated by renewable sources.

In the present paper, estimation is made of the monthly average and annual solar potential and cloud cover at three monitoring sites in the Municipality of Burgas: AMS Meden Rudnik, DOAS OPSIS and AMS Dolno Ezerovo.

MATERIALS AND METHODS

Sunshine duration is the total time (day, month, year or other period) of direct sunshine. It is expressed in hours and tenths of hours (absolute sunshine duration) or percentage of the as-

tronomically possible duration (relative sunshine duration) [7].

The total global insolation (total extraterrestrial solar radiation) G_0 can be determined by the formula of Klein [8]

$$G_o = \frac{24}{\pi}.I_{SC}.\left(1+0.033.cos\left(\frac{360.d}{365}\right)\right). \left(cos\phi.cos\delta+\frac{\pi.\omega_S}{180}sin\phi.sin\delta\right), \quad (1)$$

where: ϕ –geographic latitude, degree; δ –declination, degree; I_{SC} = 1367.7 W/m^2–solar constant; ω_S – hour angle of the sunrise, degree.

The hour angle ω_S and sun declination δ can be determined by the equations:

$$\omega_S = cos^{-1}[cos(-tan\phi.tan\delta)];$$

$$\delta = 23.45.sin\left(360.\frac{284+d}{365}\right),$$

where: d is the day of the year. Usually, the 15th day of the month is taken to calculate the solar radiation.

Sun height is determined by the formula:

$$\sin h = \sin\phi.\sin\delta + \cos\phi.\cos\delta.\cos\omega, \quad (2)$$

where: ϕ –geographic latitude, degree; δ – declination, degree; ω –hour angle, degree.

In the present paper, a simplified model is suggested for determination of the hourly values of the total solar radiation on a monthly basis for the different monitoring sites. It describes the dependence between the total solar radiation G and the astronomic time. The regression model used was polynomial of the type:

$$G = b + a_1 t + a_2 t^2 + a_3 t^3 + a_4 t^4 + a_5 t^5 + a_6 t^6 \quad (3)$$

where: b, a_1, a_2,...., a_6 –regression coefficients, t– time.

Monthly average and annual estimation of the relationship between the total global insolation G_o (called Global Horizontal Irradiation GHI) and the amount of clouds. The data were taken at local noon (12:00, GMT+2), when the incident GHI is maximal. A comparison was made between the GHI corrected for the cloud cover and the total solar radiation G measured. The measured and calculated values of cloud cover at the monitoring sites were compared. Estimation was made for the solar potential of the Municipality of Burgas. The values of the radiation obtained were compared with these obtained by the estimation of the potential of the average annual solar radiation for the Burgas Region [9].

By comparison between the measured and calculated values, the quality of the regression models [10, 11, 12] was estimated by the coefficient of determination R^2 which shows the extent of the linear dependence between the regressors included in the model and the predicted value of the initial variable**.**

RESULTS AND DISCUSSION

The paper reports the monthly average and annual estimation of the solar potential and the cloud cover made at three monitoring sites in the municipality of Burgas: AMS Meden Rudnik (European code BG0056A; geographic coordinates N42^0 28’ 01”, E27^0 23’ 23”), DOAS OPSIS (European code BG0063A; geographic coordinates N42^0 31’ 07”, E27^0 26’ 18”) and AMS Dolno Ezerovo (European code BG0044A; geographic coordinates N42^0 31’ 05”, E27^0 22’ 01”).

The total global insolation incident directly on a horizontal area of the Earth (Global Horizontal Irradiation) GHI – G_0 is a function of the angle of the Sun above the horizon and the cloud cover.

The following parameters were calculated for the monitoring sites in the Municipality of Burgas: monthly average solar elevation corrected for atmospheric refraction h, degree; average total cloud cover c, % (average total cloud cover); Global Horizontal Irradiation) GHI – G_0, W/m^2; Expected GHI corrected for the cloud cover), W/m^2 and the Measured Total Solar Radiation G, W/m^2. Formulae (1), (2) and (3) were used for this purpose.

The data were taken at local noon (12:00, GMT+2) when the incident GHI is maximal. Table 1 shows the monthly average values of the solar elevation h, degree; cloud cover c, %; GHI – G_0, W/m^2; the corrected GHI, W/m^2 and the total solar radiation measured G, W/m^2 for DOAS OPSIS, Burgas. Their annual values were also calculated.

The relationship between the total global insolation (GHI) G_0, GHI corrected for the cloud cover and the average cloud cover are illustrated in Fig.1.

The lowest values of the cloud cover (less than 36%) were registered for the period from May to September and, hence, the corrected GHI is lower than the expected total global insolation

(GHI) G_0. Correction of G_0 smaller than 20% was observed for July and august (July - 14 %, August – 17%). For the rest of the months the correction was higher than 50% (the smallest one in October – 50% and the highest one – in January – 73 %).

Table 1. Monthly average values for DOAS OPSIS, 12 local time (solar elevation *h*, degree; cloud cover, *c*, %; total global insolation (GHI) G_0, W/m^2; expected GHI, W/m^2 and measured total solar radiation *G*, W/m^2)

Month	Solar Elevation corrected for atm refraction *h* [deg]	Average total Cloud cover *c* [%]	Clear sky GHI G_0 [W/m^2]	Expected GHI corrected for Cloud cover [W/m^2]	Measured Total Solar Radiation *G* [W/m^2]
January	26.19	72.68	904.79	247.19	345.61
February	33.91	55.85	1002.07	442.86	450.46
March	44.97	54.95	1100.52	465.32	526.81
April	56.72	49.45	1143.53	532.77	596.69
May	65.76	36.02	1085.20	694.51	723.44
June	69.64	30.82	1049.50	761.39	726.91
July	67.43	24.13	1020.91	876.90	799.98
August	60.17	25.58	1068.14	882.41	827.81
September	49.83	34.98	1092.56	710.35	686.48
October	38.46	48.43	1062.24	526.51	527.84
November	28.89	46.42	896.64	480.45	436.37
December	24.17	56.52	862.02	374.85	356.12
Ann	47.18	44.65	1032.77	582.96	583.71

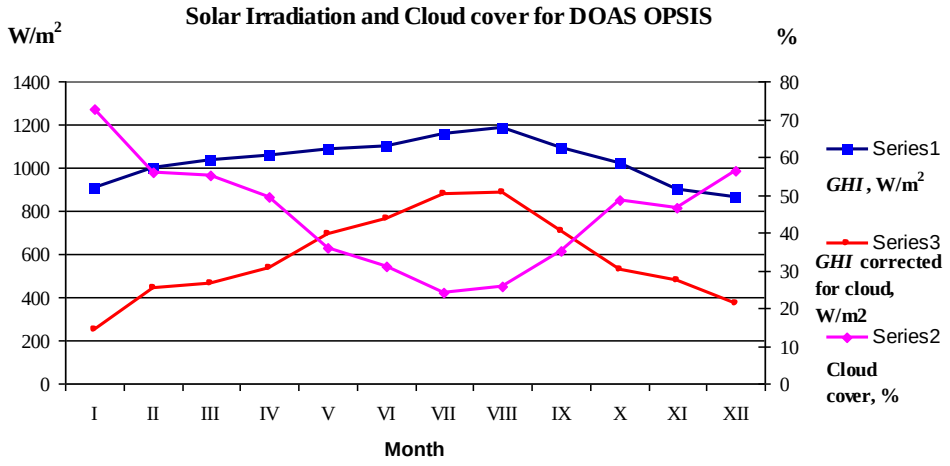

Fig. 1. Solar radiation and cloud cover for DOAS OPSIS, 12 GMT.

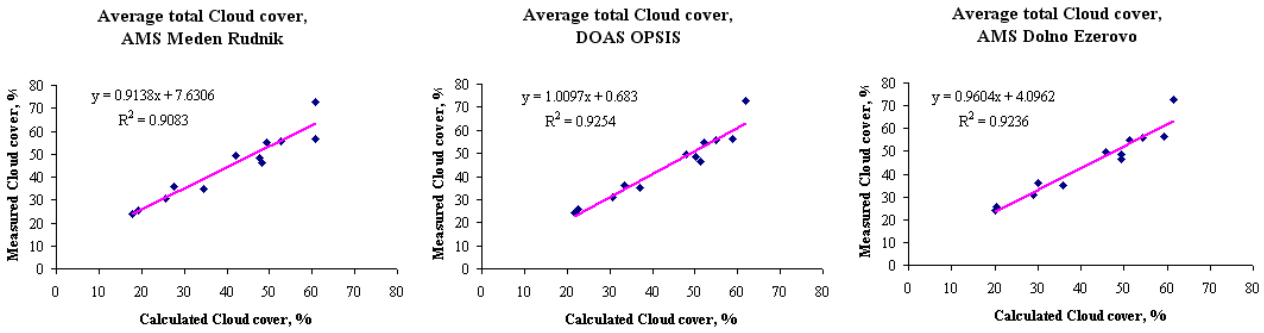

Fig. 2. Dependence between the measured and calculated cloud covers by sites

The dependencies between the cloud covers measured and calculated at three sites in the municipality of Bourgas: AMS Meden Rudnik, DOAS OPSIS and AMS Dolno Ezerovo are presented in Fig.2.

The regression coefficients and the coefficients of determination for the measured and the calculated cloud cover are presented in Table 2.

Table 2. Regression coefficients and Coefficients of determination for average total cloud cover

Monitoring site	Coefficients	Coefficient of determination R^2
AMS Meden Rudnik	b = 7.630592 a = 91.384575	0.908319
DOAS OPSIS	b = 0.683037 a = 100.96808	0.925380
AMS Dolno Ezerovo	b = 4.096164 a =96.03575	0.923558

It can be seen from Fig.2 and Table 2 that the coefficients of determination were high enough (R^2 > 0.9) which means that the regression dependence can be used for analysis and prediction.

Therefore, the cloud cover measured can be used to calculate the corrected GHI.

Fig.3 shows graphically the dependence between the values of the total solar radiation measured for DOAS OPSIS, 12:00 local time and the corrected GHI.

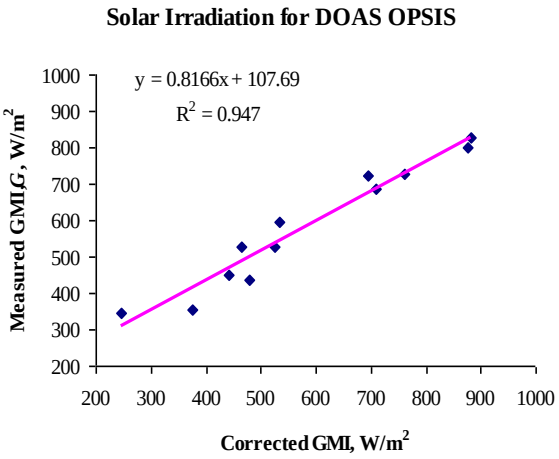

Fig. 3. Dependence between the measured and corrected radiation for DOAS OPSIS, 12:00 local time.

Table 3. Monthly average values of the total solar radiation for the monitoring sites measured daily from 8 to 17 (the approximate duration of sunshine)

Month	AMS Meden Rudnik G [W/m^2]	DOAS OPSIS G [W/m^2]	AMS Dolno Ezerovo G [W/m^2]
January	357.63	345.61	348.41
February	470.85	450.46	476.90
March	558.13	526.81	560.00
April	656.51	596.69	638.43
May	777.70	723.44	751.87
June	774.09	726.91	776.09
July	838.17	799.98	815.51
August	864.03	827.81	856.90
September	716.27	686.48	717.04
October	551.21	527.84	556.58
November	462.11	436.37	450.92
December	339.45	356.12	352.58
Ann	613.85	606.03	608.44

As can be seen from Fig.3, the coefficient of determination obtained was quite high (R^2 = 0.947), which indicated that the regression dependence can be used for analysis and prediction.

The analysis carried out showed that the total solar radiation calculated by formula (3) can be used for scientific research since the values of GHI corrected for the cloud cover are very close (which can also be observed in Fig.2).

The monthly average values of the total solar radiation at the monitoring sites measured daily from 8 to 17 (the approximate duration of sunshine) are shown in Table 3.

The annual incident radiation at a certain location has values more stable than the monthly

ones. It can be seen from the calculations carried out (Table 3) that the average total solar radiation measured for Burgas was 609.44 W/m^2 while the estimation of the solar potential is a total of 1334.47 kWh/m^2. The spent solar radiation energy is in the range of the values obtained for the estimation of the potential of the average annual solar radiation according to the data from the National Institute of Meteorology and Hydrology at the BAS for a 30 year period [9]. Their estimation is that the radiation over horizontal surface is 1315 kWh/m^2 and 1492 kWh/m^2 at optimal angle.

CONCLUSIONS

In the present paper, monthly average and annual estimations of the solar potential and cloud cover are made for three monitoring sites in the Municipality of Burgas.

It can be seen from the values obtained that the lowest values of cloud cover (less than 36%) were observed from May to September and, hence, the corrected GHI was smaller than the expected total global insolation (GHI). Corrections of G_0 smaller than 20% were obtained for July and August (July – 14 %, August – 17%). For the other months, the correction was more than 50% (the smallest for October– 50%, the highest for January – 73 %).

The dependence between the calculated and measured cloud cover for the three sites was studied. The coefficients of determination obtained were (R^2 >0.9) which indicates that the regression dependence is suitable for analysis and prediction.

The total solar radiation and the value corrected for the cloud cover were compared. The coefficient of determination was quite high (R^2 = 0.947). The calculated total solar radiation can be used in scientific research, e.g. for estimation of the solar potential.

It can be seen from the calculations carried out that the average total solar radiation measured for Burgas was 609.44 W/m^2 while the estimation of the solar potential is a total of 1334.47 kWh/m^2. The value obtained is in the range calculated by the National Institute of Meteorology and Hydrology at the BAS.

The monthly average and the annual estimations of the radiation can have practical use, e.g. in designing solar radiation collectors, heating and cooling installations, etc.

REFERENCES

1. Alexandrov, V., M. Schneider, E. Koleva, J. Moisselin. *Journal Theoretical and Applied Climatology*, **79**, (2003), pp. 133–149.
2. Alexandrov, V., P. Simeonov, V. Kazandzhiev, G. Korchev, Climate change. *NIMH - BAS, Sofia, Bulgaria*, (2010).
3. National Renewable Energy Laboratory (NREL), National Laboratory of the US Department of Energy, Office of Energy Efficiency and Renewable Energy, operated by the Alliance for Sustainable Energy, LLC, *Washington*, (2016), www.nrel.gov.
4. Taylor, B., A. Thompson (Editors). The International System of Units (SI). NIST Spe-cial Publication 330, National Institute of Standards and Technology, US Department of Commerce, *Washington, March* , (2008).
5. Sharif, A., A. Hussaini, I. Alenezi. New Method for Predicting the Performance of Solar Pond in any Sunny part of the World. *World Renewable Energy Congress, Linko-ping, Sweden*, May 8-13 (2011), p. 3702.
6. Iliev, I., V. Kamburova, A. Terziev, P. Gramatikov., *Scientific papers of the Rousse University*, **49** (1.2), (2010), pp. 8-13.
7. Duration of sunshine, (2016), http://www.gaisma.com/en/location/sofia.html.
8. Klein, S. *J. of Solar Energy*, **19** (1977), pp. 325-329.
9. The solar potential in Bulgaria, (2016), http://www.emde-solar.com.
10. Georgieva, A., K. Panayotova. *Annual Assen Zlatarov University, Burgas, Bulgaria*, **45** (1), 2016, pp. 61-65.
11. Georgieva, A. Ch. Karagiozov, J. Ulrich, B. Bogdanov, Y. Denev. *Asian Chemistry letters*, **14** (2), (2010), pp. 141-148.
12. Belovski, I. *Annual Assen Zlatarov University, Burgas, Bulgaria*, **45** (1), 2016, pp. 24-28.

ANNUAL OF ASSEN ZLATAROV UNIVERSITY, BURGAS
BULGARIA, 2017, v. XLVI (1)

ANALYSIS OF COMPUTER SIMULATION IN SOFTWARE ENVIRONMENT OF ONE-PHASE BRIDGE VOLTAGE INVERTER FOR A PHOTOVOLTAIC SYSTEM.

Vasil Ivanov
E-mail:vasil_bi@mail.bg

ABSTRACT

Software product MATLAB - SIMULINK computing, making graphs and charts is a modern method of creating mathematical models. Simulation structure of functional blocks of switching is built in Simulink programming environment.

Key words: *filter, amplitude frequency response, duty cycle, Matlab and Simulink.*

INTRODUCTION

The energy received from photovoltaic (PV) modules as primary sources cannot directly supply the loads from the power grid. For this reason a power electronic converter - inverter (Fig.1) is included in the architecture of a photovoltaic system. Its main function is to convert DC voltage from PV modules to AC with qualitative performance to ensure normal load operation.

DC/AC devices work with high efficiency because they use impulse control algorithm for power semiconductor switches. This method of operation is the most energy saving in switching devices. The efficiency of the inverter operation, with the active load and rated operating mode, reaches 98%.

A block diagram of an inverter incorporating input / output elements for modeling its mode of operation is shown in Fig. 1.

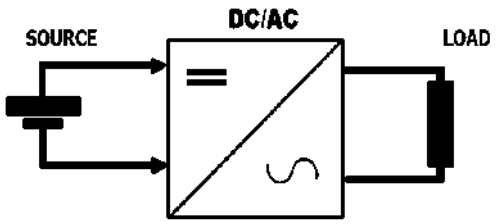

Fig. 1 Structure of an inverter system with source and load included

● Permanent source - simulates the energy produced by photovoltaic modules under standard test conditions (solar radiation and operating temperature) G=1000 W/m^2, T=25^{0}C, [Wp].

• Inverter (DC / AC) – bridge of two-wire circuit with powerful switch transistors.

● Electrical load - designed for network power supply (mains operation): U=23V, f=50Hz.

The voltage at the output of the inverters has a strictly defined shape, which depends on the control algorithm of the power devices in the circuit. The shape of the current through the load at the output, provided that voltage of strictly defined shape is applied to it, depends on the character and the parameters of the load circuit. Depending on the system voltage variables for supplying the load at the output, the most common are single-phase and three-phase voltage inverters [1].

The objective of the article is to demonstrate the efficiency of transformation through a single-phase voltage inverter in the simulation model analysis.

EXPERIMENT

Methodology

The main elements of the power part of the inverters are semiconductor devices controlled by a "circuit" method. These are usually bipolar transistors with isolated gate (IGBT) with built-in diode switched in reverse.

The impedance $\mathbf{Z_T}$ in the circuit loads is of L, R character and simulates the output transformer. It is between the two arms in "A" and "B". The scheme shown in Figure 2e is executed in a simulation environment Simulink[2].

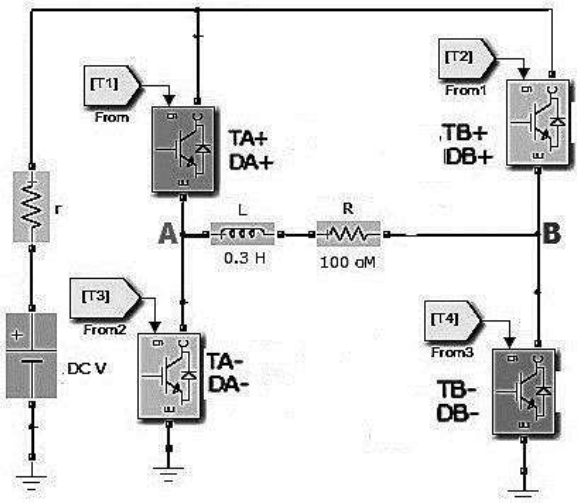

Fig. 2. Simulation model of single-phase voltage inverter.

Each pair of top and bottom transistors makes a unit of single-arm transistors marked as arm A and arm B. Transistors contain indexes for the arm that correspond to "-" and "+" or depending on whether they have a common point with the plus or minus of the power source.

The signals of the gates of the transistors on each arm are inversive with each other and their shape is rectangular (Fig. 3).

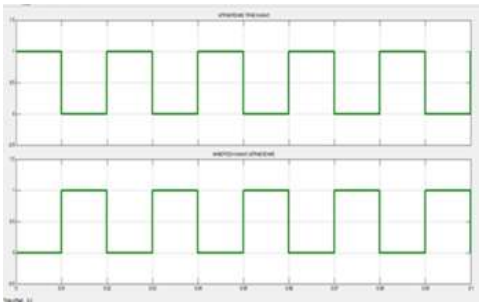

Fig. 3. Modeling the control signals dephased at $\pi = 180$ °

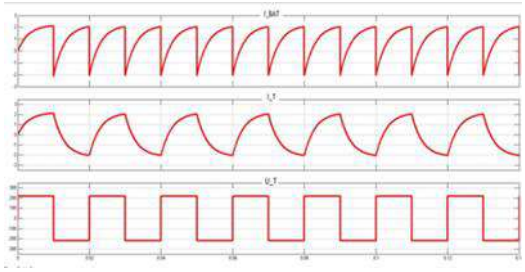

Fig. 4. Timing diagrams of starting the model of Fig.2.

The diagram shown in Fig. 4 is the result of starting the model of Fig. 2 and graphically shows the size and shape of the current from the battery IBAT, the output current IT and the output voltage UT applied to the load R, L.

The analysis of the diagrams in Figure 4 shows that the waveform of the output current depends on the complex nature of the load. A rectangular output voltage is set in the model with a 50% load factor and a 50 Hz frequency.

The law for the change of the load current i_T in one of the half-periods (e.g. the positive) of the output voltage UT is given with the expression:

$$i_T = \frac{U_d}{R_T}.\left[1 - \frac{2.e^{-\frac{\pi}{\omega.\tau}}}{1+e^{-\frac{\pi}{\omega.\tau}}}\right] \quad (1)$$

where,

$\tau = \frac{L_T}{R_T}$ – the time constant electrically load,

U_d – **DC** voltage from the PV modules,

R_T – active power on Z_T

Considering that for $\vartheta = \pi$, π, the adjustment angle and $i_T = I_M$, from (1) the maximum value of the current through the power devices can be found:

$$I_M = \frac{U_d}{R_T}.\frac{1-e^{-\frac{\pi}{\omega.\tau}}}{1+e^{-\frac{\pi}{\omega.\tau}}} \quad (2)$$

Ignoring commutation excess tension when switching power devices on his single shoulder (transistor or diode) applies to the whole supply voltage ("key" mode). The graph in Fig.4 can be found on the effective value of the output voltage:

$$U_T = \sqrt{\frac{1}{\pi}.\int_0^{\pi} U_d^2.d\vartheta} = U_d \quad (3)$$

The maximum value of the base frequency of the output voltage is:

$$U_{TM}^1 = \frac{2}{\pi}.\int_0^{\pi} U_d.\sin\vartheta\, d\vartheta = \frac{4}{\pi}.U_d \quad (4)$$

Consequently, the effective value is:

$$U_T^1 = \frac{U_{TM}^1}{\sqrt{2}} = \frac{2.\sqrt{2}}{\pi}.U_d \quad (5)$$

RESULTS AND DISCUSSION

● Simulation of the harmonics from the operation of the inverter system for the direct current $\mathbf{I_{DC}}$, , the output current $\mathbf{I_T}$ and the $\mathbf{U_T}$ voltage consumed by the load.

Figure 5 shows the amplitude frequency response AFR for the magnitudes of the harmonics

with sequence numbers from the direct current circuit I_{DC}.

Fig. 5 shows the amplitude frequency response **AFR** of the size of harmonics with numbers from **DC** circuit $\mathbf{I_{DC}}$.

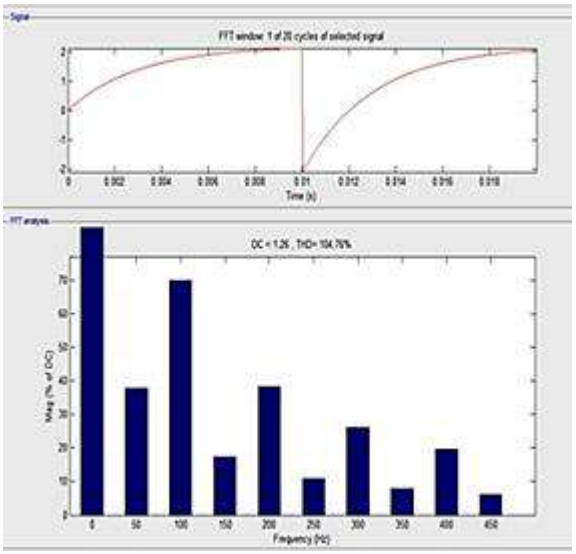

Fig. 5. AFR and magnitudes of the harmonics contained in the DC current when simulating the inverter's operation.

From the simulation of the diagram in Fig. 5, it is taken into account: I_{DC} = ***1,26 A*** ***at*** U_{dc} = ***220V***

The calculated maximum magnitude of the active power applied by the source is determined by the formula:

$$P_{in} = U_{DC}.I_{DC} = 220.1,26 = 277,2\,W \quad (6)$$

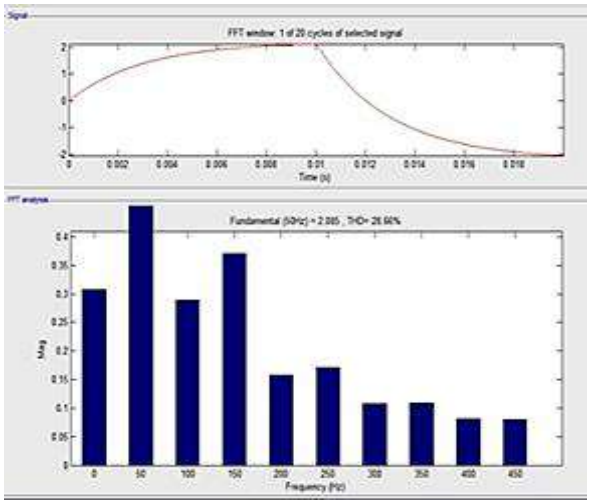

Fig. 6. The **AFR** and measured harmonic sizes from the inverter simulation in the alternating output current $\mathbf{I_T}$.

The effect of the output current on the load is shown in Fig. 6, the reported effective value is $\mathbf{I_T = 1,474A}$.

Simulation of the output voltage diagram is illustrated in Fig.7. The shape of the wave is rectangular and it comprises the number of odd numbered members of the **AFR.**

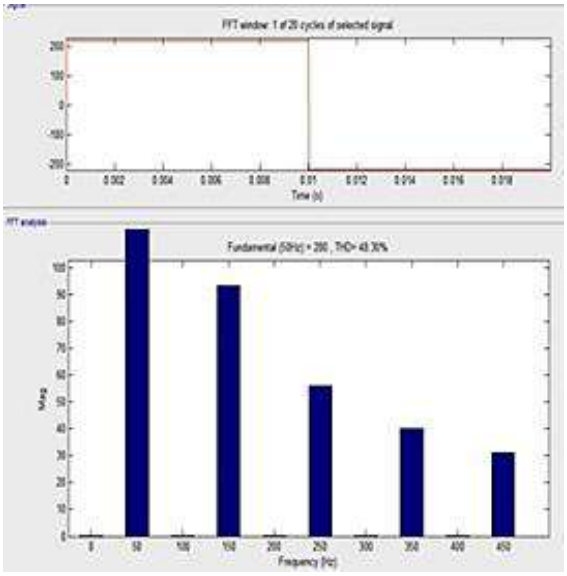

Fig. 7. Simulation **AFR** and measured magnitude of the inverter harmonics contained in the output voltage $\mathbf{U_T}$.

From the model diagram shown in Fig. 7, the magnitude of the main harmonic is measured from the output voltage with an effective value of **198V**, which can be compared with (5) at **Ud = 220V**

- Efficiency of the operation of the bridge voltage inverter.

Through the read results of modeling graphs, we can calculate the efficiency of the inverter system by the expression:

$$\eta = \frac{P_{1out}}{P_{in}} \quad (7)$$

where,

P_{1out} – active power output of the basic harmoni

P_{in} – active input power

The active output power is calculated by the magnitudes of the effective values of the first harmonic for the current and voltage read in Fig. 6 and Fig. 7: $U_1 = 198\,V, I_1 = 1,474\,A$. The angle of dephase applies for the output current and its magnitude is $\varphi_1 = -31^0$.

The active output power calculated for the main harmonic is:

$$P_{1out} = U_1.I_1.cos\varphi_1 \quad (8)$$

$$P_{1out} = 198.1, 474.0.86 = 250,1\,W$$

The constant current input power is calculated by (6) and after substituting numerical values in (7) for the efficiency the result is the following:

$$\eta = \frac{P_{out}}{P_{in}} = \frac{250,1}{277,2} = 0,902$$

CONCLUSIONS

The calculated efficiency shows the high efficiency of the inverters regardless of the rectangular shape of the output voltage.

The simulation analysis of a voltage inverter with a rectangular shape of the output signal proves its massive application in autonomous low power photovoltaic systems, automotive power converters, UPS, etc.

These devices can power electrical loads such as lighting fixtures, pumps, television and radio receivers, computer stations, objects remote from the public mains supply, and structures designed for continuous power supply.

No filter is applied to the test model, which takes into account the increased harmonics of the inverter system. When installing a reject filter in the output circuit, higher harmonics can be suppressed, which will improve the power, efficiency, and energy performance ratios applied to loads.

The economic efficiency of using single-phase inverters is low in good technical characteristics.

REFERENCES

1. Antchev, M., "The power electronic devices", Sofia, 2007.

2. Hudyakov, Galkin-German, Silovaya Elektronika, №1, №2, №3, №4”2005, №1”2006, №4’2007, №1’2008, №2’2008, №4’2008, №4”2009, №2’2010, №4”2011. - www.finestreet.ru.

ANNUAL OF ASSEN ZLATAROV UNIVERSITY, BURGAS
BULGARIA, 2017, v. XLVI (1)

STUDY OF THE QUALITY OF ELECTRIC POWER GENERATED BY A VOLTAGE INVERTER FOR PHOTOVOLTAIC SYSTEM

Vasil Ivanov, Neli Simeonova
E-mail: neli_simeonova@btu.bg

ABSTRACT

The aim of the study is to obtain experimental data on the performance of a small power photovoltaic system and analyze the quality of the energy generated and exchanged with the electric power system loads.

Key words: *inverter, photovoltaic, maximum power point, DC/AC converter.*

INTRODUCTION

Alternative power sources usually generate output voltage with direct current. In this case, only DC consuming devices can be powered but the loads in an electrical power grid are mostly alternating current ones. So it is necessary to transform the energy generated to reach properties compliant with the electric power system (EPS). The inverter is the device doing this for the photovoltaic (PV) systems connected to the power grid. It must provide nominal output voltage and frequency synchronized with the public power grid [1].

The purpose of the inverter in the photovoltaic systems is to transform the constant voltage generated by the solar generator into alternating one so the system could be attached to the grid. In more complex photovoltaic systems, besides transformation of the power, the inverter plays other roles. It has built-in MRRT algorithm for tracking the maximum power point, protection from overloading by voltage and current.

The linear structural scheme shown in Fig. 1 is for a photovoltaic system attached to the power grid by a main switchboard for low voltage (MSLV).

The scheme presented in Fig. 1 realizes exchange of electric power with the power transport grid through single phase bridge inverter DC/AC which transforms the constant voltage into alternating one.

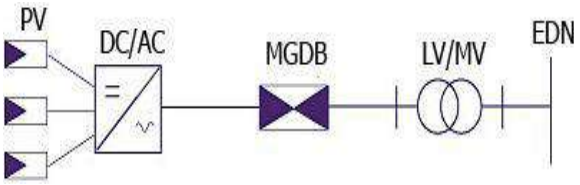

Fig. 1. Linear structural scheme: DC/AC–inverter, MSLV–main switchboard for low voltage, transformer LV/AvV–0,4– 10 kV, EPG – electric power grid.

EXPERIMENT

The energy exchange was recorded for certain period of time and it depends on the luminance of the photovoltaic modules and the complex nature of the loads in the power grid. The energy generated by the inverter was analyzed on the basis of graphical data obtained with network harmonic analyzer «QUALI Star».

The data obtained with the network analyzer «QUALI Star model C.A 8334B» were recorded at minimal mode of operation.

The images on device display carry graphical and digital information about the main electric power characteristics. These are U, I, P, waveform, THD, coefficients of power and efficiency, phase difference, peak factor, energy consumed, etc.

Fig. 2 shows the mounting and structural scheme of the voltage inverter [2].

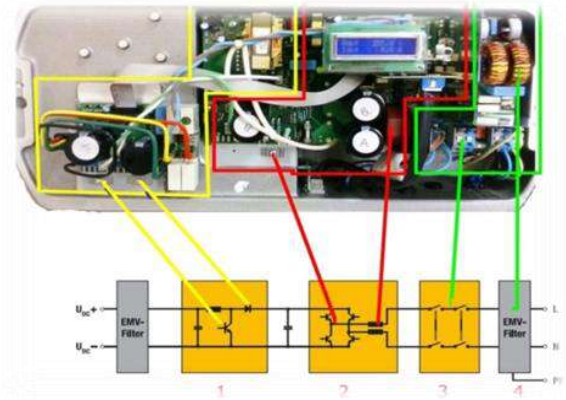

Fig. 2. SolarMax 2000C: 1 – increasing DC/DC converter, 2 – single phase bridge DC/AC inverter, 3 – power commutator, 4 – electronic filter.

The converter 1 increases and stabilizes the constant voltage produced by the photovoltaic modules. The built-in signal processor controls the output voltage by a feedback to the modules. It is programmed to maintain and stabilize the internal energy parameters at the point of maximal power by monitoring also the external parameters using feedbacks.

The single phase DC/AC inverter 2 is composed of four power elements in a bridge circuit in a single unit mounted on a radiator. The unit is designed by a scheme without output transformer for the connection to the grid. A built-in controller programmed with certain algorithm monitors the output parameters and, using voltage and current feedbacks, and regulates them with regard to the nominal values set. Under overloading by current and reduced input voltage, the inverter disconnects the system from the grid by activating the power commutator.

The electronic filter 4 is connected to the inverter output. It is built from inductive and capacitive elements aimed to smooth the shape of the output current wave. The filter restricts the high harmonic components present in the output voltage due to the impulse mode of operation of the powerful transistors.

Using the network analyzer „QUALI Star", all parameters and characteristics of the electric grid were measure at the point of connection according to scheme shown in Fig. 3.

The characteristics of the small power photovoltaic system (2 kWp) were determined under laboratory conditions (Fig. 3) the electrical parameters current, voltage and power were measured by network analyzer.

The data obtained were stored and analyzed to produce an estimation of the electric energy quality. The network analyzer measures the coefficient of high harmonics present in current and voltage waves which affect the quality of the output parameters. This was the reason to calculate the efficiency coefficients of the influencing harmonics in the current and voltage spectra. Their magnitude provides an estimation of the losss in the transformation of the DC to AC energy [3].

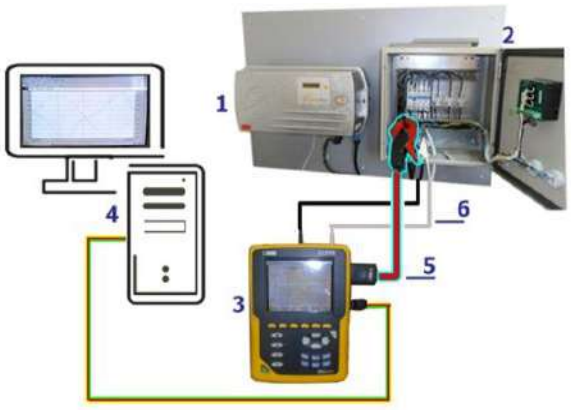

Fig. 3. Scheme of the experiment: 1 – single phase inverter „Solar Max 2000C", 2 – switchboard, 3 – network analyzer „QUALI Star" model C.A 8334B, 4 – computer workstation with the necessary software „Data Viewer", 5 – probe type ampere clamp, 6 – voltage probes

Method of calculation of the following parameters built-in in the network analyzer.

• Full power S received at inverter input:

$$S = \sqrt{P^2 + Q^2} \quad (1)$$

• The magnitudes of the output voltage U and current I were determined by taking into account their high harmonics:

$$I = \sqrt{\sum_{k=1}^{\infty} I_k^2}\,,\; U = \sqrt{\sum_{k=1}^{\infty} U_k^2} \quad (2)$$

• the active power for a complex load:

$$P = U_0.I_0 + \sum_{K=1}^{\infty} U_K.I_K.cos\varphi_K \quad (3)$$

• Efficiency coefficient

$$\eta = \frac{P_{out}}{P_{in}} \quad (4)$$

• Efficiency of the k[th] harmonic by sine wave of the voltage was calculated by the formula:

$$\eta_K = \frac{P_K}{P_1} = \frac{U_1.I_K.cos\,\varphi_K}{U_1.I_1.cos\,\varphi_1} \quad (5)$$

RESULTS AND DISCUSSION

The time diagram shown in Fig. 4 shows the shape of the output voltage at the connection point, as well as the magnitude of the main harmonic.

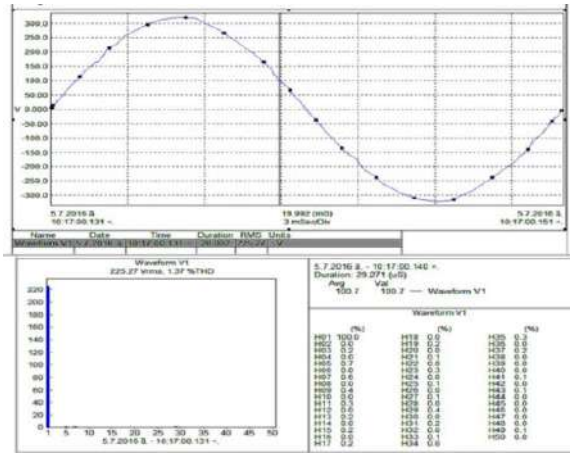

Fig. 4. Waveform and spectrum of the magnitudes of the effective values of each harmonic of the frequency of the output V_1

The degree of loading of the inverter by the photovoltaic system is represented by the diagram of the output current shown in Fig. 5.

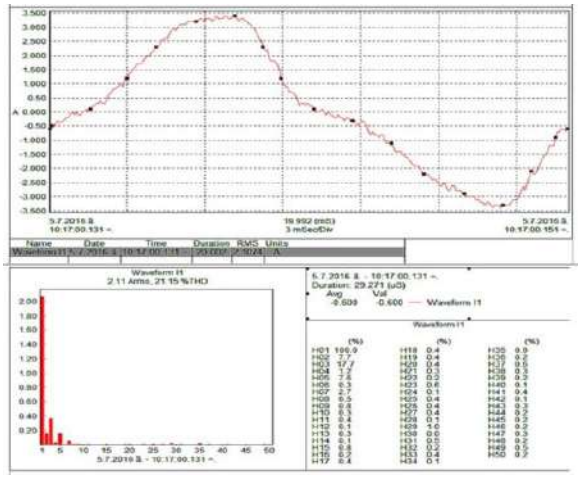

Fig. 5. Waveform and spectrum of the magnitudes of the effective values for each harmonic of the output current I_1

Waveform is a prerequisite for deterioration of output current quality. The result presented in the diagram shows non-sine waveform of the output current. The reason here is the non-linear part of a characteristic by which the inverter operates at small load.

The values of the current taken from the diagram in Fig. 5 for the first, third and fifth harmonic were:

I_1 = 2,107A (100%),
I_3 = 0,373A (17,7%) and
I_5 = 0,16A (7,6%).

The efficiency compared to the basic frequency (100%) $\boldsymbol{\eta_1 = 1}$ can be determined by the expression:

$$\boldsymbol{\eta_{out} = \eta_1 - \eta_3 - \eta_5} \quad (6)$$

After substitution in (5), for the higher harmonics №3, №5 we obtain:

$$\boldsymbol{\eta_3 = 0,177,\ \eta_5 = 0,076}$$

The final result is:

$$\boldsymbol{\eta_{out} = 1 - 0,177 - 0,076 = 0,747}.$$

Consequently, the coefficient of harmonics K_H increases, which leads to a decrease of the power factor and the efficiency coefficient K_E. The coefficient of efficiency is also low for this regime of operation $\boldsymbol{\eta_{out} = 0,747} < 0,95max$.

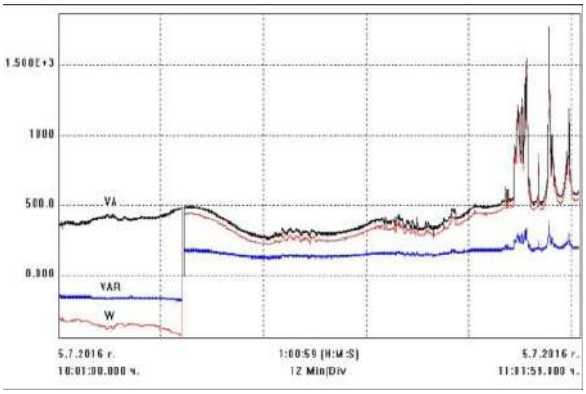

Fig. 6. Summary diagram of powers: W – active, VAR – reactive and VA – full for an interval of 1 h for the period from 10 to 11 o'clock

The negative part in Fig. 6 indicates that the direction of the active power consumed by the loads was from the powering grid [4].

The positive zone indicates that the direction of the power generated towards the loads was coming already from the photovoltaic system.

The peak values at the end of the experimental period were result of partial or full shadowing of the photovoltaic modules.

The diagram in Fig. 7 shows the change of the electric energy and exchange balance at the point of connection.

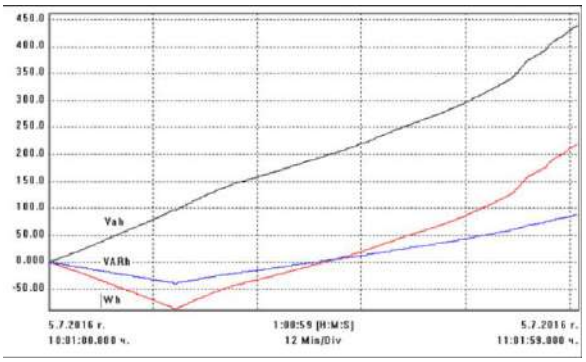

Fig. 7. Diagram of the energy exchange by operation of Photovoltaic systems

The increased number of harmonics present in the energy transportation affects the quality of the electric energy in the grid. Sensitive devices powered at the point of connection will have poor performance characteristics. The harmonic components of the current generate conductive phenomena which are spreading through the conductive medium and might cause heat effects on the cables.

As a result of the study, the following conclusions can be summarized:

- The output voltage contained less than 1% high harmonics. The effective value of the first harmonic was found to be U_1 = 225,27 V;
- The portions of the first, third and fifth harmonic of the current were as follows: I_1 = 73%, I_3 = 17,7% and I_5 = 7,6%;
- The coefficients of efficiency for the first three harmonics were: $\boldsymbol{\eta_1}$=**74**,%, $\boldsymbol{\eta_3}$=**17**,**7**% and $\boldsymbol{\eta_5}$=**7**,**6**%;
- Data were obtained on the energy exchange depending on the performance of the photovoltaic system;
- It was suggested to add adaptive filters to improve the waveforms of U and I by compensating for the complex nature of the loads under different regimes of operation.

REFERENCES

1. БДС EN 50160:2010. *Characteristics of the voltage of the electrical energy supplied by public electricity networks*.
2. V. Ivanov, "*Investigation of the Influence of Photovoltaic Systems on Electricity Networks"*, 2017, TU – Rousse .
3. БДС EN 61000-4-7:2002/A1:2009. Electromagnetic Compatibility (EMC). Part 4-7: *Testing and measurement methods. General Instrument Guidance and Measurement Instruments for Harmonics and Intermediate Harmonics in Power Systems and Related Equipment.*
4. Yakov V., V. Stefanov, *Electromechanical Devices and Systems*, University of Rousse, 2013, Avangard print EOOD.

ANNUAL OF ASSEN ZLATAROV UNIVERSITY, BURGAS
BULGARIA, 2017, v. XLVI (1)

SYNTHESIS AND TESTING OF A DIGITAL DIFFERENTIAL THERMOSTAT

Ivaylo Belovski
E-mail: ivbel@abv.bg

ABSTRACT

Differential thermostats are devices used mainly in solar energy water-heating installations and in central heating systems to which a water heater (boiler) is connected. They provide the unidirectional transmission of heat from the panel to the boiler, while at the same time monitoring the thermal regimes within the system and directing the operation of the pump. The current article aims to present the synthesis of an effective prototype of a digital thermostat with easy to operate interface, and to also analyze its main blocks and parameters.

Key words: *differential thermostat, solar thermostat, temperature difference*

INTRODUCTION

Due to the rising prices and depletion of petrol deposits used mainly for the production of fuels and energy resources, more and more attention is paid to renewable energy sources. Our Sun sends to Earth approximately 10^{18} kWh per year, which is about 3,000 times more than the energy that we humans currently need. Part of that energy is effectively used in water-heating installations [1-3]. With the growing interest in photovoltaic systems, their technological improvement has been paid little attention to in the last few years.

The principal structure of these installations is of the indirect pump type with an entatic water carrier and a heat-interchanger built into the very hot-water storage vessel itself. An essential component securing the effective and trouble-free operation of such installations is the differential thermostat [4-5] controlling the pump. Its job is to provide unidirectional transfer of heat from the panel to the boiler, while at the same time monitoring the thermal regimes within the system and managing the pump so that it operates in the most effective way possible. Another important function in the systems for continuous hot-water production is controlling an alternative way of heating in times of no sunshine (an electric heater or a burner running on natural gas or black oil).

Regardless of what elements are used in the building of a digital differential thermostat it needs to include the following key blocks:

- **Two thermal sensors**. The sensors give information about the ΔT difference in the temperature at the two points in the system being monitored. For example a solar hot water installation or a boiler connected to a central or local heating system;
- **Analogue-to-Digital Converter (ADC)** for processing the data from the sensors. The ADC can be in the form of a single Integrated Circuit (IC) multiplexing the inputs with analog keys, and digital output towards the central processing unit. Present-day microcontrollers have in their architecture built-in precision ADCs [6]. In most cases several outputs of the microcontroller are multiplexed to their input. This makes it possible to design very compact devices often superior to those with a stand-alone ADC;
- **Calculations and control** block. For small devices of low and medium complexity this is usually a single microcontroller having all the functional blocks, inputs and outputs necessary to perform a specific task;
- **Data input and output block**, normally containing indication and keyboard. Most often done as a single module on the front panel including both elements;
- **Output commutation block** (relay), controlling the pump of the solar water-heating installation or the valve at the input of the heat-exchanger of the hot water boiler connected to the heating installation;
- **Power supply** – a must-have for any electronic device. Its job is to provide stable electrical power in normal and borderline operating mode, plus good filtration of the outgoing voltages needed for the circuit to operate in a stable way.

The current article aims to propose a method for the synthesis of an effective prototype of a digital differential thermostat with a convenient to use interface, and to also present the analysis of its main blocks and parameters.

PRESENTATION

In designing the device the following block diagram was synthesized – see Figure 1 below.

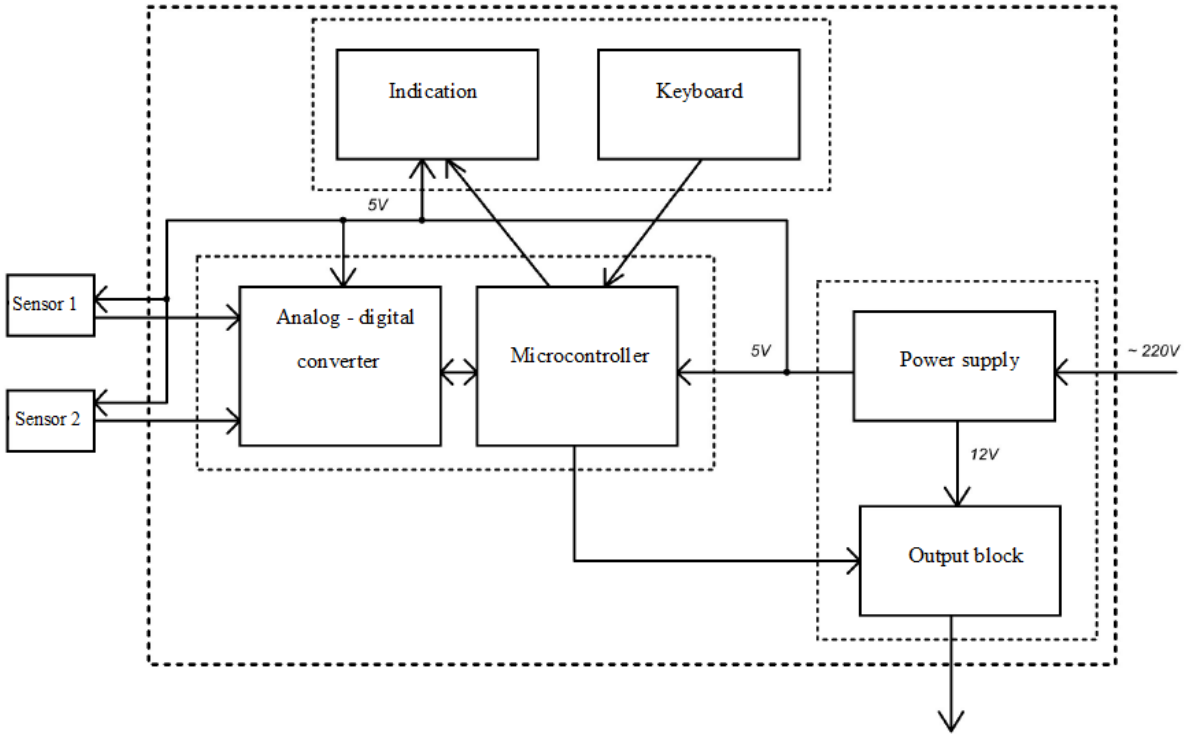

Fig. 1. Block diagram of a digital differential thermostat

The central block in this diagram is the microcontroller. The type selected is ATMEGA8, the smallest one from the MEGA series of the AVR line made by ATMEL Company [7]. Its key parameters related to the functionality of the device designed are as follows:

- 8 KBytes In-System Programmable Flash memory;
- 512 Bytes EEPROM memory;
- 1 KByte RAM memory;
- Built-in internal RC oscillator;
- Two 8-bit Timer/Counters;
- One 16-bit Timer/Counter;
- 6-channel ADC;
- Programmable Watchdog Timer with Separate On-chip Oscillator;
- 23 Programmable I/O (Input/Output) Lines.

The microcontroller has enough inputs / outputs available to control the peripheral blocks. They can reach a maximum number of 23 (when using the internal RC generator and using the RESET pin as an output). Six of them can be programmed as analogue inputs as well. Two are used as analogue inputs for the signals coming from the thermal sensors, and one is programmed as a digital input for the signals from the keyboard.

In order for the keyboard and indication to be jointly used, the keyboard is connected (by means of buttons) to the pins controlling the segments of the dynamic indication as shown in Figure 2. In this way, the number of microcontroller pins in use is reduced and the electrical diagram and the wiring tracks of the printed circuit board are simplified.

The indication of the thermostat is dynamic. Four seven-segment indicators with a common anode are used. For control 11 pins programmed to be outputs are used.

The anodes of each separate indicator are connected to the common +5V bus through BC807 type bipolar transistors that provide enough current for the normal operation of each of the 36 segments.

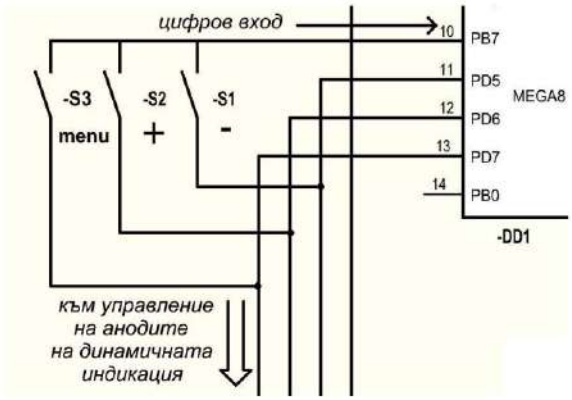

Fig. 2. Connection of the indication and keyboard to the microcontroller

The cathodes of the indicators are connected through resistors (R12-R18) directly to the microcontroller outputs. Two LED indicators are also provided – one to show pump-on mode, and another to show input signal or working parameters error.

The LM335 ICs are used as temperature sensors [8]. This is a three-terminal thermal sensor – temperature to voltage convertor. It was chosen because of its relatively simple structure, good results of data output in temperature measurement and little dependence on unstable power sources. Figure 3 shows the integrated circuit internal architecture.

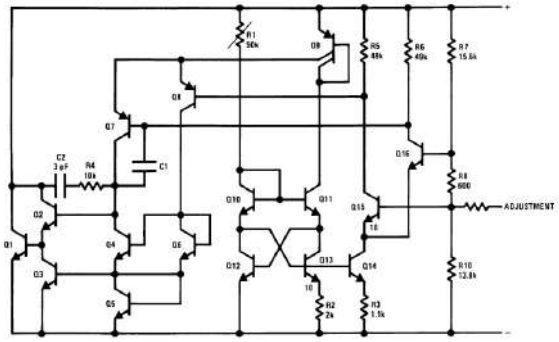

Fig. 3. Internal architecture of LM335 IC

The input circuits of the IC are voltage dividers – see Figure 4.

The role of the R2 - R3 divider is to fit the voltage of the LM335 thermal sensor to the range of the ADC of the microcontroller, whose reference voltage is set by the generator of reference voltage inside the microcontroller itself.

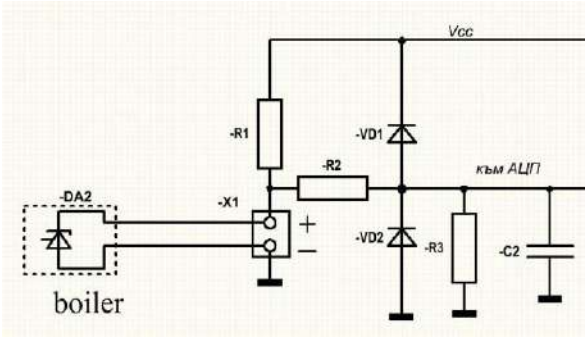

Fig. 4. Input circuit of the electrical diagram of a differential thermostat

There is a standard power block, consisting of a mains transformer and a bridge rectifier with a smoothing capacitor. The stabilized voltage U = 5V for the digital components is provided through a standard L7805 stabilizer.

The K1 output relay is controlled from a pin (PB1) of the microcontroller through a BC337 transistor (VT5). A diode (VD7) is added to the circuit of the coil to damper the reverse voltage appearing when the power fed to the relay coil stops. The relay is powered from the unstabilized voltage after the bridge rectifier (VB1) and its filtering capacitor – Figure 5.

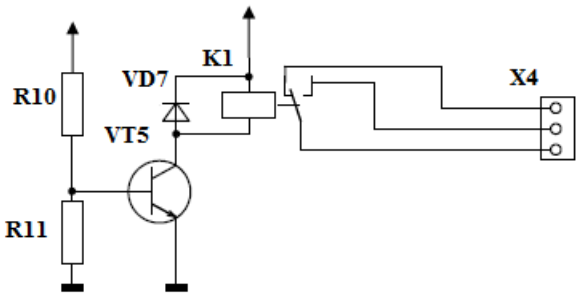

Fig. 5. Electrical diagram of the output block of the differential thermostat

After the digital differential thermostat was designed and made the accuracy of the thermal readings from the sensors was tested. Their readings were compared against those of a reference class (etalon) thermometer with 0,1 ^{o}C precision . The results from the test are presented in Table 1 below.

Table 1. Results from the testing of the thermal sensors

$T, {}^oC$	20	40	60	80	100
$T_{etalon}, {}^oC$	20	40	60	80	100
$T_{sensor1}, {}^oC$	20,6	40,5	60,4	80,3	100,2
$T_{sensor2}, {}^oC$	20,7	40,5	60,5	80,3	100,4

CONCLUSION

A digital differential thermostat has been designed and synthesized, and can be successfully applied in the household installations for heating water through solar energy and also in the central heating systems to which hot water boilers are connected.

The design was on the basis of an analysis of the main components of the differential thermostat. Using this analysis, the block diagram and principal electrical diagram containing the components needed for the thermostat were prepared. The selection of components was done taking into account the primary goal set: to create a compact, reliable and well-functioning device at a relatively affordable price.

The ATMEG A8 microcontroller was chosen for the control block – it fully meets all the requirements for managing the peripheral modules.

Many factors important for the functioning of the differential thermostat have been taken into account when writing the software. The source code includes the "watchdog" timer of the microcontroller – the watchdog improves reliability and restarts the system when external forces bring it to a non-functional state.

The communication interface of the differential thermostat is convenient for the user, and no unnecessary buttons or functions are included.

REFERENCES

1. Qu M., H. Yin, D.,*A solar thermal cooling and heating system for a building: experimental and model based performance analysis and design,* Solar Energy, Vol.84, Iss. 2, pp. 166-182, Elsevier, 2010.
2. Lunde P., *Solar thermal engineering: space heating and hot water systems*, NY, 1980.
3. Ozgener L., A. Hepbasli, I. Dincer**,** *Performance investigation of two geothermal district heating systems for building applications: energy analysis*, Energie and Buildings,Vol.38, Iss.4, pp. 286-292, Elsevier, 2006.
4. Cahlon B., D. Schmidt, M. Shillor, X. Zou, *Analysis of thermostat models*, Europeen Journal of Applied Mathetatics, Vol. 8, Iss.5, pp.437-455, 1997.
5. Liang C, X. Zhang, X. Li, X. Zhu, *Study on the performance of a solar assisted air source heat pump system for building heating,* Energie and Buildings,Vol.43, Iss.9, pp. 2188-2196, Elsevier, 2011.
6. Barrett S., D. Pack, *Microcontrollers Fundamentals for Engineers and Scientists,*Morgan and Claypool, 2006.
7. http://www.atmel.com/images/atmel-2486-8-bit avr mmicrocontrolleratmega8_l_ datasheet.pdf.
8. http://www.sensorzine.com/datasheet-of-lm 135-lm235-lm335-precision-temperature-sensors-379.html

ANNUAL OF ASSEN ZLATAROV UNIVERSITY, BURGAS
BULGARIA, 2017, v. XLVI (1)

AUTONOMOUS LIGHT DIAGNOSTICS SYSTEM FOR THE PURPOSES OF SEA BUOY MONITORING

Todor Kostadinov, Asen Iliev, Stanislav Simeonov
E-mail: kostadinov_todor@btu.bg

ABSTRACT

The present work addresses a novel approach in solution of the issues related to the monitoring process of the light navigation equipment in sea buoys. The main goal is to establish a seamless operation of the light system equipment used for navigation of marine vessels such as sea buoys and beacons. The monitoring is performed by a system using the signal output in the light equipment along with sensors used to sample the lamp parameters. An alarm event is then generated on light outage. The system output is plotted in user friendly graphical interface. The proper functionality of the monitoring system is proved by practical experiments and field tests.

Key words: *sea buoy, beacon, autonomous light monitoring system, diagnostics, measurement, smart lightning*

INTRODUCTION

Maritime navigation and water corridors designation are common to sailing for centuries. A good visibility of the water corridors is crucial in terms of wreck prevention and proper functionality of ports. The commonly used signs applied to dispatch the sea traffic are light emitting sources such as LED or incandescence bulb due to their long visibility range and distinctive signals. The light beacons use a variety of signals according to their purpose. They are presented as a pattern of light pulses with different duration obtained by a signal generator [1, 2]. Another application of light signalling is in the field of aviation where the presented system can also be used to monitor the airplane navigation lights located on the track. The aforementioned functionality is implemented in every light navigation sign [4]. To provide proper navigation the light source must meet certain requirements. For that purpose a monitoring system is required. A system designed to establish coarse estimation of the lantern functionality is presented in [3].

An alternative diagnostics of the full functionality and signalling of light including light intensity, signal duration and pattern along with fault detection has not been an object of investigation yet.

The present work proposes a monitoring system - part of the positioning and communication system suggested in [5, 6], similar to the one presented in [3]. The difference is that [3] is designed for a certain type of sea buoys and beacons manufactured by the company "Tideland" and the system [5, 6] can be implemented in every marine device, vessel or light source. In order to meet the requirement of all light navigation equipment [4], a complete analysis of the light system output must be performed. This is done in two stages: output of the controller providing the pulses and output of the light source. The signal sampling algorithm along with design of the system inputs is presented in chapter two, implementation and analysis is presented in chapter three. The results from the field test of the system are presented in chapter four.

LIGHT SAMPLING APPROACH

As mentioned in the previous chapter every light sign called beacon is comprised of three main blocks connected in serial: a power supply unit, a signal generator (controller) and a light emitting source (Fig. 1).

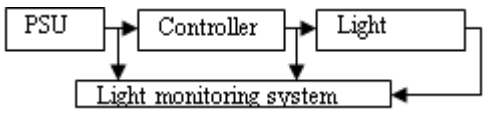

Fig. 1. Structure of a light sign and sampling points

In order for the light navigation to operate properly, each of the three blocks must work seamlessly – in other words, the input of a par-

ticular block depends on the output of the previous. This means that the system must monitor the output of each of the blocks accordingly, as shown in Fig. 1 and it must be capable of dealing with a wide variety of output readings in order to provide a broad area of use. The first and most important one is the measurement of the supply voltage as it is crucial to both the monitoring and monitored system as it is required to operate the systems. To do this the monitoring system [5] must work with a variety of DC voltage ranges varying from 3 to 48 volts. The microcontroller chosen in [5] has maximum measurement capabilities of the ADC of up to 4 volts, which is the supply voltage. In order to measure voltages higher than that, a voltage divider with a ratio 1/12 must be applied. The resistance of the voltage divider must be high so that less current is consumed out of the monitored device. The particular values are 3.6 and 1.2 mega ohms for the first and second resistor, accordingly. If a lack of supply voltage is established, an alarm event is generated as the system has an autonomous power supply that provides 72 hours operational time. To monitor the signal generated by the signal generator, it is necessary to state the level on which the controller is operating with the light source – high or low. In both cases this is recognized by the software as the duration of a pulse or a group of pulses is less than the pause duration (Fig. 2 a, b). To examine whether the controller provides a pulse (pulses) to the light source, a control signal must be sampled. This is done by the connection from the lantern controller to a digital input port of microcontroller of the measurement system. The pulse registration is performed by interception of an interrupt routine on the aforementioned digital port. A sample diagram of a signal generated from the controlled is depicted in Fig. 2.

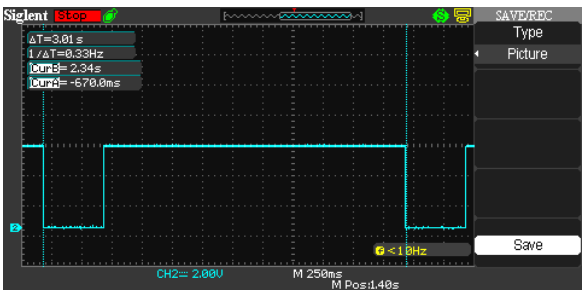

a)

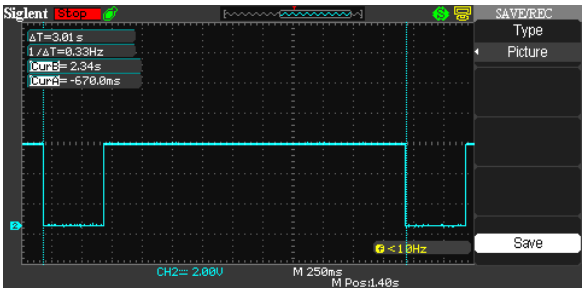

b)

Fig. 2. Diagram of the pulse generated by the controller

The pulse generated from the lamp controller depicted in Fig. 2 has a repetition period of 3 seconds (Fig. 2a) and pulse duration of 0.5 seconds (Fig. 2b), the value of the amplitude can vary from 3.6 volts up to 48 volts. To reduce the current flow, a 5 kilo ohm resistor is connected in serial. The parameters correspond to an entrance light sign. The colour of this sign can be green for the left side and red for the right side. Due to the variety of pulse amplitudes the digital port must be protected from overvoltage. A simple zener diode with breakdown voltage of 3.6 volts is sufficient, thus overvoltage will not cause malfunction of the connected port. A missing pulse is an indicator that the light is not operational meaning that alarm message must be generated. The pulse (pulses) duration is measured by time count from the rising to the falling edge. By counting the number of pulses it is possible to establish the type of the light sign and state its functionality.

In order to sample the lantern illumination, a photo sensor is required. The sensor is connected to a buffer in order to galvanic isolate it from the microcontroller. The buffer is then connected to an ADC port of choice. Thus the variation in light intensity will be transformed in voltage, which is then measured by the ADC. The final assessment of the lanterns is through sampling the parameters of the light source. It consists of two cases – first the presence of light emission during the pulse of the controller described above. Assuming the presence of power supply and no light is detected during the pulse provided by the controller means fault in the light source. In this case an alarm event is generated. The second case is measurement of light parameters during the presence of emission. If the parameters of the light including intensity and duration do not correspond to expected ones, a service of the light source is required. In that case a corre-

sponding alarm signal is generated. In case the intensity value meets the requirements but the pulse period is not in the corresponding time frame, an alarm event is generated.

If the beacon monitors the daytime light in order to switch on at night, there is a chance for a controller failure during the day. To avoid that failure, a daytime calculation is performed. If the lamp works during the day an alarm message is sent.

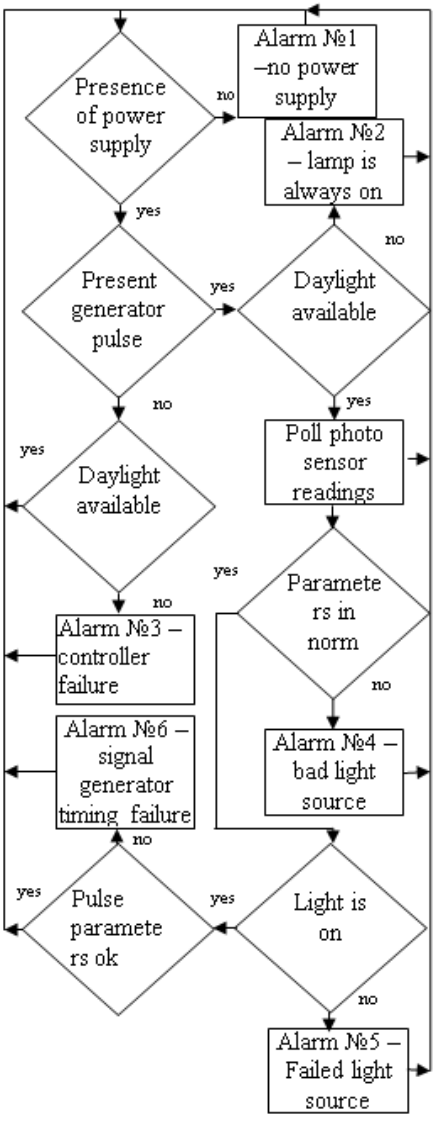

Fig. 3. Block diagram of the sampling algorithm

The sampling algorithm is presented in Fig. 3. The proposed sampling algorithm along with the hardware implementation presented in this chapter can provide seamless work of the system to a variety of lights.

MEASUREMENT SYSTEM IMPLEMENTATION AND ANALYSIS

A research object for the system is the light navigation sign manufactured by the company "Tideland" [3], presented in Fig. 4.

Fig. 4. Light navigation sign designed by "Tideland"

As can be seen from the figure above, the sign comprises a solid body with class IP67 water resistance containing photovoltaic panel placed on the outside, a controller, a battery and a communication system [6] placed inside. The light source along with the controller is placed in a transparent case on top of the body. Both parts are connected through a watertight nipple. Fig. 5 illustrates the connection of the system to the lamp.

In Fig. 5 the Power supply sample is taken directly from the lamp connectors via pink - 2 and gray - 1 cables (+ and -), thus providing an accurate measurement. The green cable - 3 is connected to a voltage divider implemented by the photo sensor -3 and a 2 kilo ohm resistor. The second terminal of the sensor is grounded.

Fig. 5. Connection to the measurement points

The pulse measured on the terminal - 5 is high when dark (lamp off – light sensor 4 senses light) and low when light (lamp on – 4 senses lack of light or low light). This can be seen from the measurements taken at the lamp signal terminal 5 (Fig. 6 a, b).

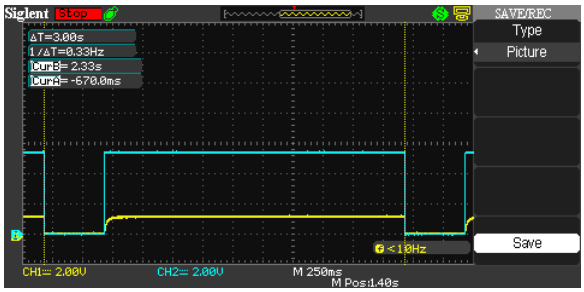

a)

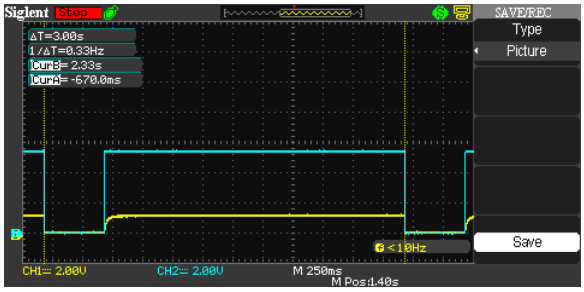

b)

Fig. 6. Parameters of lamp signals

As can be seen from the figure above, the pulse with higher amplitude denotes the one taken from the lamp controller – the other one is the pulse taken from the photo sensor. The amplitude difference is due to the voltage divider applied to the photo resistor. A significant moment in the process of sampling is the delay between the beginning of the controller pulse and the detected light pulse which is around 360 microseconds (Fig. 7). This delay is caused by the controller circuitry and if not taken into account, it could cause false readings.

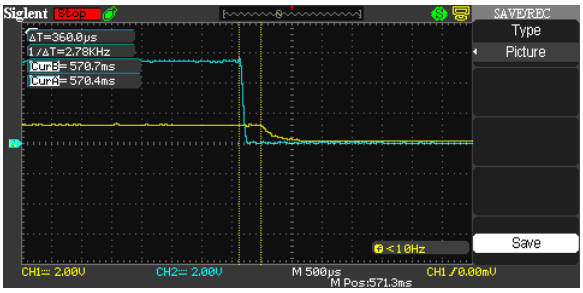

Fig. 7. Delay between electrical and light pulse.

There is also a difference between the falling edges of the pulses in Fig. 7. The controller pulse (the one with higher amplitude) transition between high and low level is roughly 100 microseconds and the falling front of the photo sensor pulse is five times larger. The photo sensor falling edge is also nonlinear due to the function of the current through the light diodes used to implement the light source. This fact has been also taken into account in the process of design of the diagnostics system.

The solution is to wait for the second pulse. The delay must not be greater than 0.5 seconds or an alarm message will be generated. This interval is taken due to the requirement for versatility.

The proposed monitoring algorithm in Fig. 3 matches the measurements taken from a randomly chosen commercial product. This verifies the algorithm performance.

RESULTS

The proposed algorithm has been implemented in [5] and installed in the device depicted in Fig. 4. The data sampled by the measurement system is sent via the communication module of [5]. It is then positioned on the map with the physical location of the device along with the data in human readable format. Due to limited margin for error simulation only three scenarios can be tested – alarm events 1, 2 and 5. Event 1 stands for lack of supply voltage – in this case the lamp will not operate as it is supplied by the main battery which is discharged, shortened or missing. This case is presented in Fig. 8.

Fig. 8. Diagnostic system output during alarm event 1

In case of alert the icon on the map is blinking and when clicked the failed parameter is coloured in red – in this case the battery level is 5.7 volts – row 6. In this case the lamp was supplied with a regulated power supply source with 5.7 volts as shown in the figure.

The second failure – a lamp always on is presented in Fig. 9, where the event is lamp always on – row 8. This means that either the controller failed in position – "on", the light switch is stuck in position "on" or the light is filling with water. In our case the photo sensor of the lamp was covered during daytime causing the lamp to operate.

Fig. 9. Diagnostic system output during alarm event 2

The last event – 5 is depicted in Fig. 10. The failure message in row 8 is lights always off. This means that the controller failed, the switch circuitry is broken, the lamp photo sensor is broken or the lights have defected. This was the case of dimmed photo sensor of the measurement system causing it to detect failed lights.

Fig. 10. Diagnostic system output during alarm event 1

Fig. 11. Diagnostic system output during normal operation

In case of normal operation routine no alarm events are present. The readings of the measurement system are depicted on Fig. 11 where the GPS coordinates are correct, battery charge is at normal level and the lights are functioning properly (switched off at daytime and on at night) The monitoring system is tested on variety of light sources such as sea buoys, beacons and light houses with diverse light signalling. The output provided by the system is available in real time at [7].

CONCLUSIONS

The routine, implementation and test of a light monitoring system for the purpose of sea signs monitoring has been presented in this work.

The design considerations taken aim to cover a large area of light signs of different manufacturers. The monitoring system appears to be useful also in other fields, such as traffic light and the urban lightning during the night. It is also applicable in other light signs with special purpose such as hazard light on road signs and tall building. The measurement system design also allows to be implemented at smart lightning and thus provide energy saving. The implementation and field test of the designed monitoring system routine has proven its functionality and the results show good overall system performance.

ACKNOWLEDGMENT

The authors are thankful for the support provided by the port of Burgas and Project 1/2017: Modernization of the navigation equipment in the area of the Sea administration of Burgas.

REFERENCES

1. US 6086220 A
2. US 20110121734 A1
3. http://www.tidelandsignal.com/File%20Library/Documents/Spec%20Sheets/GSM-Monitoring.pdf
4. http://www.iala-aism.org/
5. Kostadinov, T., "Design Of An Autonomous Communication, Measurement And Positioning Station", Industrial Technologies vol. IV, 22-23. June 2017, Burgas, Bulgaria.
6. Kostadinov, T., "Implementation of An Autonomous Communication, Measurement And Positioning Station", Industrial Technologies vol. IV, 22-23. June 2017, Burgas, Bulgaria.
7. https://www.shobs.bgports.bg

ANNUAL OF ASSEN ZLATAROV UNIVERSITY, BURGAS
BULGARIA, 2017, v. XLVI (1)

GENERALIZED NET OF THE PROCESS OF HIERARCHICAL CLUSTER ANALYSIS

Veselina Bureva, Stanislav Popov, Evdokia Sotirova, Boriana Miteva
E-mail: vbureva@btu.bg

ABSTRACT

In the paper, a generalized net model describing the process of hierarchical cluster analysis is constructed. It can be helpful in analyzing, managing and optimizing the clustering process. Hierarchical clustering can be applied using bottom-up (hierarchical agglomerative clustering) or top-down (hierarchical divisive clustering) approach. The clustering procedure uses parameters for calculating similarity or dissimilarity between the data objects and stopping criteria which can be a number of clusters or threshold for similarity/ dissimilarity measure.

Key words: *cluster analysis, generalized nets, hierarchical clustering*

INTRODUCTION

Hierarchical clustering is a type of cluster analysis which groups data objects into a tree of clusters. The type of hierarchical clustering is formed in a bottom-up (merging) or top-down (splitting) fashion. Therefore, hierarchical clustering can be agglomerative or divisive depending on the way of creating clusters. Hierarchical agglomerative clustering starts with each data object as a single cluster and step by step the two nearest data objects/clusters are iteratively merged. Divisive clustering starts with all the objects grouped in a single cluster. Clusters are being divided or split until each object is in a separate cluster. In the cluster analysis distance and similarity measures are used for determining the similarity between two points. The distance between data objects can be found using different distance measures – Euclidean distance, Manhattan distance (City-block distance), Chebychev distance, etc. The commonly used distance is the Euclidean distance which has the following form:

$$d_E(A,B)=\sqrt{(x_A-x_B)^2+(y_A-y_B)^2} \qquad (1)$$

When the cluster analysis will be with nominal or binary data the better choice is to use similarity measure (matching coefficient). In the hierarchical cluster analysis, after the calculation of distance/similarity measure, the linkage methods, variance methods or centroid methods are applied to form clusters. The linkage measures determine the way the data objects are grouped. Let $|x-y|$ is the distance between two data objects, x and y; c_i is the centroid of the cluster, C_i; and n_i are the number of objects in C_i. Widely used measures in the hierarchical clustering are the following [1, 9]:

- *Minimum distance between the data objects/clusters*: The points with minimum distance between them are merged into a cluster. This is sometimes called nearest-neighbor clustering algorithm. If the clustering process has a termination threshold, it is called single-linkage algorithm. The agglomerative hierarchical clustering algorithm that uses the minimum distance measure and the tree structure is popular with the name "minimal spanning tree algorithm".

$$d_{\min}(C_i,C_j)=\min_{x\in C_i,y\in C_j}|x-y| \qquad (2)$$

- *Maximum distance between the data objects/clusters*: The points are merged by maximum distance into a cluster. It is sometimes called farthest-neighbor clustering algorithm. If the clustering process has a termination threshold, it is called complete-linkage algorithm.

$$d_{\max}(C_i,C_j)=\max_{x\in C_i,y\in C_j}|x-y| \qquad (3)$$

- *Average distance between the data objects/clusters*: The dissimilarity between C_i and C_j is the average dissimilarity over all points in opposite groups, i.e. average distance across all pairs. The average linkage is a compromise between Single and Complete Linkage. The average distance is less sensitive to noise and outliers. Average linkage is popular with the names Mean linkage and UPGMA (Unweighted Pair Group Method with Arithmetic Mean).

$$d_{avg}(C_i,C_j)=\frac{1}{n_i n_j}\sum_{x\in C_i}\sum_{y\in C_j}|x-y| \qquad (4)$$

• *Centroid distance between data objects/clusters*: This method defines the distance between two clusters as the sum of the distances between cluster means for all of the variables. In the centroid method, the centroid of a merged cluster is a weighted combination of the centroids of the two individual clusters, where the weights are proportional to the size of the clusters. The algorithm is also known as Centroid linkage clustering or UPGMC (Unweighted Pair Group Method with Centroid Averaging) [1, 9].

$$d_{centroid}(C_i, C_j) = |c_i - c_j| \quad (5)$$

The measures presented above are included in the main algorithms for hierarchical cluster analysis. There are many variations of linkage methods, variance methods or centroid methods which can be applied in the clustering procedure.

GENERALIZED NET MODEL OF THE PROCESS OF HIERARCHICAL CLUSTER ANALYSIS

The concept of Generalized nets (GNs) is introduced in [3-5]. The constructed Generalized nets for data mining processes are presented in [2, 6-8, 10-12]. In the current research work, a GN of the process of hierarchical cluster analysis is constructed. It contains 6 transitions and 21 places (Figure 1). The Generalized net of the process of hierarchical cluster analysis contains the following set of transitions:

$$A = \{Z_1, Z_2, Z_3, Z_4, Z_5, Z_6\},$$

where the transitions describe these process:

- Z_1 – "Selecting data";
- Z_2 – "Determining the type of the hierarchical clustering";
- Z_3 – "Calculating the similarity (dissimilarity)/distance matrix";
- Z_4 – "Performing hierarchical agglomerative cluster analysis";
- Z_5 – "Performing hierarchical divisive cluster analysis";
- Z_6 – "Constructing the dendrogram (or Venn diagram)";

Initially, there is one α-token that is located in place L_3 with initial characteristic: "*data for cluster analysis*". In the next time-moments this token is split into two or more. The original α-token will continue to stay in place L_3, while the other α-tokens will move to transition Z_3 via place L_2.

Initially, there is one β-token that is located in place L_6 with initial characteristic: "*type of hierarchical clustering*". In the next time-moments this token is split into two. The original β-token will continue to stay in place L_6, while the other β-tokens will move to transition Z_3 via place L_5.

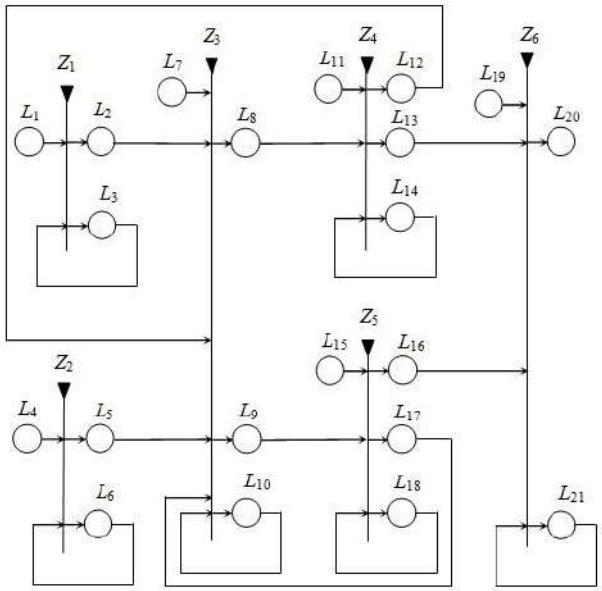

Fig. 1. GN model of the process of hierarchical cluster analysis

From place L_1 the α-token enters the net with initial characteristic respectively: "*new data for clustering*". The transition Z_1 has the form:

$$Z_1 = \langle\{L_1, L_3\}, \{L_2, L_3\}, R_1, \vee(L_1, L_3)\rangle,$$

where:

R_1 =	L_2	L_3
L_1	*false*	*true*
L_3	$W_{3,2}$	$W_{3,3}$

and:

$W_{3,2}$ ="The input data for cluster analysis is chosen",

$W_{3,3} = \neg W_{3,2}$.

The α-token entering in place L_3 (from L_1) doesn't obtain new characteristic. The α-token in place L_3 generates new α-token that enters in place L_2 with characteristic respectively: "*selected data for hierarchical cluster analysis*". This α-token will move to transition Z_3 where it will be merged with the β-tokens from places L_5 and L_7 in place L_{10}.

The β-token enters the net via place L_4 and has initial characteristic: "*type of hierarchical analysis*". The transition Z_2 has the form:

$$Z_2 = \langle\{L_4, L_6\}, \{L_5, L_6\}, R_2, \vee(L_4, L_6)\rangle,$$

where:

$$R_2 = \begin{array}{c|cc} & L_5 & L_6 \\ \hline L_4 & false & true \\ L_6 & W_{6,5} & W_{6,6} \end{array}$$

and:

$W_{6,5}$ ="The type of the hierarchical clustering procedure is chosen",

$W_{6,6} = \neg W_{6,5}$.

The β-token entering in place L_6 (from L_4) doesn't obtain new characteristic. The β-token in place L_6 generates new β-token that enters in place L_5 with characteristic respectively: "*selected type for hierarchical cluster analysis*". This β-token will move to transition Z_3 where it will be merged with the α- and β-tokens from places L_2 and place L_7 in place L_{10}.

The β-token enters the net via place L_7 and has initial characteristic: "*Similarity or distance metric*". The transition Z_3 has the form:

$$Z_3 = \langle\{L_7, L_2, L_{12}, L_5, L_{17}, L_{10}\}, \{L_8, L_9, L_{10}\}, R_3, \vee(\wedge(L_5, L_7), L_{12}, L_{17}, L_2, L_{10},)\rangle,$$

where:

$$R_3 = \begin{array}{c|ccc} & L_8 & L_9 & L_{10} \\ \hline L_7 & false & false & true \\ L_2 & false & false & true \\ L_{12} & false & false & true \\ L_5 & false & false & true \\ L_{17} & false & false & true \\ L_{10} & W_{10,8} & W_{10,9} & W_{10,10} \end{array}$$

and:

$W_{10,8}$ ="The similarity/distance matrix for hierarchical agglomerative clustering procedure is calculated",

$W_{10,9}$ ="The similarity (dissimilarity)/distance matrix for hierarchical divisive clustering procedure is calculated",

$W_{10,10} = \neg (W_{10,8} \wedge W_{10,9})$.

The α- and β-tokens entering in place L_{10} (from L_7, L_2, L_5, L_{12} and L_{17}) don't obtain new characteristics. At the first activation of the transition the token in place L_{10} (after merging the α- and β-tokens from places L_2, L_{12} or L_{17}) generates two new α-tokens that enter in places L_8 and L_9 with characteristics respectively: "*calculated similarity/distance matrix for hierarchical agglomerative clustering*" in place L_8 and "*calculated similarity (dissimilarity)/distance matrix for hierarchical divisive clustering*" in place L_9.

At the second activation of the transition the token from place L_{10} (after merging the α- and β-tokens from places L_2, L_5, L_7) generates new α-tokens that enter in places L_8 and L_9 with characteristic: "*calculated similarity/distance matrix for hierarchical agglomerative clustering after merging step*" in place L_8 and "*calculated similarity (dissimilarity)/distance matrix for hierarchical divisive clustering after dividing step*" in place L_9.

This transition will be activated several times until the cutting threshold is achieved.

The β-token enters the net via place L_{11} and has initial characteristic: "*criteria for merging the data objects and stopping criteria for hierarchical agglomerative clustering*". The transition Z_4 has the form:

$$Z_4 = \langle\{L_{11}, L_8, L_{14}\}, \{L_{12}, L_{13}, L_{14}\}, R_4, \vee(\wedge(L_{11}, L_8), L_{14})\rangle,$$

where:

$$R_4 = \begin{array}{c|ccc} & L_{12} & L_{13} & L_{14} \\ \hline L_{11} & false & false & true \\ L_8 & false & false & true \\ L_{14} & W_{14,12} & W_{14,13} & W_{14,14} \end{array}$$

and:

$W_{14,12}$ = "The similar objects are merged and the similarity/distance matrix need to be recalculated",

$W_{14,13}$ = "All objects are merged according to criteria for merging the data objects and stopping criteria for hierarchical agglomerative clustering",

$W_{14,14} = \neg (W_{14,12} \wedge W_{14,13})$.

The α- and β-tokens entering in place L_{14} (from L_{11} and L_8) don't obtain new characteristics. The token in place L_{14} generates two new α-tokens that enter in places L_{12} and L_{13} with characteristics respectively: "*merged objects and need of similarity/distance matrix recalculation*" in place L_{12} and "*merged objects according to criteria for merging the data objects and stopping criteria for hierarchical agglomerative clustering*" in place L_{13}.

Hierarchical agglomerative clustering presents each data object as a single cluster. Thereafter, the data points are merged according to criteria for merging until the stopping criteria is satisfied.

The β-token enters the net via place L_{15} and has initial characteristic: "*criteria for dividing the data objects and stopping criteria for hierarchical divisive clustering*". The transition Z_5 has the form:

$$Z_5 = \langle\{L_{15}, L_9, L_{18}\}, \{L_{16}, L_{17}, L_{18}\}, R_5, \vee(\wedge(L_{15}, L_9), L_{18})\rangle,$$

where:

$R_5 =$

	L_{16}	L_{17}	L_{18}
L_{15}	*false*	*false*	*true*
L_9	*false*	*false*	*true*
L_{18}	$W_{18,16}$	$W_{18,17}$	$W_{18,18}$

and:

$W_{18,16}$ = "All objects are divided according to criteria for dividing the data objects and stopping criteria for hierarchical divisive clustering",

$W_{18,17}$ = "The most dissimilar objects are divided and the dissimilarity/distance matrix needs to be recalculated",

$W_{18,18} = \neg (W_{18,16} \wedge W_{18,17})$.

The α- and β-tokens entering in place L_{18} (from L_{15} and L_9) don't obtain new characteristics. The token in place L_{18} generates two new α-tokens that enter in places L_{16} and L_{17} with characteristics respectively: "*divided objects according to criteria for dividing the data objects and stopping criteria for hierarchical divisive clustering*" in place L_{16} and "*divided objects and need of dissimilarity/distance matrix recalculation*" in place L_{17}.

Hierarchical divisive clustering presents all data objects as a single cluster. Therefore, the data points are divided according to criteria for dividing until the stopping criteria is satisfied.

The β-token enters the net via place L_{19} and has initial characteristic:"*visualization tool – dendogram or Venn diagram*". The transition Z_6 has the form:

$$Z_6 = \langle \{L_{19}, L_{13}, L_{16}, L_{21}\}, \{L_{20}, L_{21}\}, R_6, \vee (L_{19}, L_{13}, L_{16}, L_{21}) \rangle,$$

where:

	L_{20}	L_{21}
L_{19}	*false*	*true*
L_{13}	*false*	*true*
L_{16}	*false*	*true*
L_{21}	$W_{21,20}$	$W_{21,21}$

and:

$W_{21,20}$ = "Clusters are visualized",

$W_{21,21} = \neg W_{21,20}$.

A widely used method for presenting clusters is the dendogram. It is a tree diagram which visualizes the relationships between similar datasets.

The α- and β-tokens entering in place L_{21} (from L_{19}, L_{13} and L_{16}) don't obtain new characteristics. The token in place L_{21} generates new α-token that enters in place L_{20} with characteristic: "*visualized clusters*".

CONCLUSION

The constructed Generated net model can be used for description and simulation of the process of hierarchical cluster analysis. It can be helpful in analyzing, managing and optimizing the hierarchical clustering process. The current paper partly solves the problem describing the clustering procedures using GNs referred to in [2]. In future research, the constructed Generalized net of the process of hierarchical cluster analysis will be modified by extending the transition Z_1 in [7] using the hierarchical operator from the Generalized nets theory.

ACKNOWLEDGMENT

The authors are thankful for the support provided by the National Science Fund of Bulgaria under grant DN 02/10 New Instruments for Knowledge Discovery from Data and their Modelling and the project of Asen Zlatarov University under Ref. No. NIH-372/2016 "Methods and tools for extracting knowledge from heterogeneous sources of information"

REFERENCES

1. Aggarwal C., Data Mining: The Textbook, Springer, 2015
2. Atanassov K. *Generalized* Nets as a Tool for the Modelling of Data Mining Processes, IN: *Innovative Issues in Intelligent Systems, Vol. 623 of the series Studies in Computational Intelligence*, 2016, p.161-215
3. Atanassov K., E. Sotirova, Generalized Nets, Prof. Marin Drinov Academic Publishing House, 2017 (in bulgarian)
4. Atanassov, K. Generalized Nets, World Scientific, Singapore, 1991
5. Atanassov, K., On Generalized Nets Theory, Prof. M. Drinov Academic Publishing House, Sofia, 2007
6. Bureva V., E. Sotirova, K. Atanassov, Hierarchical generalized net model of the process of clustering, *Issues in Intuitionistic Fuzzy Sets and Generalized Nets,Vol.1*, Warsaw School of Information Technology, 2014, p.73-80.
7. Bureva V., E. Sotirova, K. Atanassov., Hierarchical generalized net model of the process of selecting a method for clustering, *15th Int.*

Workshop on Generalized Nets, Burgas, 16 October 2014, p. 39–48.

8. Bureva V., E. Sotirova, S. Popov, D. Mavrov, V. Traneva, Generalized Net of Cluster Analysis Process Using STING: A Statistical Information Grid Approach to Spatial Data Mining, IN: Henning Christiansen, Hélène Jaudoin, Panagiotis Chountas, Troels Andreasen, Henrik Legind Larsen (Eds.): *Flexible Query Answering Systems - 12th International Conference, FQAS 2017, London, UK, June 21-22, 2017. Proceedings. Lecture Notes in Computer Science 10333*, Springer, 2017, ISBN 978-3-319-59691-4
9. Han J., M. Kamber, J. Pei, Data Mining Concepts and Techniques. Third Edition, Elsevier, 2012
10. Krawczak M., S. Sotirov, E. Sotirova, Generalized net model for parallel optimization of multilayer neural network with time limit, *Proc. of 6th IEEE Int. Conf. on Intelligent Systems IS'12*, 2012, p.173-177. Print ISBN: 978-1-4673-2276-8
11. Roeva O., T. Pencheva, A. Shannon, K. Atanassov, Generalized Nets in Artificial Intrelligence. Volume 7: Generalized Nets and Genetic Algorithms, Prof. Marin Drinov Academic Publishing House, 2013, ISBN:978-954-322-700-6
12. Sotirova, E., D. Orozova, Generalized net model of the phases of the data mining process, *Developments in Fuzzy Sets, Intuitionistic Fuzzy Sets, Generalized Nets and Related Topics. Vol. II: Applications*, Poland, 2010, p. 247–260.

ANNUAL OF ASSEN ZLATAROV UNIVERSITY, BURGAS
BULGARIA, 2017, v. XLVI (1)

AUTOMATED METHOD FOR ESTIMATING A PEDESTRIAN AND CYCLIST TRAFFIC ACCIDENT IN THE ABSENCE OF BRAKE TRACES

Yuliyan Petrov
E-mail: yulipetrov@tu-sofia.bg

ABSTRACT

It was found out that pedestrian (cyclist) traffic accidents are a relatively high percentage of all traffic accidents in the country and the world as a whole. This article presents an automated method, which allows easier calculation of pedestrian (cyclist) traffic accidents. The proposed approach is implemented using GUI development environment in MATLAB.

Key words: *GUI Matlab, accident, cyclist traffic*

INTRODUCTION

Pedestrian (cyclist) traffic accidents (Fig. 1) are classified under various conditions [1]:

1. Depending on the impact type
   - frontal impact;
   - side impact.
2. According to the visibility and overview conditions;
   - unlimited visibility and overview;
   - limited visibility and overview;
   - reduced visibility;
   - reduced visibility and limited overview;
   - limited visibility and limited overview.

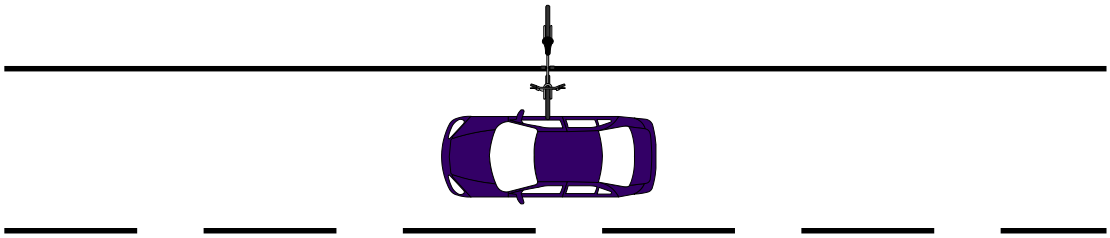

Fig. 1. Pedestrian (cyclist) traffic accident pattern

3. Depending on the vehicle motion type, the impact may be at:
   - uniform motion;
   - variable motion;
4. Depending on the pedestrian motion direction with respect to the vehicle and the roadway, the impact can be in the case of:
   - pedestrian sideways motion;
   - pedestrian perpendicular motion;
   - pedestrian and vehicle same way movement;
   - counter-movement of the pedestrian and the vehicle;
   - stationary pedestrian.

A sample pattern of pedestrian (cyclist) traffic accident is shown in the figure above.

METHOD DESCRIPTION AND IMPLEMENTATION

Given the nature of pedestrian traffic accidents [1, 2, 3, 4], the main ratios refer to the following dimensions (Fig. 2):

- V_n - pedestrian speed;
- t_y – break delay rise time;

- t_p – response time;
- t_{np} – break system delay time;
- $Vt_{np\ a}$ - vehicle speed;
- B_a - vehicle width;
- l_y – distance between the road and impact point.

The method flowchart is shown in the figure below:

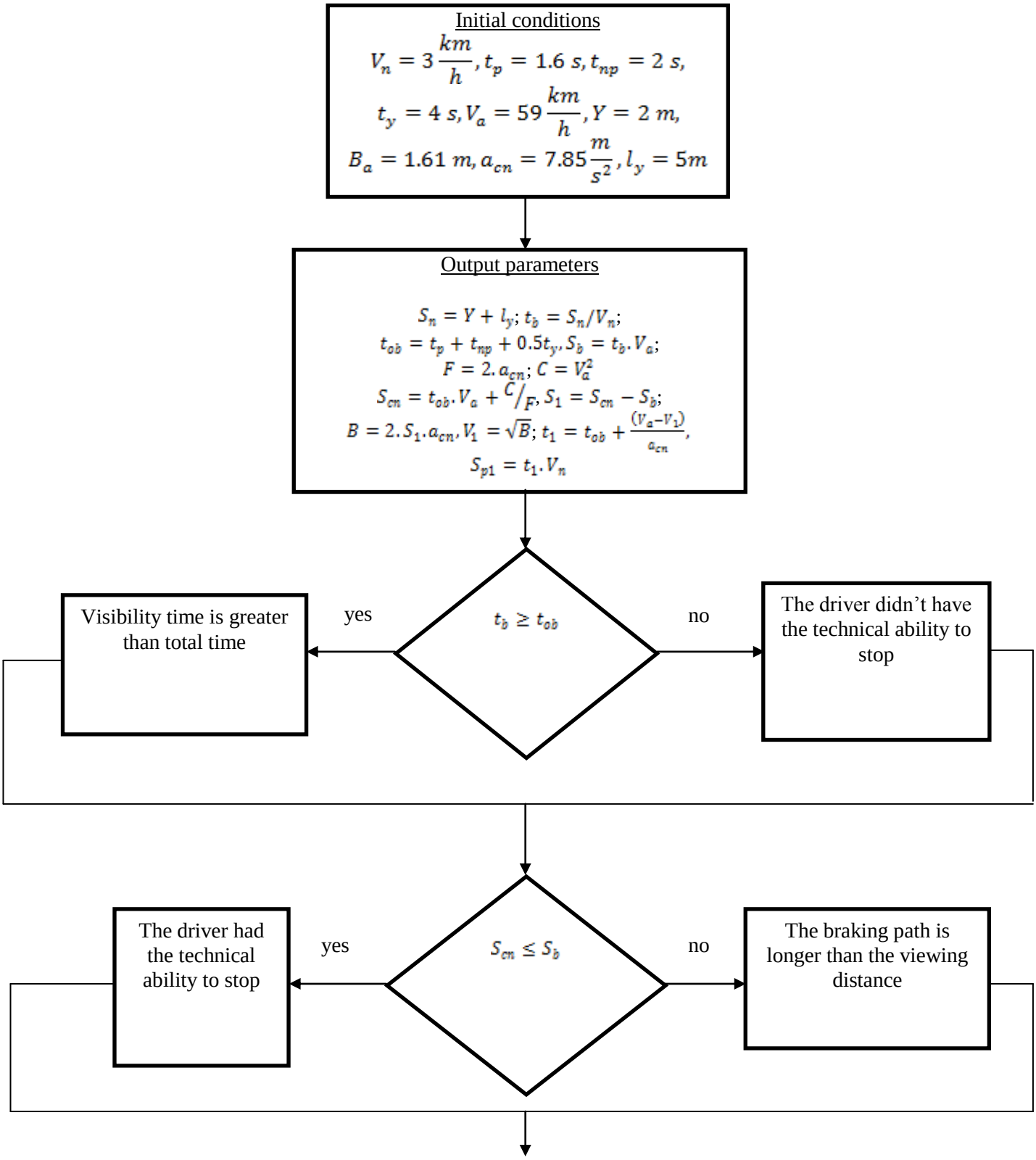

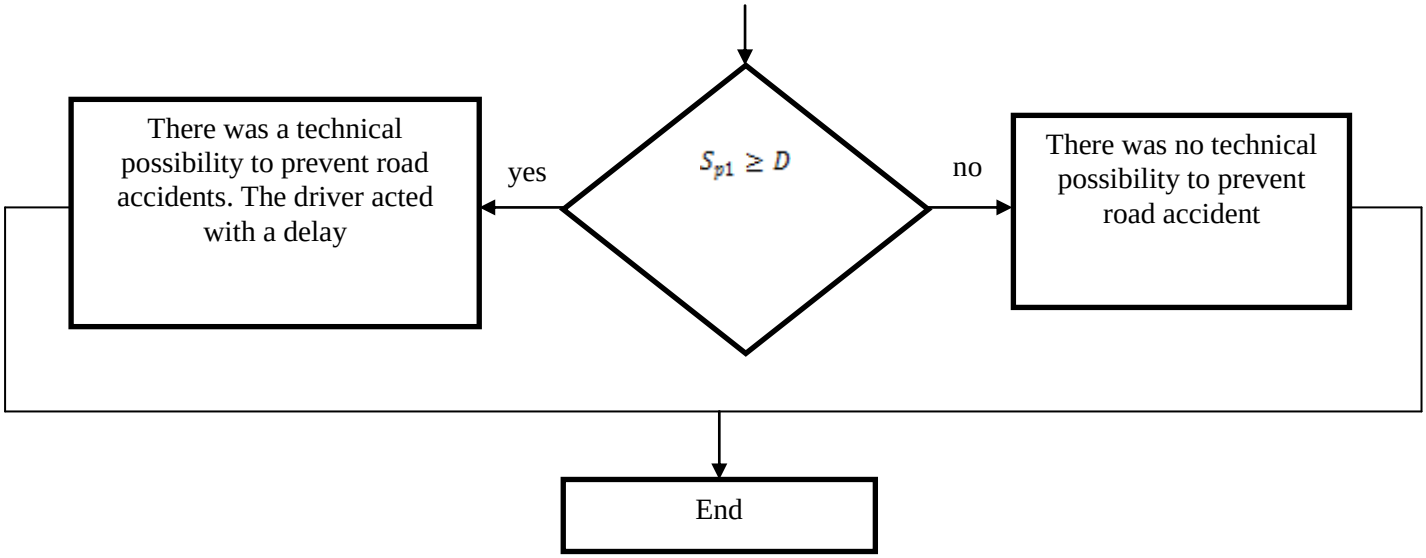

Fig. 2. Program flowchart

EXPERIMENTAL RESULTS

Fig. 3 shows a screenshot of the graphic user interface implementation of the method in MATLAB-Guide environment [5, 6, 7].

Based on the input parameters, the output values are calculated and the final estimation is made.

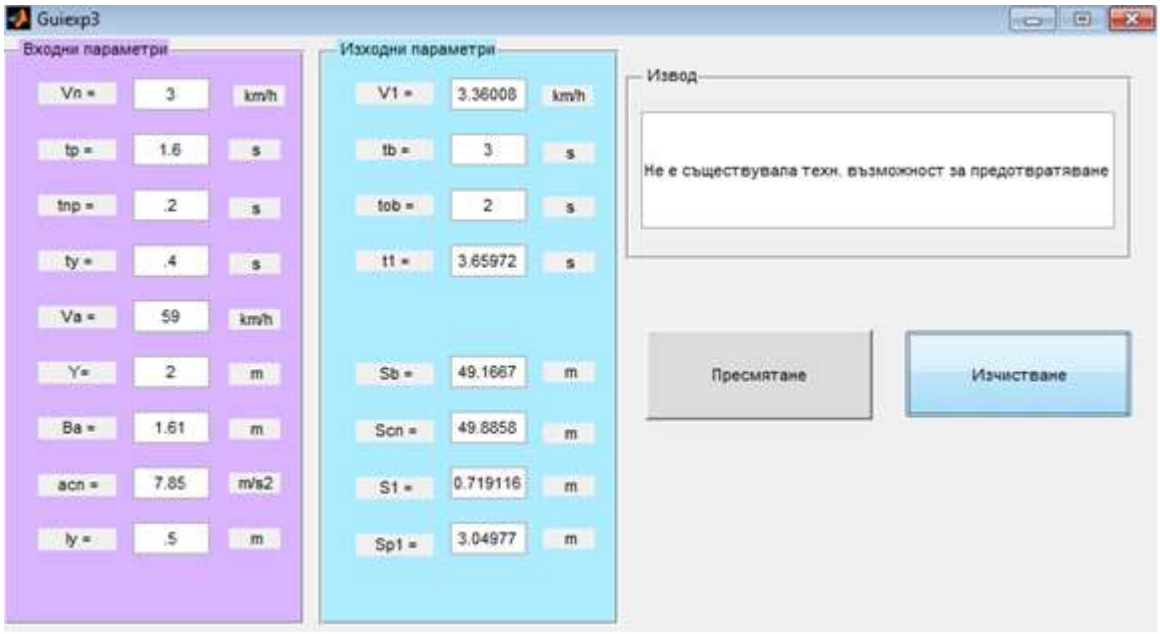

Fig. 3. Screenshot of the graphic user interface software implemented in MATLAB environment

The input parameters have the following sample values used in the example:

- pedestrian speed V_n = 0.83 m/s;
- break delay rise time t_y = 0.4 s;
- response time t_p = 1.6 s;
- break system delay time t_{np} = 0.2 s;
- break acceleration *acn* = 7.85 m/s^2;
- vehicle speed $Vt_{np\ a}$ = 59 m/s;
- vehicle width B_a = 1.61 m;
- distance between the road and impact point l_y = 0.5m.

The calculated output parameters have the following values:

tb =3.0120

tob =2

Visibility time is greater than the total time

Sb =49.3641

Scn =49.8858

The breaking path is longer than the visibility distance

S1 =0.5217

V1 =2.8618

t1 =3.7232

Sp1 =3.0902

Based on the calculated values, the final conclusion is: "There was no technical possibility to prevent the traffic accident".

CONCLUSION

The proposed automated approach allows:

- to explore dependencies and to determine the outcome of pedestrian (cyclist) traffic accident;
- based on an existing accident, to derive conclusions about possibilities to prevent pedestrian (cyclist) traffic accidents;
- to achieve more accurate results and reduce the error in the calculation part, by taking the result to the fourth decimal place.

The method can also be applied to a wider range of issues relating to the automation of road accident situations. With this kind of automated approach, the technical possibility or impossibility for preventing a traffic accident can be determined more accurately.

REFERENCES

1. Ilarionov, V. *Ekspertiza dorogno-transportnah proizshestvii*, 1989, Moscow
2. Baiet R, R. Louts, *Razsledvane na patno-transportni proizshestvia*, Tehnika, Sofia, 1985
3. Nikolaeva Z. *Computer Simulation of Solar Radiation and Ozone Concentration in the Atmosphere*, Journal of Balkan Ecology, ISSN 1311-0527, Vol. 18, Book 3, 2015, pp. 293-301.
4. Nikolaeva, Z. *Investigation and prediction of the total greenhouse gases emissions in Bulgaria*. Academic journal „Management and Education", 2012, Burgas, Volume 8, Part 4, ISSN 13126121, Prof. Assen Zlatarov University, p. 151-157.
5. Erbakanov L., L. Staneva, I. Vardeva, Y. Petrov, *Tire Contact Footprint Area Measurement Using an Alternative Bounding Box Method*, Int. Journal of Engineering Research and Application, Vol. 7, Issue 8, (Part -3) August 2017, pp.01-04
6. Ketkov, Y., A. Ketkov, M. Shultc, *Matlab 7. Programirovanie, chislenoe metoda*, Sankt – Peterburg, 2005
7. Badriev, I., V. Banderov, O. Zadvoronov, *Razrabotka graficheskogo polzvatelkogo interfeisa v srede Matlab*, Kazan, 2010

Assen Zlatarov University
ANNUAL, VOL. XLVI, BOOK 1, 2017
TECHNICAL AND NATURAL SCIENCES

Design and layout:
Libra Scorp Publisher
www.meridian27.com

Edition of:
Assen Zlatarov University
www.btu.bg

ISSN 1312-1359

BURGAS, 2017

ISSN 1312-1359